Analytical and Experimental Nanomechanical Approaches to Understanding the Ductile-to-Brittle Transition

A DISSERTATION
SUBMITTED TO THE FACULTY OF THE GRADUATE SCHOOL
OF THE UNIVERSITY OF MINNESOTA BY

Eric Daniel Hintsala

IN PARTIAL FULFILLMENT OF THE REQUIREMENTS
FOR THE DEGREE OF
DOCTOR OF PHILOSOPHY

Advisors
William W. Gerberich and K. Andre Mkhoyan

October 2015

Dedication:

This thesis is dedicated to my parents, Brian and Julie Hintsala, who raised me right.

Abstract

This dissertation presents progress towards understanding the ductile-to-brittle transition (DBT) using a mixture of nanomechanical experiments and an analytical model. The key concept is dislocation shielding of crack tips, which is occurs due to a dislocation back stress. In order to properly evaluate the role of these interactions, *in-situ* experiments are ideal by reducing the number of interacting dislocations and allowing direct observation of cracking behavior and the dislocations themselves.

First, *in-situ* transmission electron microscope (TEM) compression experiments of plasma-synthesized silicon nanocubes (NCs) are presented which shows plastic strains greater than 50% in a semi-brittle material. The mechanical properties are discussed and plasticity mechanisms are identified using post-mortem imaging with a combination of dark field and high-resolution imaging. This observations help to develop a back stress model which is used to fit the hardening regime. This represents the first study of its kind where back stresses are used in a discrete manner to match hardening rates. However, the important measurable quantities for evaluating the DBT include fracture toughness values and energetic activation parameters for cracking and plasticity. In order to do this, a new method for doing *in-situ* fracture experiments is explored. This method is pre-notched three point bending experiments, which were fabricated by focused ion beam (FIB) milling. Two different materials are evaluated: a model ductile material, Nitronic 50, an austenitic steel alloy, and a model brittle material, silicon. These experiments are performed *in-situ* scanning electron microscope (SEM) and TEM and explore different aspects including electron backscatter diffraction (EBSD) to track deformation in SEM scale experiments, pre-notching using a converged TEM beam to produce sharper notches better replicating natural cracks, etching procedures to reduce residual FIB damage and elevated temperature experiments. Lastly, an analytical method to predict DBTs is presented which can account for effects of strain rate, temperature and impurity presence. The model is tested by pre-existing data on macroscopic compact tension specimens of single crystal Fe-3%Si. Next, application of the model to nano/micro scale fracture toughness experiments is explored and the large number of confounding variables is discussed in detail. A first attempt at fitting is also presented.

Table of Contents

List of Tables

List of Figures

Chapter 1: Introduction

In the world of modern engineering, it may seem to the outside observer that mechanical design is well understood. Thanks to rigorous testing regimens and statistics, the mechanical performance of macroscopic components in a majority of cases is reliable. However, the understanding of many fundamental deformation processes occurring at atomistic scales remains beyond our grasp, which can culminate in seemingly unexplained failures at times. As micro-scale and nano-scale technologies emerge, these processes become increasingly important to understand. In addition, it's important to realize that even though mechanical properties are a fundamental piece of engineering, our modern understanding of plastic and brittle fracture mechanisms are actually very young. This is because the necessary tools to evaluate deformation processes at atomistic scales, such as electron microscopes, are less than 50 years old. The exciting news is that these characterization tools are rapidly improving, such that new levels of understanding are coming within our grasp.

The ultimate goal of studying the mechanical behavior of materials is to be able to precisely predict the resulting deformation from a generic applied stress state for any given material. Unfortunately, obtaining this knowledge requires understanding of the connection between structure, composition and properties which are complex and diverse. By performing deformation experiments on small volumes *in-situ* it is possible to study these local processes with unprecedented levels of characterization. These *in-situ* experiments can take place utilizing SEM or TEM and are a growing field of research [1-5]. These methods allow the researcher to introduce their own flaws that are similar in scale to the microstructural flaws that are preexisting in bulk, such as grain

boundaries, pre-notches, or inclusions [6-8]. The coupling of flaw control and improved characterization means that these types of experiments allows for studying fundamental deformation processes with unprecedented detail.   These types of experiments are crucial input for modeling efforts; the cycle of experimental validation and model/theory development is the essence of scientific advance.

Furthermore, studying mechanical behavior at the nanoscale has some direct technological impacts for a variety of nanoscale technologies already employed or being developed.   These include thin films for functional and protective coatings, microelectronics, MEMS/NEMS devices, developing drug delivery systems and more.

Deformation behavior can be divided into two broad types: brittle and ductile. Traditionally, metals are dominated by ductile processes while ceramics are dominated by brittle processes. However, in real materials, a mixture of both types of behavior are usually observed. There is an energetic competition between these processes, and the favorable mechanism can vary locally. By applying a load to a material, an energy is applied that must be dissipated. Crystalline materials can accommodate some amount of energy initially by elastically stretching the atomic bonds in its lattice, but when the elastic limit is reached, behavior can diverge significantly. Ductile processes dissipate energy by step-wise deformation processes that result in a permanent shape change, where brittle processes dissipate energy by the formation of new surfaces.   The differences in energy cost are based on bonding character and crystal structure. The energetics can be affected by several variables, such as temperature, strain rate, presence of impurities and as previously mentioned, size, such that a given material may behave in a brittle or ductile manner depending on the situation.   The fact that a material can

transition in its behavior gives opportunities for engineering. Brittle materials have a number of attractive qualities, such as lower conductivities, transparency, high hardness and band gaps that can be engineered for use in electronic devices. A major limitation to the use of these materials is their brittleness, so if their ductility could be enhanced, much more reliable and robust devices could be produced.

To put the question being explored in this work bluntly, will a material behave in a ductile or brittle manner? More specifically, how much deformation energy can materials absorb before failure and what are the interactions of the variables listed previously leading to this answer? To work towards understanding the answers to these questions, both *in-situ* nanomechanical experiments and analytical methods are employed that attack the problem from two directions. It is proposed that a critical concept is dislocation-crack tip interactions based on dislocation shielding. Understanding and development of this concept into a full model that works at the nanoscale and incorporates the effects of temperature, strain rate and impurities requires several things. First dislocation back stress models are needed to characterize the crack tip interactions. Second, a method of measuring fracture toughness at the nanoscale which allows characterization of deformation mechanisms to evaluate activation parameters as a function of impurity content, temperature and strain rate is needed. Lastly, a model which can incorporate these measurements into a predicted fracture toughness value puts everything together. This dissertation does not achieve these goals, but progress in each of these directions is made.

The chapter overviews are as follows:

Chapter 2: Background Information – A brief overview of the relevant mechanical properties topics as well as a description of the nanoindentation and electron microscopy equipment utilized for the experimental portions of the manuscript.

Chapter 3: *In-situ* Compression of Silicon Nanocubes – Plasma-synthesized nanocubes are compressed *in-situ* transmission electron microscope. The mechanical properties, deformation regimes and characterization of the plasticity mechanisms are determined. A dislocation pile-up model is employed to fit the hardening rate in the nanocubes which contributes to understanding of dislocation shielding for DBT models.

Chapter 4: *In-situ* fracture testing by pre-notched bending specimens – A new experimental method for measuring fracture toughness *in-situ* the SEM and TEM is explored. Studies are performed for a model ductile material, Nitronic 50, an austenitic stainless steel and a model brittle material, silicon. This chapter follows a progression in techniques, experimental and analytical, needed to develop accurate fracture testing methodologies which can be employed at the nano/micro scale while simultaneously providing good visibility of cracking processes.

Chapter 5: Analytical methods coupling plasticity and fracture – A model for the DBT based on the interaction between crack tips and shielding dislocations is developed. The model is validating using example case of hydrogen and strain rate effects for single crystal Fe-3%Si. Next, applications to nano/micro scale experiments are considered, with complicating variables explored using insights gained from the previous chapters.

Chapter 2: Background Information

Chapter Overview: A brief overview of the relevant mechanical properties topics as well as a description of the nanoindentation and electron microscopy equipment utilized for the experimental portions of the manuscript.

2.1: Mechanical Properties

2.1.1: Dislocations

To understand plasticity, the critical concept is the dislocation, which is a linear crystalline defect representing a fundamental unit of plastic deformation. The original concept for a dislocation dates back many years, long before any proof of their existence was presented. This proof later came in many forms, but most notably with the invention of the transmission electron microscope [9]. A dislocation has two important vector quantities associated with it, the Burger's vector and its line vector [10,11]. The line vector represents the boundary between deformed and undeformed regions of a crystal. The Burger's vector represents the resulting shift in the crystal lattice caused by the passage of the dislocation. The angle between the line vector and Burger's vector is used to define a dislocation's character; if they are parallel a screw dislocation is formed and if they are perpendicular, an edge dislocation results but most often real dislocations are of mixed character. Edge and screw dislocations, as the limiting cases, have different stress fields associated with them, and different mobilities and are illustrated in Figure 2.1.
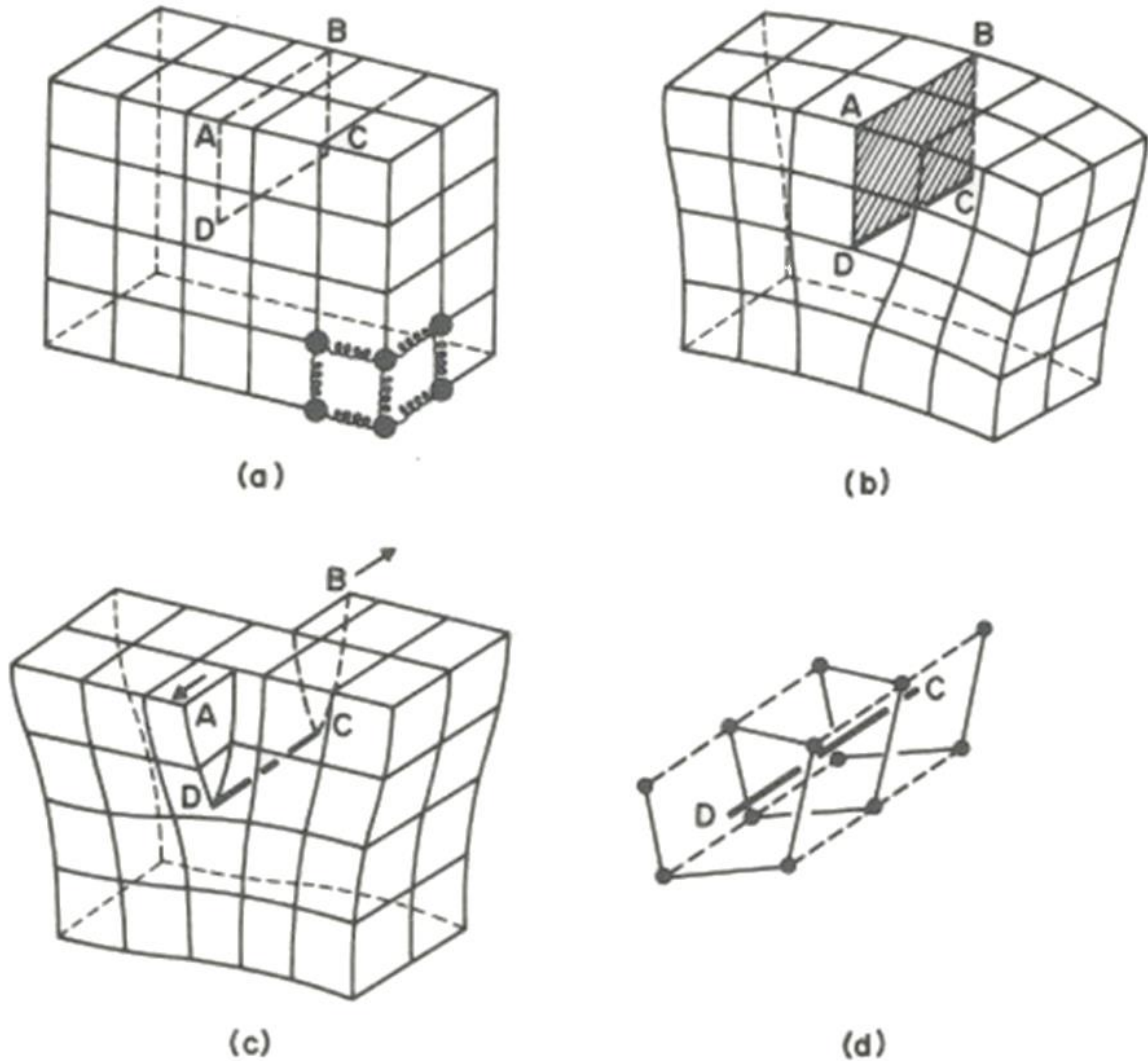
Figure 2.1: a) Perfect lattice with dashed lines showing insertion of extra half plane ABCD b) distortion of lattice due to introduction of the edge dislocation c) distortion of lattice due to introduction of a screw dislocation d) rotational symmetry of a screw dislocation and atomic displacements along the dashed axis. From Hull & Bacon [10].

The energy cost of forming a dislocation arises from the stress field of the dislocation itself and the energy cost to sever the necessary atomic bonds. Therefore, it makes sense that materials with stronger bonding, like ionic and covalent compared to metallic bonding, have a higher energy cost associated with dislocation nucleation. As can be seen in Figure 2.1, dislocations create strong local lattice distortions which give

rise to elastic stress fields which decay slowly as $1/r$. The nonzero stress fields components for a screw dislocation are given by Eqs. 1a,b [10]:

$$\sigma_{xz} = -\frac{\mu b}{2\pi}\frac{y}{x^2 + y^2},$$ (1a)

$$\sigma_{yz} = \frac{\mu b}{2\pi}\frac{x}{x^2 + y^2}$$ (1b)

and for an edge dislocation by Eqs. 2a-d:

$$\sigma_{xx} = -\frac{\mu b}{2\pi(1-\nu)}\frac{y(3x^2 + y^2)}{(x^2 + y^2)^2},$$ (2a)

$$\sigma_{yy} = \frac{\mu b}{2\pi(1-\nu)}\frac{y(x^2 - y^2)}{(x^2 + y^2)^2},$$ (2b)

$$\sigma_{xy} = \frac{\mu b}{2\pi(1-\nu)}\frac{x(x^2 - y^2)}{(x^2 + y^2)^2},$$ (2c)

$$\sigma_{zz} = \nu(\sigma_{xx} + \sigma_{yy}).$$ (2d)

For both, μ is the shear modulus, b is the Burgers vector and ν is Poisson's ratio. Because of these stress fields, dislocations interact with surfaces, interfaces other dislocations and defects. One important consequence is that they are attracted to free surfaces or interfaces with a lower modulus material where they can terminate and reduce their energy and be repelled from interfaces with materials that have a higher modulus. The second important consequence is that dislocations of the same type will repel one another while dislocations of opposite type attract to attempt to mutually annihilate. The repulsion of similar dislocations leads to formation of force equilibrium based dislocation arrays, the simplest of which is a single linear pile-up. These pile-ups exert strong shear stress fields both ahead and behind them as the normal stress components approximately cancel. This stress field takes the form of [10]:

7

$$\sigma_{BS} = \frac{\sigma_{FS}}{2} = \frac{\mu b N}{2\pi(1-\nu)l_s} \tag{3}$$

where N is the number of dislocations in the pile-up and l_s is the distance from the leading dislocation in the pile-up. A schematic of a dislocation pile-up is shown in Figure 2.2.
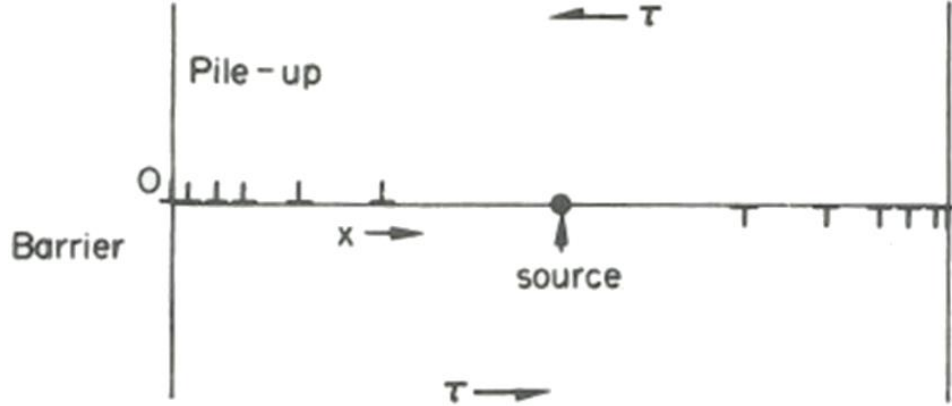
Figure 2.2: Schematic of a dislocation pile-up against a generic barrier due to dislocation nucleation and motion from a source operating under shear stress τ. From Hull & Bacon [10].

In order for a dislocation to propagate through a crystalline material, it needs to overcome the resistance of the lattice associated with bond breaking and atomic motion. This concept is named the Peierls barrier [12,13] which can be expressed as energy per unit length of dislocation line as:

$$U_0(x) = \frac{\sigma_p a b}{2\pi}\left[1 - \cos\left(\frac{2\pi x}{a}\right)\right] \tag{4}$$

where σ_p is the Peierls stress which is a characteristic lattice resistance, a is the lattice parameter, and b is the Burgers vector. It can be seen that this barrier is appropriately periodic with the lattice. The important result is that this barrier is in general lowest on the highest atomic density planes. Similarly to dislocation nucleation, materials with stronger bonding or more complicated crystal structures have higher Peierls barriers, making dislocation processes energetically less favorable. The combination of slip plane

8

and slip direction are known as a slip system which are usually multiply redundant depending on the symmetry of the crystal structure. The Peierls barrier determines the most favorable slip system in terms of energy cost, but the applied stress state leads to different resolved shear stresses for each slip system according to Schmid's law [14]. Both effects must be coupled to determine the precise activated slip system.

The last important point is that of dislocation self-energy. As previously described, dislocations create a lattice distortion with an associated energy cost per unit length. One outcome of this is that dislocations may split into two partial dislocations, separated by a distance d, whose Burgers vectors add to recreate the original Burgers vector. This results in a stacking fault between the two partial dislocations which has the same lattice as the rest of the material but slightly offset, with an associated energy cost, γ_{SFE}. The dislocation self-energy scales with b^2 such that the rule for predicting whether or not a dislocation will split into partials is [10]:

$$\gamma_{SFE} = \frac{\mu b^2}{2\pi d} \tag{5}$$

2.1.2: Fracture Mechanics

For crystalline materials, the main alternative to dislocation plasticity is brittle fracture where the bonds across a plane are severed rapidly, i.e. cracking. Linear elastic fracture mechanics (LEFM) is a well-developed field and some of the essential concepts will be briefly presented here [15]. One of the earliest accomplishments of fracture mechanics was the Griffith criterion [16,17], which for a perfectly brittle material (no dislocation nucleation/motion) predicts the necessary stress to cause catastrophic failure from a flaw of given size. The Griffith criterion is based on an energy balance approach.

The relief in stored elastic energy arising from an externally applied stress that is unsupported due to a crack and the energy cost of forming a new surface are given in:

$$a)\ U_E = -\frac{\pi a^2 \sigma^2}{E};\ \ b)\ U_S = 4a\gamma_S \tag{6}$$

where a is again the crack length, σ the applied stress, E the elastic modulus and γ_S is the free surface energy. These two terms may be summed together to give the total energy of the crack. Next, this is differentiated with respect to crack length and set equal to zero, to establish the minimum needed stress to extend the crack length. This, upon simplification, yields the final result shown in, which can be rearranged as in 7b to define a useful quantity, K_{IC}:

$$a)\ \sigma = \left(\frac{2E\gamma_S}{\pi a}\right)^{1/2};\ \ b)\ \sigma_C\sqrt{\pi a} = (2E\gamma_S)^{1/2} \equiv K_{IC} \tag{7}$$

Essentially, the Griffith criterion states that the elastic energy that is relieved by extending the crack by an increment *da,* also known as *G*, the strain energy release rate where $G = K^2/E$, must equal the energy cost of forming new free surfaces over the same interval *da*. K_{IC} is defined as the critical mode I stress intensity factor, and is a material property which describes a materials ability to resist crack growth. Because of this, it is often referred to as the fracture toughness. There is a G_{IC} which corresponds to K_{IC} where a crack will propagate unstably towards fracture. In the case of a brittle material, G_{IC} is simply equal to $2\gamma_S$, but as will be seen in the next section, G can incorporate other strain energy dissipation mechanisms. Another consequence of the Griffith criterion is that in brittle materials, fracture occurs along well defined atomic planes with the lowest surface energy, known as cleavage planes. Redundant cleavage planes exist within a

given lattice, so the one with the highest resolved stress on it will fracture first. This is

reminiscent of Schmid's law for plasticity.
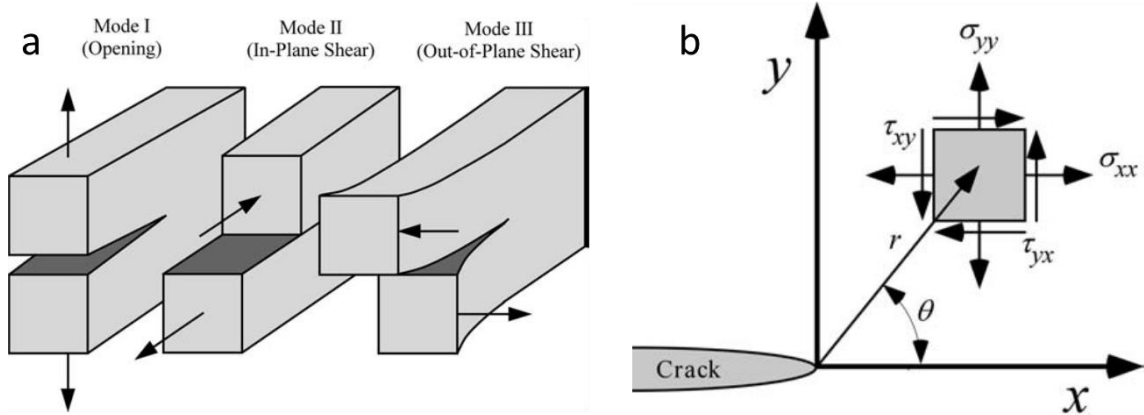
Figure 2.3: a) Schematic of crack loading modes b) Components of a crack tip stress field using r, θ coordinates. From T.L. Anderson [18].

There are three basic modes by which a crack or flaw can be extended, as

illustrated in Fig. 2.3a. Mode I is a tensile opening mode, Mode II is an in-plane shearing

mode, and Mode III is a transverse shear or tearing mode. Of the three, Mode I is the

most destructive and is often the only one considered. For embedded flaws, high tensile

stresses are typically present due to a hydrostatic, or triaxial, stress state. This is

illustrated both in Fig 2.3b and described in Equation 8a-c for a perfectly sharp crack

[18]:

$$\sigma_x = \frac{K}{\sqrt{2\pi r}}\left[cos\frac{\theta}{2}\left(1 - sin\frac{\theta}{2}sin\frac{3\theta}{2}\right)\right] \tag{8a}$$

$$\sigma_y = \frac{K}{\sqrt{2\pi r}}\left[cos\frac{\theta}{2}\left(1 + sin\frac{\theta}{2}sin\frac{3\theta}{2}\right)\right] \tag{8b}$$

$$\tau_{xy} = \frac{K}{\sqrt{2\pi r}}\left(sin\frac{\theta}{2}cos\frac{\theta}{2}cos\frac{3\theta}{2}\right) \tag{8c}$$

11

where each stress component is labeled in Fig 2.3b. In Eqs. 8a-c, θ represents the angle between the crack plane and the direction of interest, r is the distance from the crack tip to the point of interest, and K is the stress intensity factor. It can also be seen from Eq 8a-c that the stresses near a crack tip are very large due to the inverse dependence on r. Of course, stresses do not truly approach infinity at the crack tip, but the presented stress field equations are accurate for most distances despite this limitation.

Next, the interaction between cracks and dislocations is explored. The stress concentration that exists at crack tips make them favored locations for initial dislocation activity. Dislocation nucleation and motion represent a method for dissipation of the elastic energy associated with a crack tip. Additionally, plasticity produces blunting or rounding of the crack tip, thereby reducing the stress concentration factor.

As the crack tip emits dislocations, they travel a certain distance away but will slow to the inverse r dependence of the crack tip stress field. The furthest extent of the dislocation motion is known as the plastic zone. Any region ahead of the crack tip where the stress field reaches the yield stress (the minimum stress for nucleating dislocations) is within the plastic zone. This is shown in Fig 2.4, where r_y is the radius of the plastic zone [19, 20]. In a perfect elastic-plastic material (with no strain hardening due to interaction of the stress fields of dislocations), this region is incapable of bearing any more stress, so this can be thought of as an extended crack region, even though the crack is not physically there.
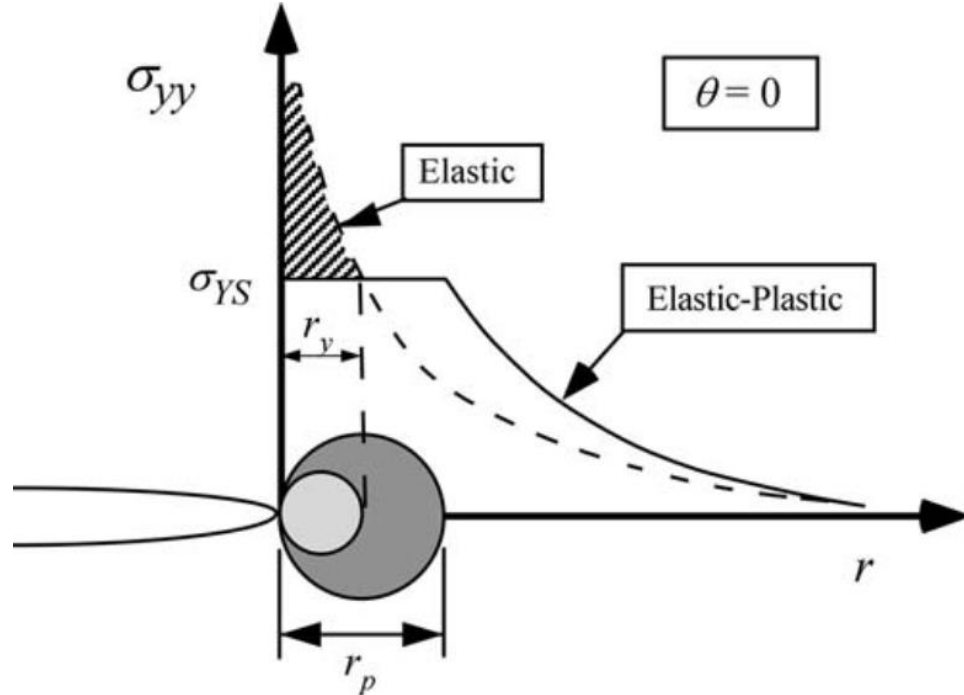
Figure 2.4: Illustration of the fully yielded plastic zone ahead of a crack tip along θ=0°. From T.L. Anderson [18].

The plastic zone size is approximated by Eq. 9a-b, depending upon whether the material is in plane stress or plane strain, respectively [18]:

$$r_p = a) \; \frac{1}{2\pi} \frac{K^2}{\sigma_{ys}^2} \; or \; b) \; \frac{1}{6\pi} \frac{K^2}{\sigma_{ys}^2} \qquad (9)$$

where σ_{ys} is the yield stress. Plane strain vs. plane stress is a state determined by confinement of the material and is based upon specimen thickness such that increased thickness tends towards plane strain. The increased confinement of material surrounding the crack in plane strain results in a more triaxial stress state and suppressed yielding.

One approach for determining U_p is the J-integral [21]. Numerically, J is a strain-energy release rate that is set equal to G, but it is calculated in a special way. J is interpreted as the difference in energy as the crack is extended by an increment through

the specimen by taking a path integral surrounding the crack and summing the total

deformation energy contained within the enclosed area. J is defined as:

$$J = \int_{\Gamma} \left(W dy - T \frac{\partial u}{\partial x} ds \right) \tag{10}$$

where W is the strain energy per unit volume, Γ is the path of the integral which encloses

the crack, T is the stress vector acting on the contour Γ, u is the displacement and ds is an

increment of the path Γ. This type of integral is path-independent, allowing for flexibility

in calculation. Finite Element analysis can be used to determine the stress across the

contour and thereby calculate J. This method is adaptable to the type of testing being

carried out. One common testing scheme is three-point bending, described further in

Chapter 4, with a corresponding J as shown:

$$J = \frac{2A}{Bb} \tag{11}$$

where A is the area under the load-displacement curve, B is the specimen thickness, and b

is the width of the specimen minus the crack length (unbroken ligament).

2.1.3: Ductile-to-Brittle Transitions

A given material might behave in a brittle or ductile manner depending on several

key variables. So called "ductile-to-brittle transitions" (DBTs) are complex in nature and

have important ramifications for the engineering world.

DBT temperature (DBTT) concepts have origins in the thermally-activated

dislocation plasticity models of Cottrell [22] and crack-tip plasticity models of Dugdale-

Barenblatt [20,23]. From a materials science approach, St. John [24] was possibly the

first to discuss definitive activation energy for the DBTT process in single crystals. This was done for silicon, which undergoes a DBTT within a few degrees, known as a hard transition. This was later compared to soft transitions (more gradual) in metallic systems [24, 25]. Over the following three decades various dislocation nucleation [26-28] and dislocation velocity [29-31] controlled approaches using discretized dislocation statics and dynamics were put forth. Although it's unclear whether dislocation nucleation or propagation controls the DBTT in a given material, the two processes have been suggested to be correlated and may in fact be viewed as a singular mechanism from the standpoint of thermal activation. For example, Roberts and Hirsch [31,32] have proposed that dislocation velocity is key to the magnitude of dislocation shielding that can take place. They calculate that the ability to emit subsequent dislocations from a crack-tip or an external source depends on the previous dislocation moving far enough away from the crack tip. This is due to the back-stress field of the previous dislocation inhibiting operation of the dislocation source. This means that the applied stress intensity factor for continued emission would be continually increasing until a critical point where the source operation is no longer favorable. Atomistic simulations using either external dislocation or crack-tip emission sources verified that such approaches could be used to predict the DBTT in silicon [29,33] and Fe-3% Si [34,35]. Furthermore, dislocation mobility was later used as a key variable by utilizing test temperature and strain rate as experimental variables. As a result, similar theoretical and analytical models confirmed the validity of such approaches for tungsten [25,36]. Irrespective of whether crack-tip nucleation has major involvement at the DBTT, it is clear that dislocation velocity will control the number of dislocations emitted. As a result, the magnitude of dislocation shielding of the

stress intensity factor must involve both strain rate and temperature effects on dislocation velocity and arrangement.

The DBTT is higher in materials with a larger Peierls barrier or more boundaries to dislocation motion, due to less available slip systems. The yield stress at which dislocations propagate freely through the material can be described as a sum of two components, $\sigma_{ys} = \sigma^* + \sigma_i$ where the constant internal stress σ_i contains resistance to dislocation motion from obstacles, back stresses and Peierls resistance and σ^* which is rate and temperature dependent. As the temperature drops or strain rate increases, which are coupled due to the statistical distribution of phonons, σ^* is increased, requiring a concurrent increase in σ_{ys}. Eventually a threshold temperature will be reached where brittle fracture will be preferred to plasticity as shown schematically in Figure 2.5 where the fracture toughness shifts concurrently with the change in fracture type.
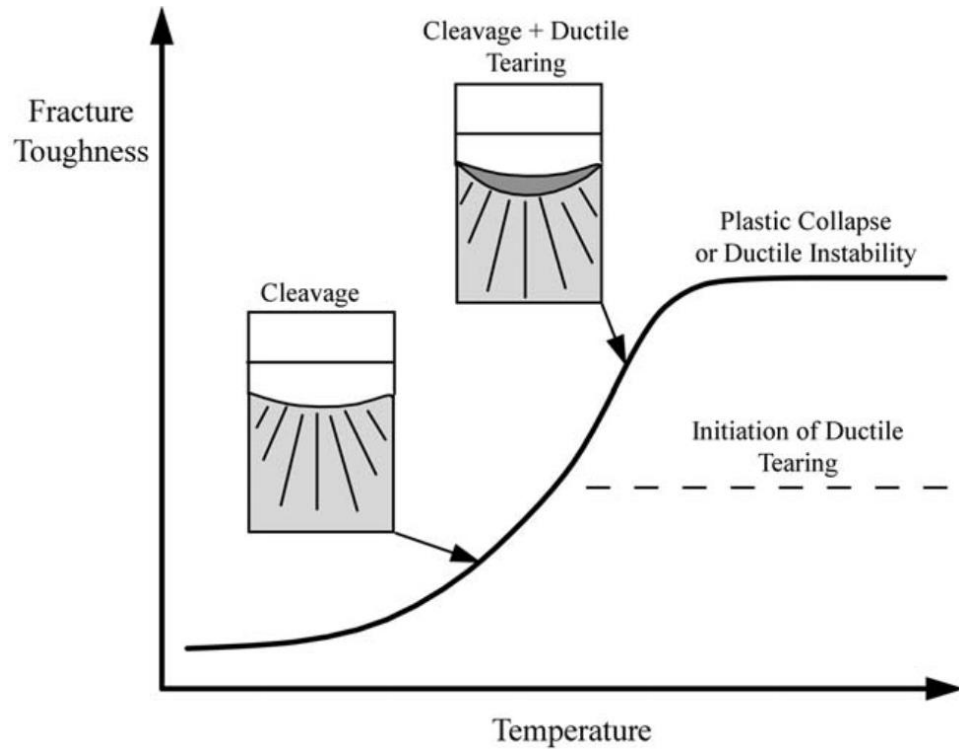
Figure 2.5: Increased fracture toughness due to a ductile-to-brittle transition based on temperature . From T.L. Anderson [18].

Typically, the DBT behavior can be fit using an Arrhenius equation, with a temperature and activation energy in the exponential. This activation energy, *H*, contains the thermal and athermal portions, such that careful measurements as a function of temperature would be able to separate these contributions. The athermal portion is often expressed as the product of a stress and activation volume $\sigma*V*$. Measurement of these activation parameters is critical for understanding deformation behavior, both from a technological and theoretical standpoint.

The presence of impurities can either increase or decrease the energy needed for dislocation nucleation by modifying the Peierls barrier. In the case of metals, impurity effects on the Peierls barrier include mechanisms such as reduced length of dislocation kinks as well as by modifying the atomic bond strength [37,38,39]). In ceramics and

17

semiconductors, impurities that are doped for electronic performance have been shown to lower the activation energy for dislocation motion. Reduction in this activation energy has been shown in Si and SiC by doping with As, P, Sb, and atomic hydrogen [40-42]. In tandem to this, it has been proposed that impurities can modify the surface energy cost for crack propagation. In terms of dislocation propagation, impurities are naturally drawn to crystalline defects and form what is known as a Cottrell atmosphere. This is because impurities possess an energetic cost due to lattice distortion, similar to dislocations, and the energy can be minimized by formation of such an atmosphere. This also results in elastic shielding of the stress field resulting from dislocations, such that the interaction between dislocations and dislocations and crack tips, for example, are reduced, generally resulting in enhanced dislocation velocities and reduced back stress on dislocation sources.

Hydrogen is a particularly infamous impurity, due to its high diffusion rate and being difficult to detect. It was first suggested by Petch and Stables that hydrogen near a crack tip could lower surface energy [43], followed by Tetelman-Robertson-Kunz which described stress-corrosion cracking [44,45]. Next, hydrogen enhanced decohesion (HEDE) mechanism of Troiano-Oriani-Gerberich-Gangloff [46] was proposed for enhancement of brittle fracture. Some propose ductile fracture mechanisms such as hydrogen enhanced localized plasticity (HELP) of Beachem-Birnbaum-Allstetter-Sofronis-Robertson-Lynch [47-52] which was based on observations of enhanced dislocation velocities in the presence of hydrogen.

2.1.4: Size Effects

Materials properties are defined by quantities such as stress and strain, which are normalized with respect to a specimen's dimensions, allowing properties to be size-independent. Despite the convenience of this approach, this is not valid when the size of the specimen is reduced so that it is comparable to the length scale over which the deformation mechanisms operate [53]. When this occurs, new mechanisms become favorable and properties change dramatically. The famous Hall-Petch [54,55] relationship for yield stress exemplifies this as shown in:

$$\sigma_y = \sigma_0 + \frac{k_s}{\sqrt{d}} \tag{12}$$

where σ_y is the yield stress, σ_0 and k_s are materials properties and d is the grain size. This relationship breaks down as grains approach the size of a dislocation loop however, where new mechanisms such as grain boundary sliding may occur, this relationship has been observed to invert. Studies have shown that elastic properties [56,57], initiation of plasticity [58-60], hardness [1,61,62], and fracture [63,64] exhibit length scale effects. They have been observed in thin films, nanospheres and nanoparticles, nanowires, and nanopillars in a variety of material classes. Various mechanisms have been proposed to explain the above phenomena, but what is clear is that the ratio of surface area to volume is important, which can support energetic arguments, geometric arguments regarding dislocation shielding and surface termination and statistical arguments regarding defect distribution.

The classic view of size effects is statistical in nature, where the probability of having a defect aligned to produce a high stress concentration approaches zero as the sample volume is decreased [65,66]. Another mechanism is based on source starvation which was proposed by Nix [67,68]. If one takes a nanopillar as an example, the most

favorable dislocation nucleation site is triggered first at the lowest stress. The load then increases and triggers the next most favorable site giving hardening. This also provides for "mechanical annealing" under low cycle fatigue with a gradually increasing stress, which would push out all the existing dislocations. In a nano-scale volume where the dislocations were unable to terminate at the surface, the back stress would build as the source operates, eventually requiring a new dislocation source which would be less favorable and operate at a higher stress [69].

2.2: Nanoindentation

2.2.1: Conventional Nanoindentation

One thing that rapidly became clear as people sought to understand deformation mechanisms, strength and fracture toughness is that microstructure plays a critical role. In order to probe local properties in a non-destructive way, indentation techniques provide a simple and effective solution. In an indentation test, a sharp probe is pushed into the material with the force measured simultaneously.

Nanoindentation utilizes depth-sensing transducer technology to probe nano and micro scale volumes. The micropillar compression work performed in this dissertation was done using a Hysitron Triboindenter 900 nanoindenter. For this system a quasistatic 3-plate capacitive load cell allows simultaneous measurement of load and displacement, as shown in Figure 2.6a. An AC signal is applied to both the top and bottom plate, so as the indenter moves towards either plate the phase change is used to determine the displacement of the tip, while the signal from the capacitance provides the load.   The

result is a force resolution of ~0.1µN and displacement resolution of ~1nm. This also allows for open and closed loop feedback control of either displacement or load. Additionally, a variety of experiments can be designed by creating a "load function" which specifies either the displacement or load as a function of time using straight lines or sinusoidal segments.
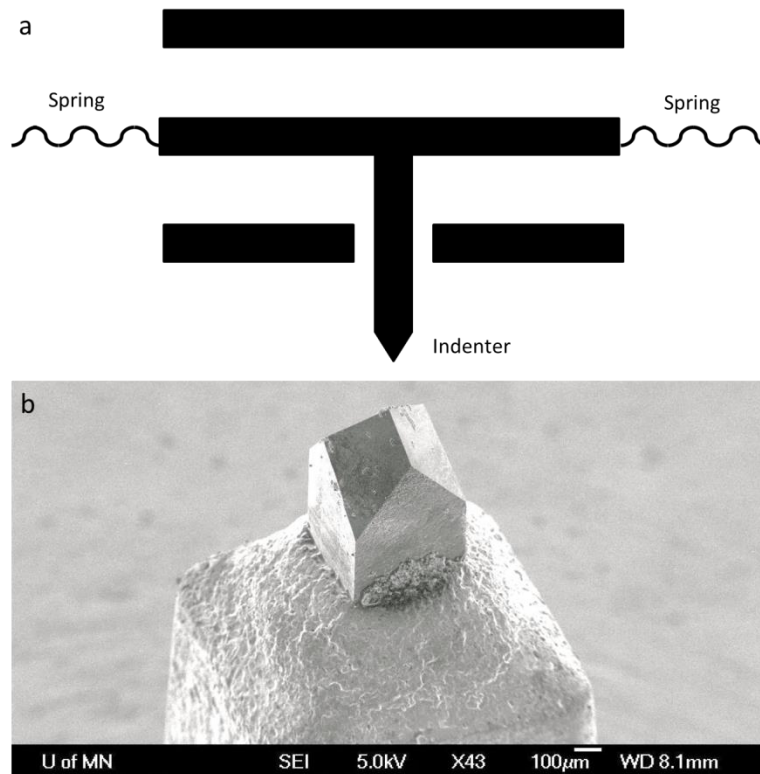
Figure 2.6: a) Schematic of Hysitron quasistatic transducer technology b) SEM micrograph of a pyramidal cube corner tip.

Diamond tips are attached to the end of the transducer and come in various geometries which are specialized for different tasks. The main categories of these are pyramidal, cono-spherical and flat punches. Pyramidal tips, shown in Fig. 2.6b, are the most commonly utilized and are suited for inducing a variety of mechanical behavior in crystals due to the sharp corners including cracking and plasticity. Cono-spherical tips

21

generally are blunter and more suited to studying elastic phenomena, such as viscoelasticity and produce a smoother elastic-plastic transition. Flat punches are notable for having a constant contact area versus depth but are mostly used to compress micro/nano scale objects such as particles and pillars.

For nanoindentation, the tip can be positioned onto points of interest in two different ways. Conventional light optics is used for coarse positioning. The nanoindenter tip itself can be used for fine imaging and positioning similar to a scanning probe microscope (SPM) utilizing a force setpoint, except displacement is measured with the transducer rather than using a laser reflected onto a photodiode as in SPM. The scanning is accomplished using a piezo-tube, which can allow alignment of the indenter with pillars for compression testing. The basic layout of the indenter is shown in Fig. 2.7a.
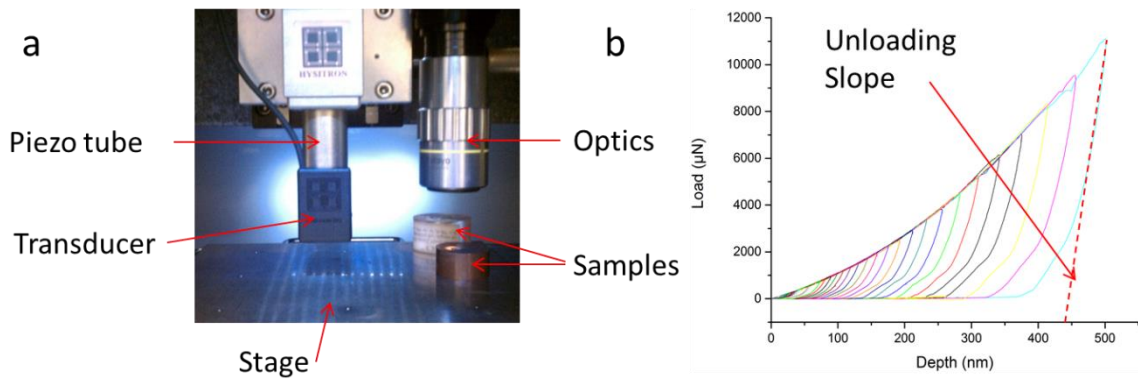
Figure 2.7: a) Hysitron TriboIndenter layout and b) series of nanoindentation curves into silicon with increasing depth.

For general nanoindentation into bulk specimens or thin films, the unloading slope can be analyzed using the Oliver-Pharr method [70-72], based on Hertzian contacts, in order to calculate values for hardness and elastic modulus as shown in Fig 2.7b. The

indenter shape is calibrated by a series of increasing depth indents into a standard sample to produce a curve of contact area versus depth.   The hardness in a nano-indentation experiment is not on an arbitrary scale, but relates to the load, P, required to induce deformation divided by the contact area, A, between the indenter and the sample, $H = P/A$.   Because the state of stress is strongly triaxial compared to conventional uniaxial test methods, comparison between nanoindentation hardness and yield strength from tensile tests, for example, is done by empirical correlation.   For micro/nano compression testing, stresses and strains can be analyzed based on the geometry of the object under study.   In both compression testing and nanoindentation, forces are an elastic series which contains the deformation of the tip as well, such that the measured modulus is called the reduced modulus. Equation 13 describes the reduced modulus of a material:

$$\frac{1}{E_r} = \frac{(1 - v^2)}{E} + \frac{(1 - v_i^2)}{E_i} \qquad (13)$$

where i denotes the indenter, *E* is the elastic modulus, and *v* is Poisson's ratio. Since the indenter material is typically diamond with $E \sim$ 1100-1200GPa, the reduced modulus approximates the elastic modulus well for most materials.

2.2.2: In-situ nanoindentation

The desire to couple the highly sensitive nanoindentation equipment with the enhanced characterization capabilities of electron microscopes has led to the development of *in-situ* nanoindenters in the past decade or so. The tip-transducer-piezo arrangement described in the conventional nanoindentation section is maintained for these techniques,

but the stage/sample mounting differs significantly. Because the scale being studied is typically even smaller than conventional nanoindentation, the transducer technology has evolved to utilize a MEMS-based approach as shown in Fig. 2.8a,b.
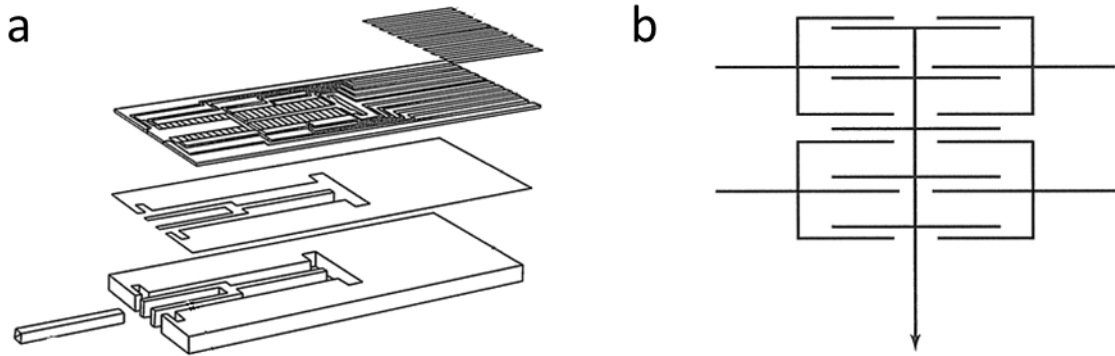
Figure 2.8: a) Schematic of layered assembly of a Hysitron MEMS-based transducer and b) Simplified sketch of the comb capacitor drive unit. From Hysitron patent US 8161803 B2.

Figure 2.8a shows the layered construction of the MEMS transducer and how the tip is inserted into the MEMS springs in the base layer. Overall, the construction is similar to the conventional capacitive transducer except multiple capacitor plates have been micromachined together to form a comb structure as seen in the upper portion of Fig. 2.8a and schematically in Fig. 2.85b. The lower portion of Fig. 2.8a holds the indenter and half the comb structure, which then moves relative to the other half mounted to a silicon chip. Indenter motion is applied via bias voltages and multiple sensing capacitors are used to determine the load and displacement. This design improves the force resolution down to ~20nN and the displacement resolution to 0.2nm.

These *in-situ* nanoindenters are designed for operation in both the scanning electron microscope (SEM) and the transmission electron microscope (TEM). An example *in-situ* TEM nanoindenter, a Hysitron PI-95 PicoIndenter, is shown in Fig 2.9a

and an example *in-situ* SEM nanoindenter, a Hysitron PI-87 PicoIndenter, is shown in 2.9b. For both types of *in-situ* indentation systems, the electron beam enters from above such that the sample and indenter appear on opposing sides in the imaging plane and are aligned in height using focus.
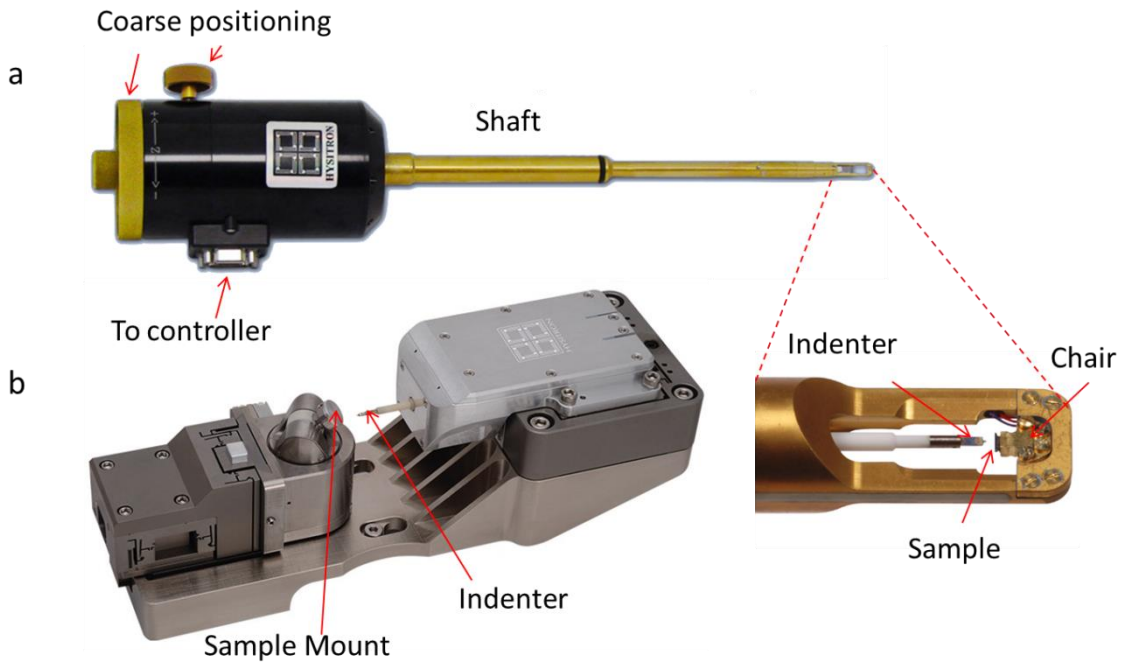
Figure 2.9: a) Hysitron PI-95 PicoIndenter with enhanced view of the indenter sample mount region b) Hysitron PI-87 PicoIndenter.

For a TEM system the sample mounts onto the end of the outer casing via a small screw and bracket piece known as the "chair". The indenter is mounted to the end of a shaft which feeds through all the way to the backend outside the microscope. The indenter can be moved using thee screws on the backend several mm along the indenter axis and hundreds of microns in other two directions. The tip and transducer attach directly to a piezo-tube on the end of this shaft for nm scale positioning, which hidden underneath the outer casing.

For the SEM system, the sample mount uses standard sized SEM stubs. The sample mount moves towards the stationary indenter with some models equipped to do rotation and tilt as the one pictured here. Coarse alignment is accomplished using motorized gears thanks to the larger interior of the SEM and can drive several mm in all directions. The entire PI-87 assembly mounts directly to the SEM stage in the case of large door systems or as a feedthrough unit which is not pictured here.

For all *in-situ* indentation equipment, shadowing from substrates is a concern as slight mistilts can block the region of interest. To prevent shadowing, a narrow and tall substrate is needed , for example lithographically patterned and etched silicon which is ideal for particle or film deposition. Cleanliness is a major concern due to carbon being drawn to the high energy electron beam thereby contaminating the region of interest. Storing samples in vacuum, plasma cleaning, and using vacuum ovens to drive off carbon are all effective measures. Both SEM and TEM are run under high vacuum as a necessity and utilize a variety of vacuum pumps including rotary roughing pumps, turbo pumps, oil diffusion pumps and ion getter pumps. This has some implications for *in-situ* nanoindentation since usually air proves an effective damping agent for natural vibrations in the tip. *In-situ* nanoindenters require special feedback control, called q-control, to damp the vibrations of the tip. Q-control uses the transducer to measure tip displacement for the feedback loop and there only reduces vibrations along the indenter axis. Depending on the sample, these undamped lateral vibrations of a few nm might result in significant unresolved forces due to tip-sample adhesion as discussed in Chapter 3.

In order to acquire high-quality data from *in-situ* indenter systems, proper calibrations, minimization of noise and tuning of feedback loop and applied rates are

crucial. Air indents are necessary to subtract the spring resistance of the transducer from the data, but importantly must be repeated whenever the microscope is tilted. Load and displacement can be calibrated for each session by comparing measured displacements from the microscope to those reported by the indenter. For this to work, crucial parameters such as transducer stiffness and plate spacing need to be accurate and may require recalibration from the manufacturer. Elimination of noise comes in multiple forms, from proper electrical grounding, proper cable alignment with sockets, noise cancellation cones to surround the indenter system and utilizing independent outlets for each component of the system. Selection of appropriate testing rates is largely based on the drift in the system and limitations of the feedback system. The feedback system can be tuned using a step function back and forth motion of the indenter, where higher feedback gains will result in more accurate testing but can lead to feedback oscillations. These oscillations are dangerous for the transducer system, so gradual adjustment is necessary.

The last issue is achieving alignment of the indenter and the specimen. This is done by achieving good focus on the sample, then adjusting the indenter to match the focus. However, this can be challenging considering the scale. Use of a focus wobbler can help get the indenter close, but achieving perfect alignment is ultimately trial and error. One method can be employed where the height is gradually adjusted until you "nudge" the specimen, but this may be limited by delicate samples or desire to keep the indenter tip very clean.

2.3: Electron Microscopy

2.3.1: Electron beams

27

Electron microscopes are divided into scanning electron microscopes (SEM) and transmission electron microscopes (TEM). Both utilize an electron gun, which include thermionic and field emission types, to produce an electron beam which is condensed and focused using a series of apertures and electromagnetic lenses. The theoretical resolution of an electron beam is much higher than that for light, which can be described as:

$$d = \frac{0.612 * \lambda}{nsin\alpha} \qquad (14)$$

where d is the distance that can be resolved, λ is the wavelength of the beam being used, and α is the convergence angle. For light the wavelength is between 400-700nm whereas for electrons the wavelength is velocity dependent. For 10kV typical of the SEM, the wavelength is 12.2pm, whereas for 100kV, typical of the TEM the wavelength is 2.5pm. This theoretical resolution does not take into account beam spread from inelastic scattering or aberrations resulting from astigmatism, energy spread of the electron beam and imperfect focusing of the beam through the lenses.

Electron microscopy is the most popular technique for materials science in terms of characterization of microstructures. This is for a good reason since first it provides excellent resolution for imaging. Secondly, the electron beam interacting with the sample produces an array of deflected electrons and electromagnetic spectra for analysis of both the chemistry and the structure as shown in Figure 2.10. For chemical characterization, characteristic x-rays and transmitted electrons are most important and are used for energy dispersive spectroscopy EDS and electron energy loss spectroscopy (EELS) respectively.

For structural characterization, backscattered electrons are utilized for electron backscatter diffraction (EBSD) in SEM while diffracted beams are used for selected area diffraction (SAD) and convergent beam electron diffraction (CBED) techniques in TEM.
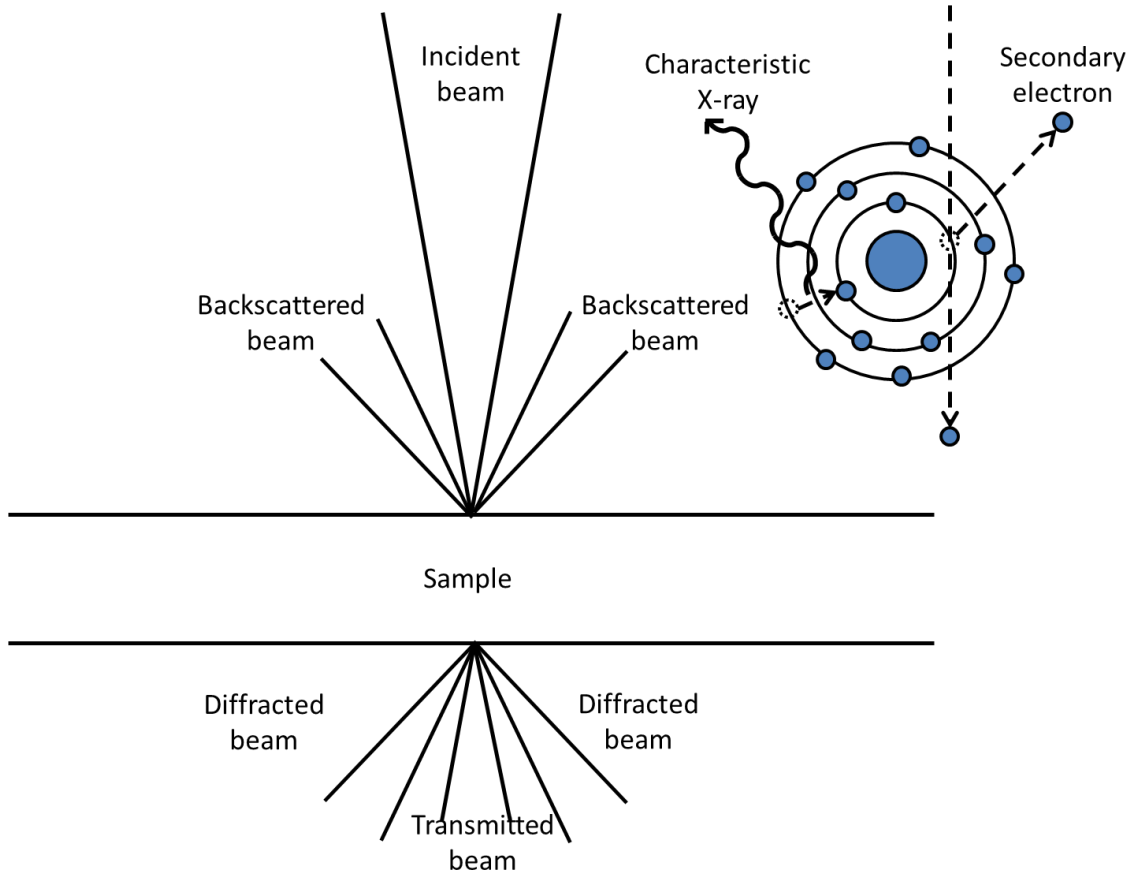
Figure 2.10: Schematic of electron beam – sample interactions with inset showing secondary electron emission and subsequent characteristic x-ray emission.

Electron diffraction is an important phenomenon for both TEM and SEM. Electron diffraction can be explained by a Ewald sphere construction, which is drawn in reciprocal space as shown in Figure 2.11a. Mathematically, reciprocal space can be considered the Fourier transform of real space; therefore every real space lattice has a corresponding reciprocal lattice. In reciprocal space, the effect of short wavelength for

29

an electron beam can be seen as the wave vector of the incident beam, k_i , is massive compared to the reciprocal lattice of the crystal. Here, a sphere can be drawn to represent the possible scattering angles for a beam with a given energy.   Where the sphere intercepts a reciprocal lattice point, a diffraction event occurs where the beam vector at a satisfied diffraction event is labeled k_d. The reciprocal lattice is not truly made up of zero-dimensional points, rather, they are rods or spheres due to excitation error, s. The size of the excitation error corresponds inversely to the sample dimensions, such that a sheet would form a long rod with varying strength along its length. The result of this is that the intersection of the electron beam occurs at various values of excitation error and produces an intensity which varies inversely with the length of the scattering vector, g, on the screen.   This is how TEM diffraction patterns are formed as the SAD pattern shown in Figure 2.11b for austenitic steel, Nitronic 50, a material studied in this dissertation (see Chapter 4).   Another important diffraction effect is known as Kikuchi diffraction.   As can be observed in 2.11b, the diffraction spots have some spread. This is partially due to diffuse scattering due to atomic vibrations, turning a nominally sharp diffracted beam into a cone shape. When these diffuse cones diffract from lattice planes, this results in a dark exclusion line and a bright diffracted line, forming a Kikuchi pattern as seen in Figure 2.11c, also for austenitic steel. These patterns are indexed for EBSD in the SEM to produce orientation maps. Samples of sufficient thickness in TEM also produce Kikuchi diffraction patterns which can be used as a navigational tool for alignment.
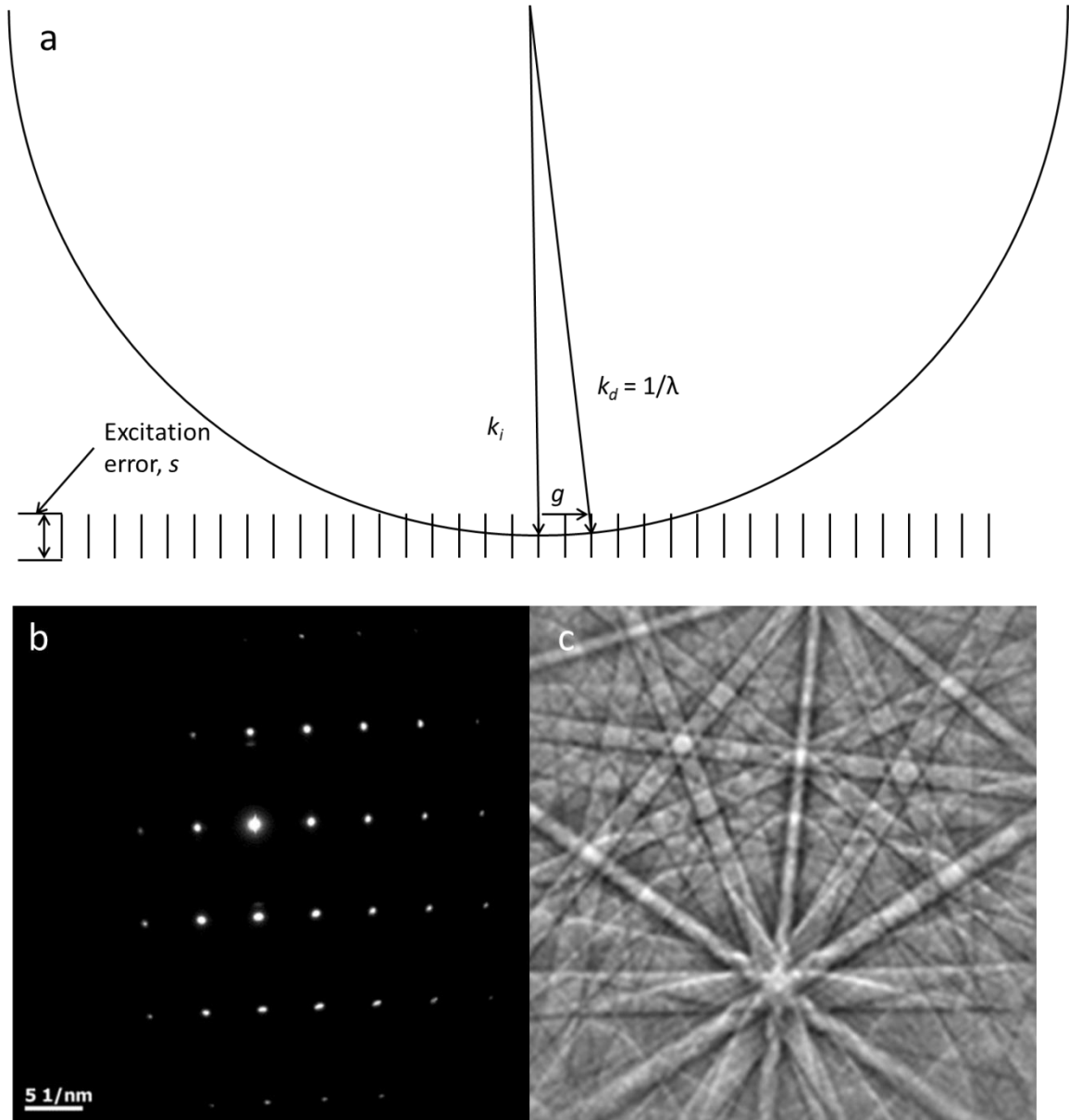
Figure 2.11: a) Schematic of electron beam diffraction based upon the Ewald sphere construction in reciprocal space from relrods due to a thin specimen b) an example resulting SAD pattern (from <110> Nitronic 50 c) Kikuchi diffraction pattern from austenitic steel (from Oxford instruments, ebsd.com).

2.3.2: Scanning Electron Microscopes

A typical scanning electron microscope, a JEOL 6700F, is shown in Figure 2.12a. The basic layout of an SEM consists of an electron gun, condenser lens system, objective lens system, scanning coils, stage and detectors, which is shown schematically in Figure 2.12b. The electron gun outputs a spread beam of electrons with varying energies which is most consistent at the tip of the gun. In order to remove the energy variance and make the beam parallel, a condenser lens system with two or more beam reducing apertures is required. This greatly reduces beam aberrations but does not completely remove them. The objective system and scanning coils are coupled in the column, where the objective system and final aperture are responsible for focusing the beam onto the samples surface while a set of x- and y- scan coils are utilized to raster the beam across the sample. The stage allows the sample to be moved in x, y and z while allowing tilt and rotation. The distance from the final aperture to the sample is known as the working distance and is an important parameter for determining the interaction of the beam with the specimen. Lastly a variety of detectors can be employed including backscatter, secondary electron, EBSD, EDS and more.
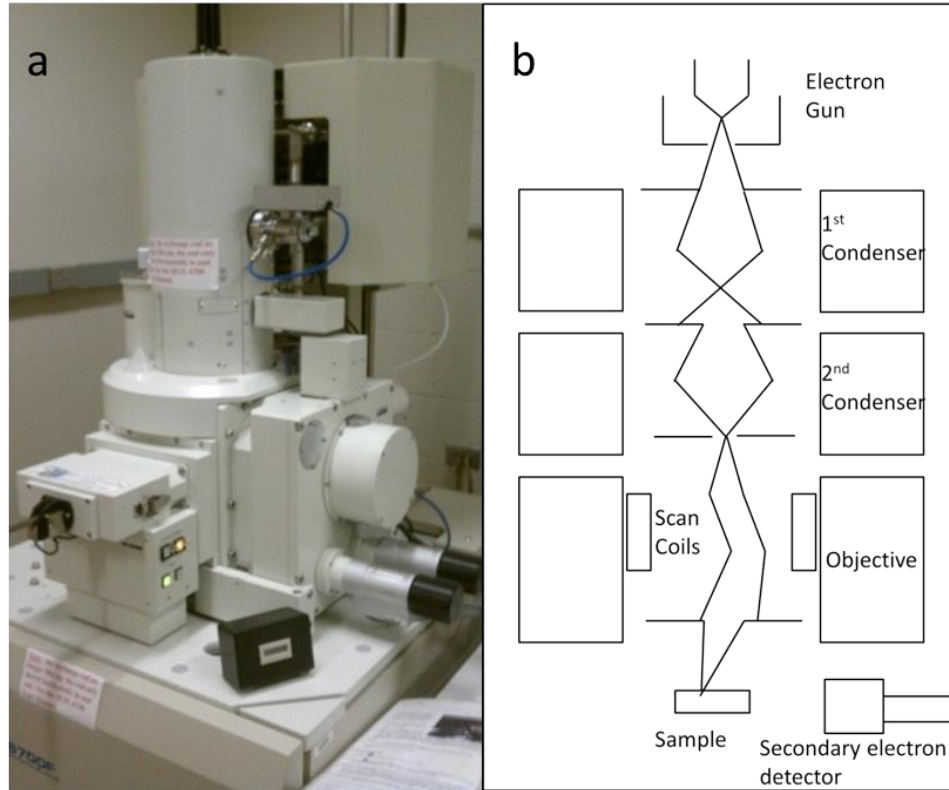
Figure 2.12: a) JEOL 6700 field emission SEM in the Characterization Facility b) schematic of SEM column.

In an SEM, accelerating voltages of 30kV or less are utilized to produce an image in a way similar to a cathode ray tube. This allows the electron beam to interact with the surface of specimen, with the interaction volume as a critical parameter which describes the portion of the sample which produces beam interactions that are able to escape and be detected. The interaction volume primarily depends on the accelerating voltage, beam convergence angle which is controlled by apertures, working distance and the material being studied. The most important signal that is measured is secondary electrons, which are generated by the incident beam donating enough energy to the sample to eject its electrons to the vacuum level. These secondary electrons are gathered by a scintillated

detector. The measured secondary electron yield depends on edge effects such that surfaces parallel to the beam are brighter than normal surfaces, creating contrast that depends upon the topography. When these secondary electrons are ejected from lower energy levels, this requires higher energy level electrons to shed energy and take their place. This energy is shed as characteristic x-rays which are used by EDS to determine local chemistry. In addition, some proportion of the incident beam is diffracted by the sample lattice and/or strongly reflected back towards the source in a process called backscatter. These electrons can be measured by an annular detector and the strength of the backscatter signal depends on the atomic weight of the sample. By putting the sample at a high tilt and using a detector inserted at a complimentary angle, these backscatter diffraction patterns can be gathered. These take the form of Kikuchi diffraction patterns, which are indexed using a database to determine sample orientation as shown in Figure 2.13 for Nitronic 50 where each high symmetry axis, 001, 101, and 111 are colorized resulting in an orientation map of the crystalline grains.
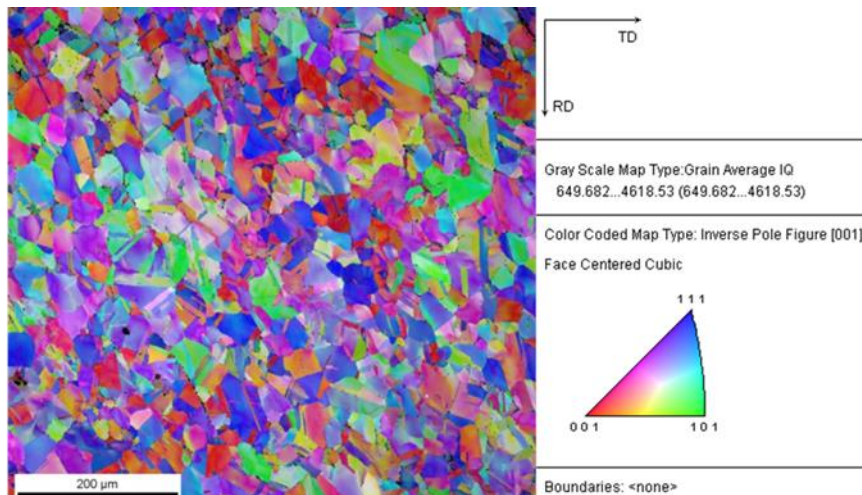
Figure 2.13: EBSD of polished Nitronic 50

2.3.3: Focused Ion Beam

It is common to utilize a dual-beam system where an SEM is combined with a focused ion beam (FIB). FIB is the most popular method employed for fabrication of test specimens on the micron and submicron scale. This is due to its versatility and control over the final specimen geometry. Typically, a Ga+ ion beam is produced using a liquid metal ion source, which consists of a sharp tip with an applied voltage coated in liquid gallium. The FIB instrument, pictured in Fig. 2.14b, can sputter away material from the sample via bombardment with high energy Ga+ ions accelerated with 30kV or less. This is shown schematically in Fig 2.14a. The user can define the geometry of the cuts to any 2D shape they desire, which coupled with the ability to tilt and rotate the sample, allows complex structures to be created. The FIB beam produces ample secondary electrons for imaging purposes and generally can be focused to compete with the resolution of a SEM, however a dualbeam FIB/SEM allows for imaging with an electron beam to avoid unnecessary damage to the sample. A practical concern with FIB milling is redeposition of the sputtered material which results in natural tapering of the cuts of ~2°. This can be compensated by tilting into the wall of the specimen during the final cut.
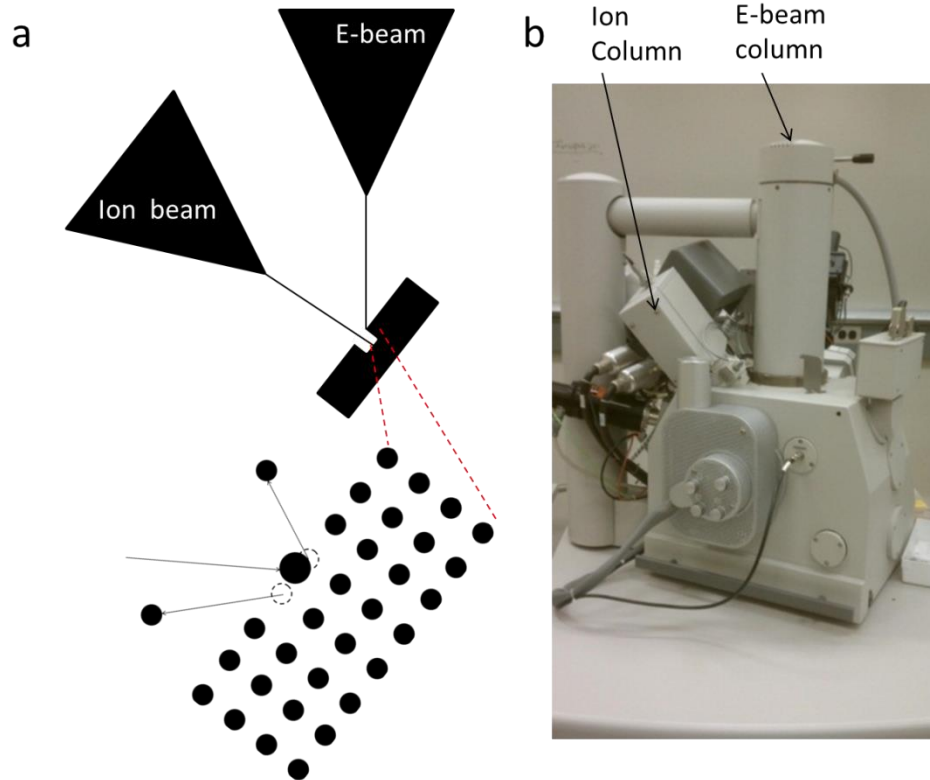
Figure 2.14: a) Schematic of dual beam FIB-SEM with blow up of Ga ions sputtering atoms from the sample b) FEI Quanta FIBSEM in the Nanofabrication Facility.

In order to produce quality structures by FIB, there are several key considerations one must take into account: drift, beam exposure and beam resolution. When performing a FIB cut, one selects the beam current and accelerating voltage as well as the geometry of the cut. Practical considerations require that the drift rate of the stage will dictate the maximum cutting time that can be used before readjustment, which for a typical FIB instrument is 2-3min. This can be improved with better stages, especially in the case of piezo-equipped models. Another way to minimize drift is to allow a few minutes for the stage to settle before cutting, using the beam shift if necessary rather than stage movement. In terms of beam exposure, one can limit damage to the sample through a variety of techniques. First, use of snapshots whenever possible with the ion beam to

track progress is advised. Secondly, when initially orienting/viewing the sample, using the lowest current/voltage combination available that provides adequate contrast. Lastly, alignment of the beam will be necessary but this can be accomplished using a reduced area scan over a non-critical part of the specimen. In terms of beam resolution, generally the resolution increases with increasing accelerating voltage and decreasing beam current. Proper stigmator alignment, focus and aperture alignment is also necessary to optimize resolution, which should be checked periodically. Lastly, beam resolution needs to be kept in mind when trying to achieve high precision final dimensions, as this beam width will extend slightly beyond the assigned pattern.

The subject of Ga damage due to FIB machining is still debated and depends on the material; some have shown little significant effect on mechanical properties while others have shown fairly large effects [73, 74]. There are some techniques to revert or minimize Ga damage [75]. Ga damage can be reduced by stepwise decreasing the strength of the ion beam as the final geometry of the test specimen is approached [76]. One can also utilize deposition of protection layers via a gas injection system which will absorb FIB damage. These gases contain platinum or tungsten which is suspended using organic chains which can be deposited in a physical vapor deposition process using the ion beam. These layers can be then removed at the minimum FIB power later to reduce the amount of damage induced. FIB damage can also be reverted by annealing the Ga out of the test specimen. This approach was introduced by Kiener et al. [77].

2.3.4: Transmission Electron Microscopes

The TEM utilizes much higher accelerating voltages than the SEM, usually 100kV to 300kV in order to achieve electron transmission through the sample. Even with these high voltages, sample preparation requirements for TEM is the biggest limiting factor since specimens of on the order of 100nm thickness are required. Several advantages are gained over SEM techniques however, including higher resolution and much more versatile and powerful diffraction based techniques, including SAD, CBED and dark field imaging. Additionally, use of electromagnetic prisms to determine electron energy loss spectra (EELS) and energy-filtering techniques is another characterization tool.

A typical TEM, an FEI Tecnai F30 is shown in Figure 2.15a. The layout of the TEM column is shown schematically in Figure 2.15b. The upper column layout of the TEM is similar to the SEM in terms of the probe forming with a condenser system and several beam limiting apertures to reduce aberrations. The sample sits within the pole piece of the objective lens which controls defocus as in the SEM. Below, there is an additional diffraction lens and projector lens system which forms the image or diffraction pattern after the specimen-beam interactions take place. The image or diffraction pattern is projected onto a phosphorescent screen which is a rapid imaging method suitable for sample navigation and column alignments. Images can be digitally captured and stored by lifting the screen to allow the image to form on a CCD camera positioned below the phosphorescent screen.
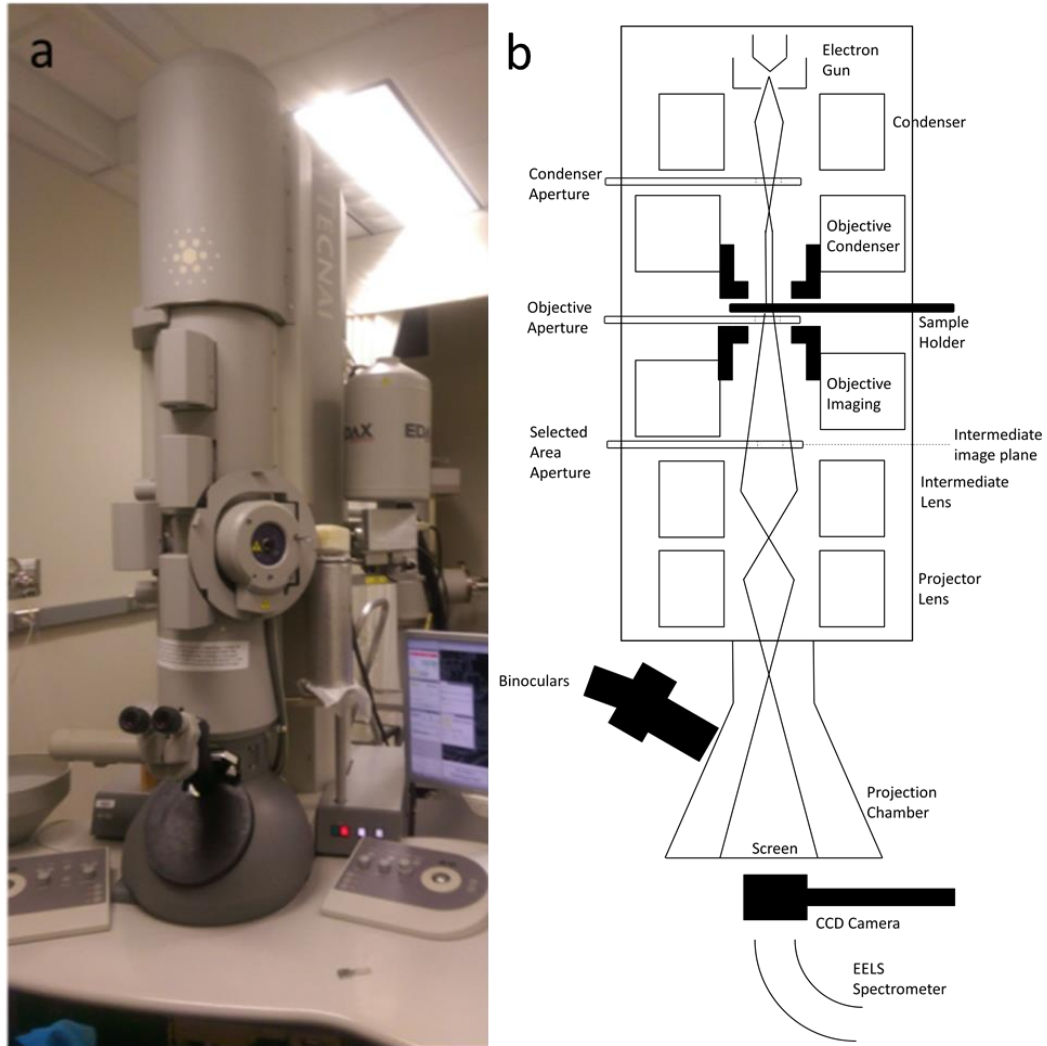
Figure 2.15: a) FEI F30 TEM in the Characterization Facility b) schematic of TEM column.

TEM can be broadly divided into two techniques: conventional TEM (CTEM) and scanning TEM (STEM). In CTEM, a parallel beam passes down the column and through the sample, and after undergoing multiple interactions with the sample is magnified onto the TEM imaging screen. For STEM, a convergent beam is rastered similar to the SEM. While the STEM technique is useful for composition mapping when coupled with EDS and EELS as well as being able to produce Z-contrast maps using

annular detectors to detect scattered beams, it is not favorable for coupling with *in-situ* deformation experiments due to the slow scan rate and is discussed no further.

When viewing CTEM images, contrast features will arise from multiple sources and results in some ambiguity regarding the image viewed on the screen. In crystalline specimens especially, multiple diffraction events can occur during the beam's interaction with the sample before the final image is formed such that imaging and diffraction are always coupled with CTEM. This is a source of complication as well as an advantage for CTEM as compared to SEM, as changing the projector lens strength allows one to switch quickly between diffraction and imaging modes. This gives the user easy access to information regarding the crystallography of the sample being studied. In addition, apertures can be inserted into both the imaging plane and the diffraction plane, the selected area diffraction aperture and objective aperture, respectively. In the image plane, the SAD aperture allows the user to select portions of the sample to contribute to the diffraction pattern, with a practical minimum of approximately 100nm radius. The objective aperture allows the selection of a particular subset of diffraction spots such that multiple imaging conditions can be achieved. Selection of the main beam excluding the diffracted beam is known as bright field, while selection of the diffracted beams is known as dark field as seen in Figure 2.16.
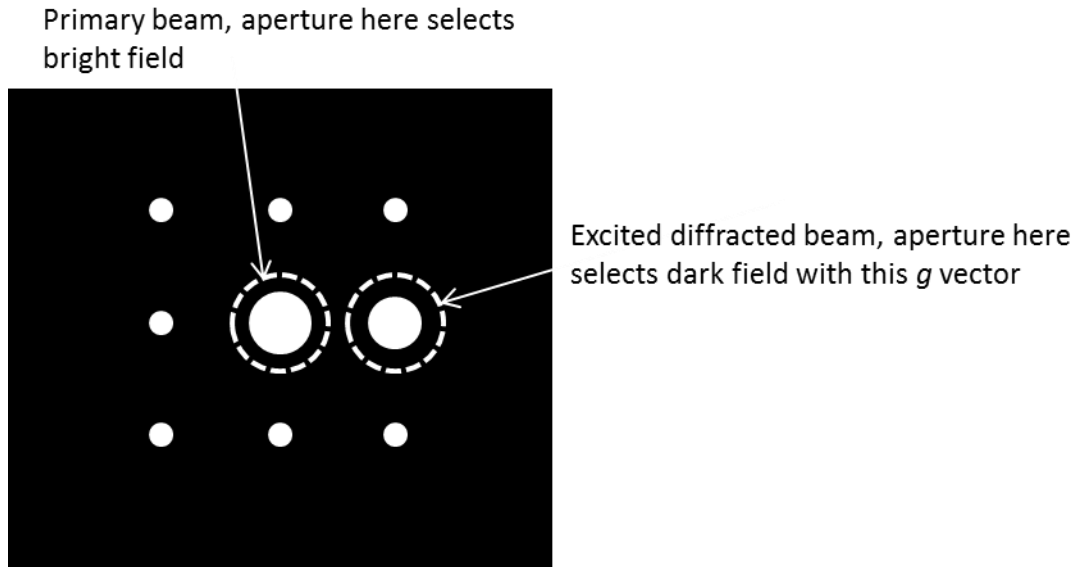
Figure 2.16: Schematic of bright field vs. dark field selection with an objective aperture in a two-beam condition.

2.3.5: Bright Field and Dark Field Imaging:

There are multiple sources of contrast in CTEM imaging including mass-thickness contrast, phase contrast and strain contrast. Understanding the origin of all of these requires a wave-mechanical model of the electron beam and its interactions with the sample [78] but these effects can be described briefly in a practical way. Image simulations are generally required to definitely interpret bright field CTEM; this section emphasizes the complexity of such images.

Mass-thickness or amplitude contrast arises from incoherent elastic scattering (no energy loss) of electrons at low fore-scattering angles of <5°, an effect which increases with sample atomic weight and thickness. Diffraction contrast is related to amplitude contrast except the scattered beams are scattered coherently at specific angles corresponding to the sample lattice. Diffraction contrast or phase contrast results from

the interference of the different path lengths of the transmitted and diffracted beams when recombined to form an image such that the contrast varies sinusoidally on the screen. This effect also explains the origins of Moiré fringes which come from the overlap of different lattices, further complicating the interference pattern. Diffraction contrast can be enhanced versus incoherent mass-thickness contrast by achieving a two-beam condition as shown in 2.16 schematically, where one diffracted beam is excited compared to the others. A two-beam condition is achieved by careful specimen alignment such that the Ewald sphere cuts through one of the g spots at a high intensity point in the excitation error. Strain contrast is due to the local change in lattice spacing due to strain, which results in a different diffraction angle from the unstrained crystal and can be viewed using dark field conditions, described below.

Bright field imaging is performed when the objective aperture is used to select the transmitted or primary beam. This reduces the amount of phase contrast but heightens mass/thickness contrast as well as diffraction contrast. Using a smaller aperture will further enhance mass/thickness and diffraction contrast but could decrease the resolution. When some of the diffracted beams are selected in addition to the primary beam, a phase contrast image is formed.

Strain contrast can be observed in dark field conditions or by selecting the excited diffraction spot and excluding the main beam. This results in defects that do not contribute to that diffraction event to appear dark compared to the perfect crystal which is bright. In order for a dislocation to be excluded from a diffracted beam to produce contrast, the so-called "invisibility criterion" must be satisfied such that $g \cdot b = 0$, where g is the scattering vector and b the Burgers vector of the dislocation. A systematic study

using different g's can allow determination of b based on the invisibility criterion. In order to produce dark field conditions, either the objective aperture can be displaced to select the excited diffracted beam, or the beam tilt controls can be used to bring this spot onto the central axis.

2.3.6: EELS

Electron energy loss spectroscopy is most often coupled with STEM modes due to the ability to produce compositional maps point-by-point. However, there are two applications for an EELS spectrometer to CTEM imaging utilized in the work presented here. The magnetic prism separates the post-sample interacted electron beam by its energy as shown schematically in Figure 2.17.
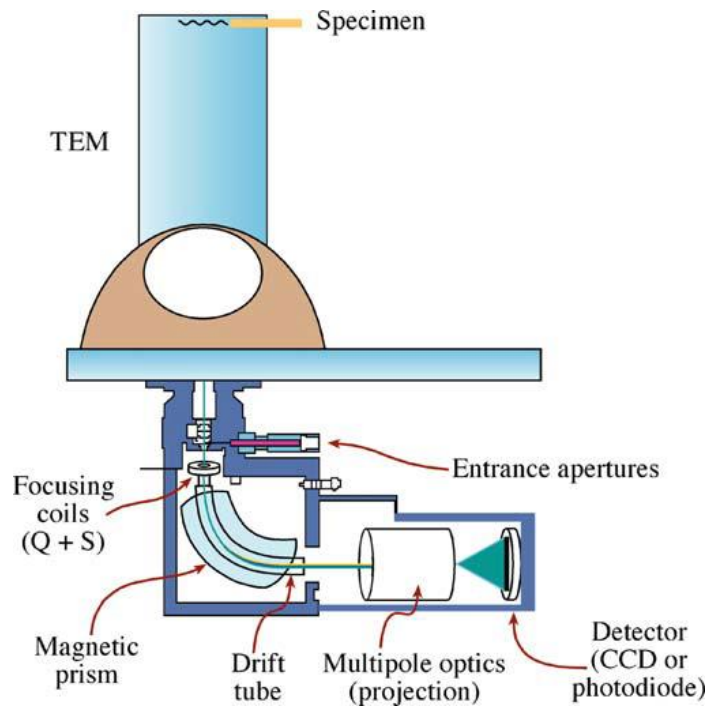
Figure 2.17: Schematic of EELS spectrometer. From Williams & Carter.

A large portion of the beam loses no energy due to inelastic scattering events, known as the zero-loss peak (ZLP). The next peaks observed as one progresses towards higher energy losses are known as plasmon peaks. Plasmons are complicated phenomena that essentially arise due to the electron beam causing vibrations in the electron clouds of the sample. The probability and plurality of these events increase with sample thickness such that a comparison between the intensity of the ZLP and plasmon peaks can provide the number of mean free path lengths in the sample according to log ratio rule: $t/\lambda = ln\left(I_t/I_0\right)$ where λ is the mean free path, I_t is the total intensity of the low loss spectrum and I_0 is the intensity of the ZLP. This becomes accurate measurement of the sample thickness, assuming the material is known since mean-free paths for scattering in many materials have been calculated quantitatively as a function of beam energy and beam convergence angle [79].

The second use for CTEM of EELS equipment is energy filtered imaging. Use of a camera post-prism allows selection of specific energy losses for image formation using mechanical slits which can be adjusted in width. This can allow composition contrast by selecting elemental edges but can simply be used to remove unwanted image contrast from inelastic scattering by filtering down to a zero-loss beam.

Chapter 3: *In-situ* Compression of Silicon Nanocubes

Chapter Overview: Plasma-synthesized nanocubes are compressed *in-situ* transmission electron microscope.   The mechanical properties, deformation regimes and characterization of the plasticity mechanisms are determined.   A dislocation pile-up model is employed to fit the hardening rate in the nanocubes which contributes to understanding of dislocation shielding for DBT models.

Adapted from:

A. J Wagner, E. D., Hintsala, P. Kumar, W.W. Gerberich & K.A. Mkhoyan Mechanisms of plasticity in near-theoretical strength sub-100nm Si nanocubes. Acta Materialia, 100 (2015). 256-265.

E.D. Hintsala, A.J. Wagner, K.A. Mkhoyan, W.W. Gerberich. The Role of Back Stress in Small Volume Strengths. (In preparation)

Collaborators: Andrew J. Wagner, Prashant Kumar

3.1: Motivation

The changes in mechanical response of a diverse set of nanoscale materials compared to their bulk counterparts has created a new challenge for device design while opening doors to new applications [2,80-88]. In silicon, these changes result in a size-based DBT [89] and an increase of the elastic limit [1,90-94]. These effects are promising for a number of critical applications, including transistor optimization. Straining of the channel in silicon-based transistors offer improvements in electron and hole mobility with the potential to increase drive current by two to four times [95]. New device structures (e.g. FINFETs) continue to push these strain-induced improvements [96-98]. Therefore, the maximum achievable strain in these nanoscale crystalline structures without dislocation nucleation needs to be determined.

The atomistic mechanisms contributing to elasticity and plasticity in silicon nanowires have been examined *in-situ* by tensile and bending tests in the TEM [90,99-103]. Under tension and bending conditions, a size-dependence on elastic limit and yielding has been observed in less than 100 nm in length Si nanowires [101,102]. Additionally, Stan *et al.* [103] demonstrated occurrence of a brittle fracture in sub-60 nm-thick Si nanowires at bending stresses of 17 GPa, although the nanowires were found to exhibit some plasticity. On the other hand, Wang *et al.* [100] reported observation of plasticity in sub-50 nm Si nanowires by bending and showed presence of both perfect and partial dislocation post-mortem. However, the origin of the mechanism of plasticity in sub-100 nm Si crystals is still unsettled. It should be noted that the challenge associated with *in-situ* TEM imaging of dislocations in nanowire during such bending experiments is that the orientation and defocus are changing at each step, making images less reliable.

In addition to bending and tensile experiments, mechanisms of plastic deformation in sub-100 nm Si structures can be studied by compression experiments, which often closely resembles strain in devices. Additionally, compression testing is better suited for studying low aspect ratio specimens, which is closer to device dimensions than nanowires and experience less significant changes in orientation and focusing. *In-situ* TEM investigations of plasticity in sub-100 nm structures under compression have been largely limited by experimental challenges with stability of indenter-incorporated holders.

Molecular dynamics simulations performed for the Si nanostructures under compression at low temperature have predicted a variety of mechanisms to accommodate plasticity [104-109]: {111} slip by perfect straight-segmented dislocation loops with burgers vector $b = a/2<\bar{1}10>$ [104,105], the dissociation of these {111} dislocation loops into two partial $b = a/6<11\bar{2}>$ dislocations, {110} slip by perfect dislocations loops with $b = a/2<01\bar{1}>$ [105], deformation twinning [106] and phase transformation [107,108].

Previous work by Garcia-Manyes and Guell [112] and Mook *et al* [64] measured stresses at the indenter contact surface (i.e. contact stress) in nanoscale silicon approaching and exceeding the theoretical strength, $E/10 = 16$ GPa [113]. The measured contact stress of 17 GPa for 1-12nm depth indentations into silicon by a diamond indenter tip mounted to an AFM [112] slightly exceeds the theoretical strength according to the E/10 determination. Compression of 40-140nm diameter Si nanospheres [64] presented an even more compelling case as the measured contact stresses appear to exceed the theoretical strength. In both cases significant plastic deformation was nucleated and the contact stresses are comparable when scaled by the plastically deformed volume. This

was approximated by relating the size of the plastically deformed Si spheres to the calculated plastic zone diameter 4a, where a is the contact radius, of the indented Si.

This suggests that there exists a strong correlation between plastic zone size and contact stress. In both cases theoretical strength level stresses are maintained for plastic zone sizes up to about 60 nm. This originally was explained as a pressure effect [114], however, previous studies have shown that the contact stress should drop as dislocations are nucleated which was not observed in either case [115]. In both cases, substantial plasticity was present and therefore these high strengths cannot be explained by a pressure effect. The presence of previously emitted dislocations exerting an elastic stress on the indenter due to their lattice distortion (a back stress) could explain these high strengths as the measured applied stress would not be the true effective stress for dislocation nucleation and motion. Nanoscale materials displaying near theoretical strengths have been observed for several years [67,110]. However, there has been no discrete analysis of the impact of back stresses on the flow stress, which is the applied stress necessary to maintain plastic deformation.

Here the results of *in-situ* TEM compression experiments on sub-100 nm Si nanocubes performed with a high-stability indenter-incorporated holder are presented. Shown is a clear identification of the onset of dislocation nucleation and propagation, and characterization of plasticity mechanisms. After this a back stress model is utilized for fitting the hardening regime.

3.2: Experimental Methods

3.2.1: Sample preparation

Si NCs were synthesized in a flow-through plasma reactor [116] consisting of a 48 mm diameter, 610 mm long glass tube. Both ends were terminated by grounded ultra-torr fittings. The bottom ultra-torr fitting contained a 6 mm thick stainless steel plate having a small orifice 1 mm in diameter on the plasma side and opening to 4 mm diameter on the exit side. The orifice acts as a convergent-divergent aerodynamic nozzle accelerating the effluent gas and creating an expanding particle beam to which the substrate is exposed. 130 W, 13.56 MHz RF power is applied to a 6 mm tall copper ring electrode positioned 152 mm above the orifice, generating a rotating capacitive filamentary discharge between the ring and lower electrodes and a weak, uniform capacitive glow discharge between the ring and upper electrode. A shutter positioned 50 mm downstream of the orifice controls exposure of the substrate to the particles. The dislocation-free cubic Si NCs were 20 nm to 65 nm in size and had crystallographic facets with slight asperity [117,118].

Sapphire was selected as a substrate in order to minimize compliance effects during compression. The large elastic modulus of sapphire (340 GPa) relative to silicon (160 GPa) results in most of the deformation occurring in the Si NCs. c-axis sapphire squares, 10 mm by 10 mm by 0.1 mm, were cleaned ultrasonically. The squares were then shattered into sub-millimeter pieces. Pieces with sharp tips from the natural cleavage were selected under an optical microscope and mounted on the Hysitron PicoIndenter "chair" using Crystal Bond wax. Silver paste was applied to the base and sides of the sapphire to mitigate charging effects in TEM. The samples were placed in a

vacuum oven heated to 50° C for at least one hour before NCs deposition. Si NCs were deposited across the edge of the sapphire substrate and isolated particles near the sharp tip were selected for compression experiments to minimize shadowing by the substrate in TEM.

3.2.2: Instrumentation

NCs were compressed by a nominally 100 nm flat diamond tip of a Hysitron PI95 PicoIndenter modified for improved lateral stability. Compressions were performed in displacement control mode at a rate of 0.8 nm sec^{-1}, corresponding to a strain rate of about 10^{-2} sec^{-1} to 10^{-1} sec^{-1}. Zero-loss-filtered images were acquired using the Gatan 692 TV-rate CCD (25 fps) of a Gatan GIF 2002 attached to an FEI Tecnai F30 (S)TEM with TWIN pole piece having $C_s = 2.0$ mm and operating at 200 keV. Specimens transferred to the TEM in less than one hour remained nominally oxide-free while delays allowed a 1 nm to 2 nm oxide layer to form. To improve contrast of dislocations nucleated on the {111} slip plane, NCs were rotated for view along the [110] or [$\bar{1}$10] directions. Displacement and contact width were measured *in-situ* and fitted assuming a square contact area to determine the true stress and true strain.

3.2.3: Indenter Stabilization

For the *in-situ* TEM Hysitron PicoIndenter system, a significant portion of the indenter shaft is suspended in vacuum beyond the final point of stabilization and is sensitive to acoustic interference. The vibrations can strongly affect the mechanical data and TEM imaging of particle compression. Such vibrations in contact with a 30 nm

crystal amount to about 0.1 transverse strain for the silicon nanocubes. This strain and the associated stresses have resolved shear stress components contributing to dislocation nucleation which are not measured by the axial load-sensing transducer.

To stabilize the indenter, the shaft was pressed against the wall of the holder near the MEMS transducer, reducing the vibration from 10nm amplitude to below 1nm. The resulting load-displacement data was improved from that obtained by the original vibrating tip, Figure 3.1. Compression of a Si NC with a vibrating tip exhibits numerous load drops of ~2-3 μN which constitutes a substantial portion of the applied load. With reduced vibration operation force-displacement curves show drastically reduced load drops, such that they were virtually indiscernible while also increasing the resolved applied load with respect to displacement.
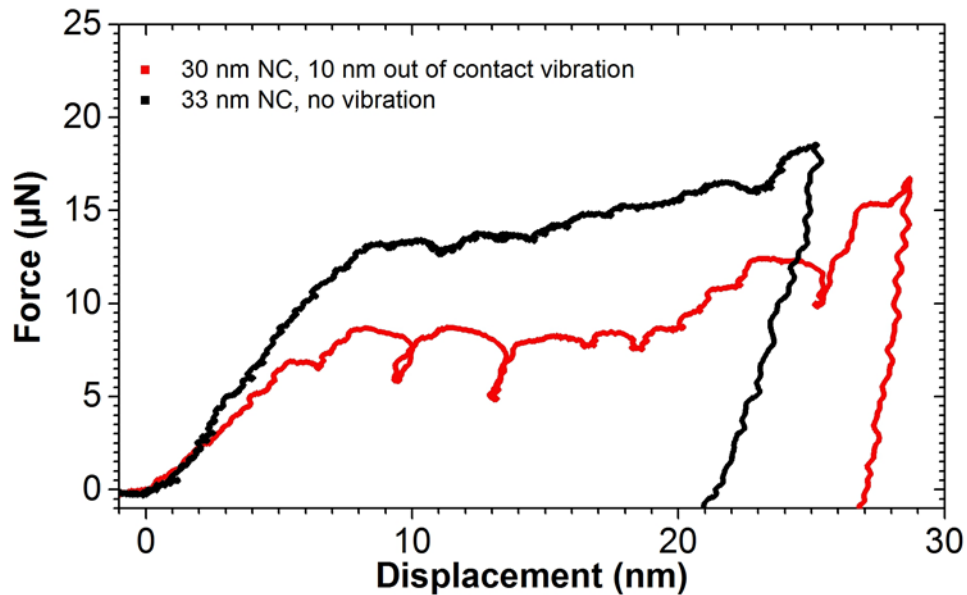
Figure 3.1: Force vs. displacement curves for Si NCs with lateral (out of contact) vibrations (red), and after damping vibrations to less than 1 nm with indenter modifications (black). Load-drops type behavior seen with standard commercial non-vibration-damped indenters could be mistakenly interpreted as pop-in events from dislocation bursts during stable compression rather than unresolved shear stresses contributing to deformation.

After these initial observations, a more refined solution to this issue was introduced using two adjustments. First, the development of a direct-drive coarse adjustment stage by Hysitron reduced the lateral vibrations from roughly 10 nm amplitude to below 5 nm while significantly improving the ability to make small coarse adjustments of indenter position. Secondly, to reduce lateral vibrations further, polyimide foam was inserted with large elasticity, low memory, and vacuum capability between the indenter shaft and holder wall. The small pressure exerted on the indenter shaft was found to reduce vibration beyond detection while simultaneously allowing coarse adjustment of indenter position.

3.3: Mechanical Properties of Silicon Nanocubes

3.3.1: Stress-Strain Analysis

Analysis is simplified by direct-observation of the contact surfaces of NCs compressed on flat {100} cube facets between a diamond tip and sapphire substrate, both materials with substantially higher modulus than Si. Stresses in the center of the particle are much lower than at the contact surfaces, making observation of contact surfaces necessary for accurate stress determination. The stress gradient from the contact to the center of the NCs results from both a slight natural truncation as well as from barreling as compression proceeds due to contact friction. For most compressions, instantaneous particle height and contact width, w_i, were visible throughout the *in-situ* testing, allowing the instantaneous contact stress to be calculated as $\sigma_i = {L_i}/{w_i^2}$, where L_i is the instantaneous load.

In the event that the contact surface was obstructed a displacement-dependent exponential fitting function to model the asperity of the NC surface was employed to determine contact stress. Under assumption of NC volume conservation the effective contact width was approximated as:

$$w_i = w_0 + (d_0 - w_0)\left[1 - \exp(-6\varepsilon_i)(1 - \varepsilon_i)^{-\nu/2}\right] \qquad (15)$$

where w_0 is the initial contact width, d_0 is the initial NC width, ε_i is instantaneous axial strain, and ν is the Poisson ratio. The surface asperity and corrects the contact area at low strains are taken into account here as well as volumetric expansion at large strains. The model reproduces the cases where contact surfaces were visible, as demonstrated in Figure 3.2.
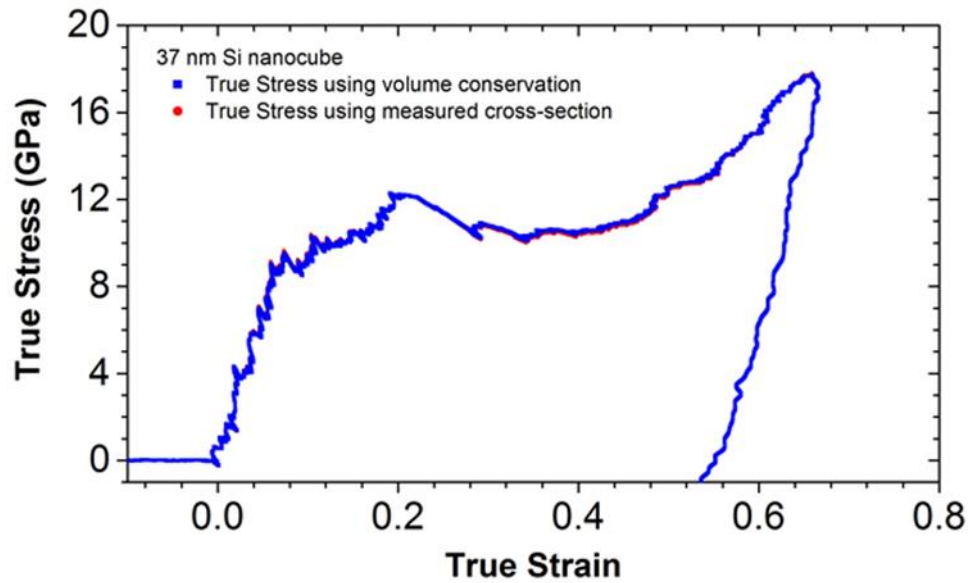
Figure 3.2: True stress vs. true strain curve as determined from instantaneous contact width (red) and using a fitted contact area (blue). The fit matches the experimental curve with only slight deviation in the region of the load drop.

3.3.2: Deformation Regimes

Si nanocubes (NCs), 20 nm to 65 nm in size, were compressed along the $[00\bar{1}]$ direction with acquisition of the load-displacement data. Representative stress-strain curves for four different Si NCs are presented in Figure 3.3. Contact surfaces areas estimated from simultaneously recorded movies were used to evaluate these true stresses and strains.
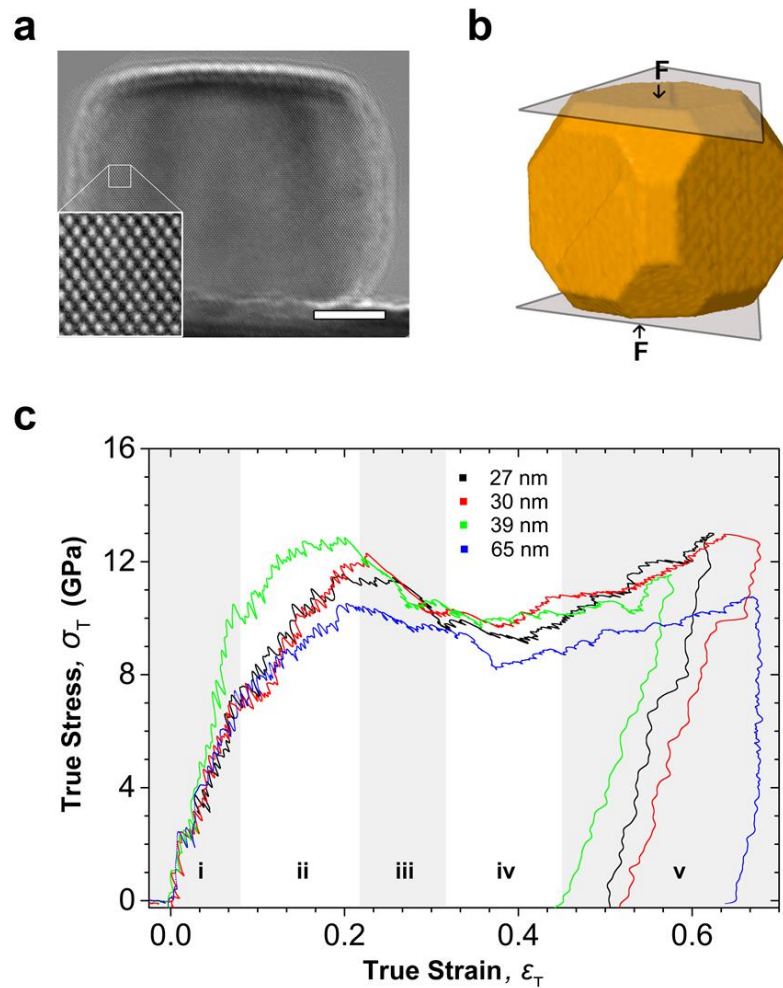
Figure 3.3: (a) HR-TEM image of a 39 nm $[\bar{1}10]$-oriented Si NC on sapphire substrate. Inset shows high-resolution fringes corresponding to $[\bar{1}10]$ orientation of the Si crystal. Scale bar is 10 nm. (b) Schematic illustration of the NC shown in (a), with top and bottom surface representing indenter and substrate. Arrows indicate direction of load application on the NC. (c) Representative true stress vs. true strain plots for NCs of varying sizes showing five distinct deformation regimes.

Five distinct deformation regimes (i-v) are observed in these compression experiments. In regime (i), a linear elastic response was observed upon loading up to the linear elastic (LE) limit at a true strain of $\varepsilon_T^{LE} = 0.07 \pm 0.01$ with a corresponding true stress of $\sigma_T^{LE} = 7.7 \pm 1.1$ GPa and resulting elastic modulus $E = 110 \pm 22$ GPa. In regime (ii), stress continued to increase while slightly deviating from linear elastic behavior until reaching the upper yield (UY) point at $\varepsilon_T^{UY} = 0.21 \pm 0.03$, and $\sigma_T^{UY} = 11.6 \pm 1.2$ GPa. In regime (iii), the upper yield strength was followed by a stress drop, ending at a lower yield (LY) point at $\varepsilon_T^{LY} = 0.35 \pm 0.04$ and $\sigma_T^{LY} = 9.5 \pm 1.2$ GPa. Stress remained relatively constant in regime (iv) up to $\varepsilon_T = 0.45 \pm 0.06$ after which linear work hardening was observed in regime (v) ($0.45 < \varepsilon_T < 0.60$). Upon further compression, above $\varepsilon_T > 0.60$, work hardening changes slightly and often can be described by a power law.

A complete data set of true-stress true-strain curves is presented in Figure 3.4. In part a, compressions into the hardening regime are shown, while in part b, tests that were terminated after the upper yield point are shown (this was done for the purposes of identifying initial dislocation character). Analysis of results from 20 individual Si nanocube compression experiments is shown in Figure 3.5. As can be seen from the Figure 3.5, the data from oxide-free nanocubes and those with native oxide show no identifiable differences. The linear elastic limit ($\varepsilon_T^{LE} = 0.07 \pm 0.01$) in our sub-100 nm Si NCs is about 50% larger than that observed in crystalline Si nanowires with sub-100 nm diameter measured in tension [92,93] or by bending [99-103]. However, the upper yield point $\sigma_T^{UY} = 11.6$ GPa observed here for nanocubes is comparable and approaches the ideal strength of silicon, $E/10 = 16$ GPa [113]. Interestingly, it appears that for these Si

nanocubes, only weak size dependence might exist for ε_T^{LE} and σ_T^{LE} as well as for ε_T^{UY} and σ_T^{UY}. These values appear to increase with decreasing nanocube size down to a size of 32 nm, and then increase with further decreasing nanocube size. However, the size dependence is not strong and requires further measurements.
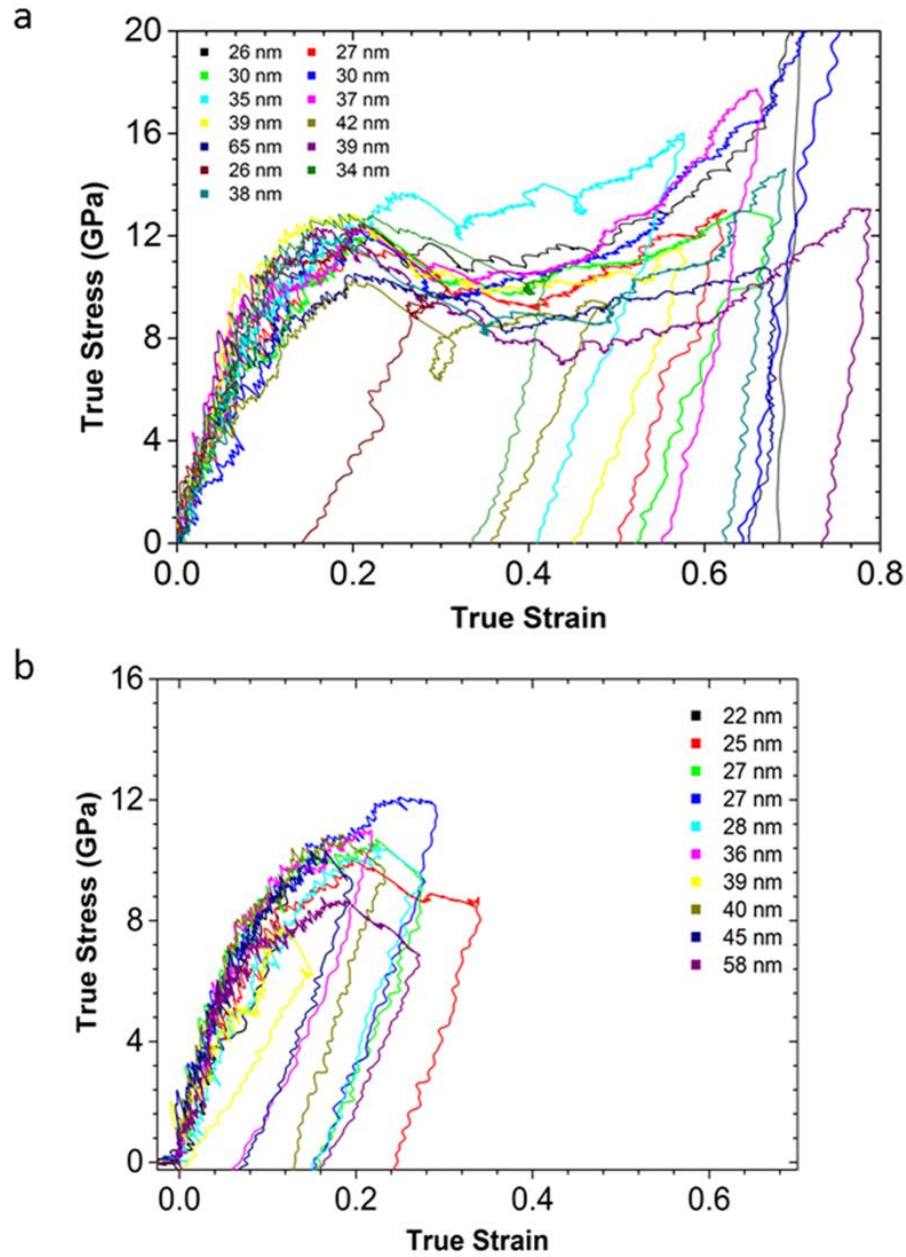
Figure 3.4: (a) True stress vs. true strain curves for [00$\bar{1}$]-compressed NCs of varying size. (b) True stress vs true strain curves for [00$\bar{1}$]-compressed NC of varying size. For post-mortem HR-TEM analysis, the compressions were aborted as soon as dislocation activity was observed.
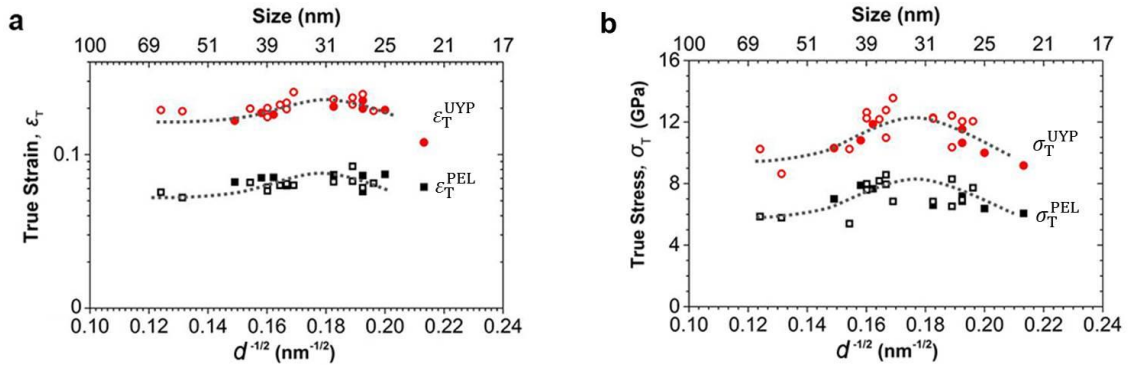
Figure 3.5: (a) True strain at LE limit and UY point as a function of NC size. Large LE strains (black squares) of about 7% ($\varepsilon_t^{LE} = 0.07$) with strains at the UY point (red circles) approaching 20% ($\varepsilon_T^{UY} = 0.20$) are observed. (b) Yield strength at LE limit, σ_T^{LE} (black squares) and at the UY point, σ_T^{UYP} (red circles) as a function of NC size. The σ_T^{LE} approaches 8 GPa and σ_T^{UY} exceeds 11 GPa. Solid symbols are for nominally oxide-free nanocubes while open symbols are for NCs with native oxide. Fitted dotted lines represent possible trend reversal at 32 nm NC size.

A correlation of each region of the stress-strain curve with representative *in-situ* TEM images illustrates the described deformation regimes. Figure 3.6 shows all five deformation regimes of a $[\bar{1}10]$ oriented 39 nm Si NC compression. In regime (i), following initial contact, broad strain contours emanate from the contact surfaces and grow across the NC as strain increases. In this projection the contours are bent, highlighting the asperity of all the NC faces, which includes the {001} faces, the {111} corner truncations and the {110} edge truncations (Figure 3.6g). When viewed along the [100] projection the strain contours appear to be parallel to the contact surface.
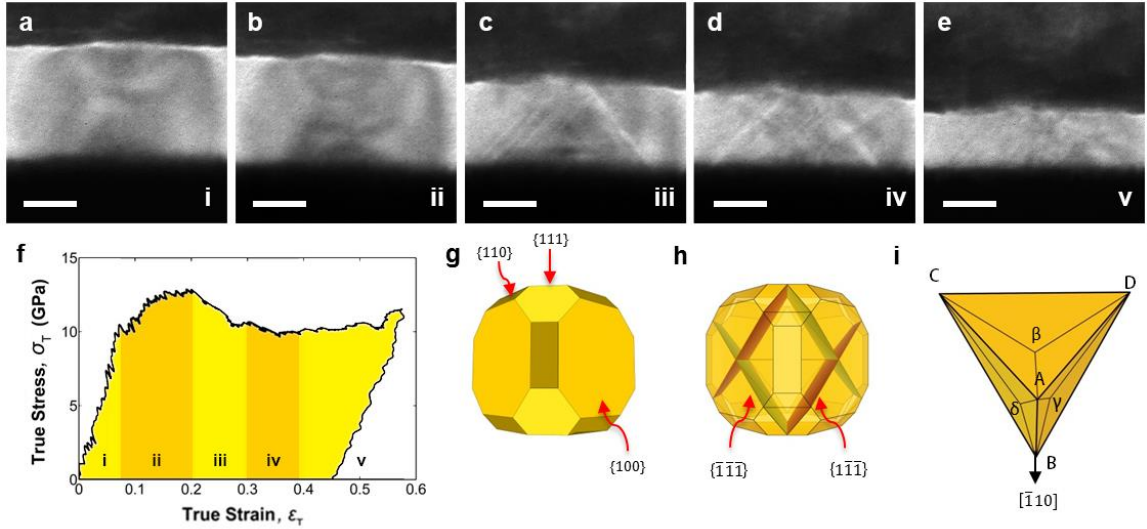
Figure 3.6: (a-e) In-situ TEM image series with its corresponding true stress vs true strain curve (f) for a 39 nm [$\bar{1}$10]-oriented Si NC. (a) The first point of contact of the indenter with the NC. (b) At $\varepsilon_T < 0.07$, symmetric strain contours are observed to extend from the compressed surfaces. (c) Sharp contrast bands on {111} planes appear at the UY point. (d) The bands multiply as strain increases, until (e) complex dislocation activity is observed at $\varepsilon_T > 0.39$. Scale bar is 20 nm. (g) A model depicting the morphology of a truncated 39 nm Si NC with crystallographic planes forming the truncations shown. (h) Inside view of Si NC model shown in (g) with highlighted activated slip planes under [00$\bar{1}$] compression. (i) Thompson tetrahedron explaining the [$\bar{1}$10] viewing projection with the {111} slip planes forming the faces of the tetrahedra.

As compression enters regime (ii) and stress-strain curve deviates from linear-elastic response, irregular contrast is observed near the center of contact on the NC. This irregular contrast suggests the creation of a dislocation embryo during compression in this regime. The first activated slip plane occurs in regime (iii) as bands of contrast along {111} planes (Figure 3.6h,i). They form within one to two TEM image frames (0.04 - 0.08 sec) as the stress reaches its maxima, followed by an observed decrease in stress. Continued compression up to $\varepsilon_T = 0.45$, which is now regime (iv), results in the development of additional {111} bands of contrast. Within this range, the bands of contrast flicker without change in position and significant multiplication, suggesting that plasticity is accommodated through repeated dislocation activity on the same planes.

58

Finally, as the stress increases into regime (v), interlocking {111} bands of contrast form, indicating that the interactions between dislocations result in work hardening. Since image contrast in this regime is complex, no reliable post-mortem information about the different activated slip planes can be extracted.

3.4: Investigation of the mechanisms of plasticity

3.4.1: Particle Shape and Schmid Factors

An additional visual aid for the particle shape, slip planes and possible Burger's vectors is shown in Figure 3.7. As can be observed, the primary facets are {100}, with {111} corner truncations and {110} edge truncations. The truncation of edges and corners leads to the rounded profile of <110>-oriented NCs. Having established that dislocation nucleation is occurring on {111} planes, nucleation of perfect dislocations with $b = a/2<\bar{1}10>$ and dissociated partial dislocations with $b = a/6<11\bar{2}>$ are both possible. For [00$\bar{1}$] compression in Si, the Schmid factor [14] for a {111}<1$\bar{1}$0> slip system is 0.408 for all perfect dislocations not perpendicular to the compression axis, while for {111}<11$\bar{2}$> partial dislocations the two possible Schmid factors are 0.471 and 0.236 (Figure 3.7). This suggests that nucleation of partial dislocations is favored in [00$\bar{1}$] compression since two of the possible {111} slip planes have a higher resolved shear stress compare to a perfect dislocation.

59
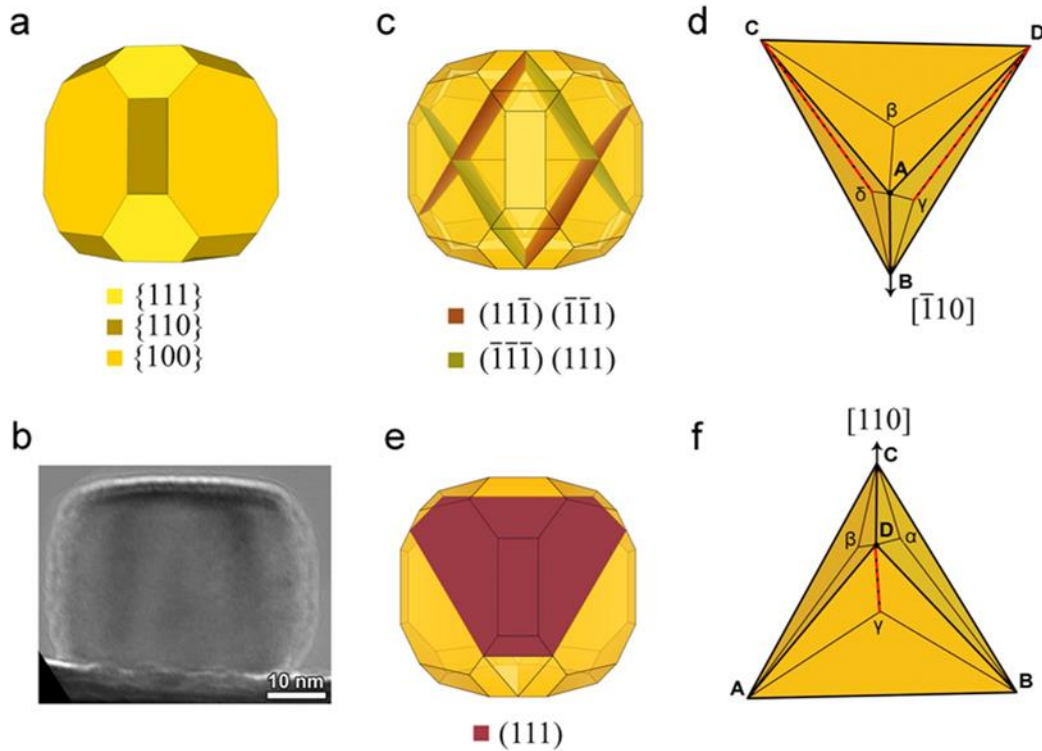
Figure 3.7: Thompson tetrahedron and schematic of slip planes in the Si NCs. (a) $[\bar{1}10]$ projection of Si NCs. (b) HR-TEM image of a 38 nm $[\bar{1}10]$-oriented Si NC. (c) View along the $[\bar{1}10]$ direction with the $(\bar{1}\,\bar{1}\,1)$ and (111) active slip planes and (d) the respective Thompson tetrahedron defining slip planes and slip directions with Greek letters indicating each slip plane. (e) View along the [110] direction with the (111) slip plane highlighted and (f) its Thompson tetrahedron. The directions with highest Schmid factors are highlighted by dashed red line in (e) and (f).

3.4.2: Dislocation Embryo

As discussed earlier, in regime (ii) incipient plasticity is revealed by the formation of a small dislocation embryo near the center of the contact surface (see Figure 3.8a-d) was observed. This embryo is highlighted by Moiré fringes, which terminate approximately 5 nm from the center of the contact surface. The dislocations appear to be nucleated at the UY point along the interface between the embryo and the host crystal. It should be noted that while predicted in atomistic simulations [105,114-116], this is, to the

best of our knowledge, the first reported experimental observation of embryo formation and subsequent dislocation emission from it. It is possible that the embryo could be of β-tin phase Si. Such phase transformations can be induced by hydrostatic stresses as has been observed before in Si under compression [117-122]. Strong friction stresses at the contact surface generate hydrostatic stress at the center of the contact, allowing transformation to the β-tin phase [104]. Wilkins *et al*. [122] have reported β-tin phase transformation in Si under uniaxial compression at around 8 GPa hydrostatic pressure, which is comparable to embryo forming stresses observed here.
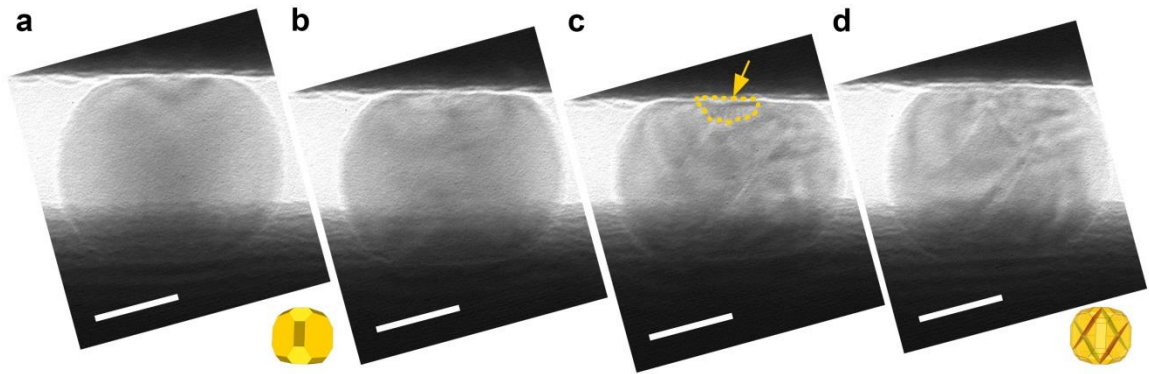
Figure 3.8: In-situ TEM image series of a 45 nm Si NC with [$\bar{1}$10] direction oriented along the electron beam direction and slip planes inclined to the beam direction. (a) Initial contact of the indenter with the NC. A model with orientation of the NC is shown. (b) Further compression of NC leads to development of irregular contrast bands at the indenter-NC interface. (c) A embryo (~5 nm in size) forms at the upper contact surface as the LE limit is reached. The highlighted region shows Moiré fringes at dislocation embryo. (d) At the UY point, {111} contrast develops, extending from the embryo to the opposing corner. Parallel contrast bands form on the lower contact surface as well. A model shows activated {111} slip planes inside the NC. Scale bar is 20 nm.

3.4.3: Dark Field

To investigate the character of initial dislocations formed in regime (iii), additional targeted experiments were performed. Several Si NCs were compressed where the loading was terminated just after the reaching upper yield point (ε_T^{UY}). High-resolution and dark-field TEM imaging were used to characterize the dislocations inside deformed NCs post-mortem. The results for 41 nm Si NC is shown in Figure 3.9a. Bright-and-dark contrast on $(11\bar{1})$ planes can be seen after compression in the bright-field (BF) image (Figure 3.9b). The selected area diffraction pattern obtained after compression (Figure 3.9c) shows two defect-related features: mirroring of spots across the $[1\bar{1}\bar{1}]$ direction and splitting of these mirrored spots into multiple low intensity spots. The mirroring indicates the presence of faulted $(\bar{1}\bar{1}\bar{1})_f$ planes, due to the overlap of misaligned crystal regions, while the splitting of spots indicates of presence of a thin faulted region. This is confirmed by post-mortem by dark-field (DF) TEM imaging with the $(\bar{1}\bar{1}\bar{1})$ and the faulted $(\bar{1}\bar{1}\bar{1})_f$ reflections (Figure 3.9d,e). As can be seen, the $(\bar{1}\bar{1}\bar{1})_f$ reflections correspond to a thin 5 nm region of the NC. Such faults must be formed by nucleation of a leading partial dislocation.
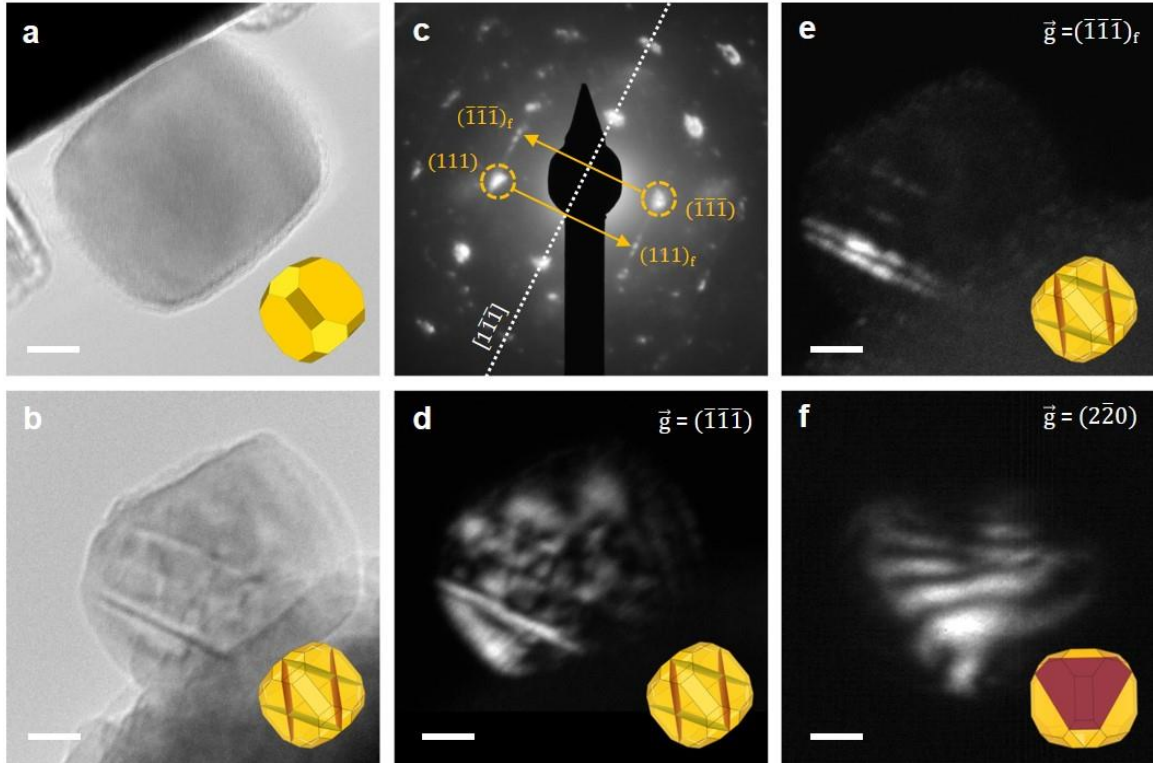
Figure 3.9: Post-mortem DF-TEM images of a $[\bar{1}10]$-oriented 41 nm Si NC under $[00\bar{1}]$ compression. (a),(b) Pre- and post-compression HR-TEM image. (c) Selected area diffraction pattern of the compressed NC shown in (b) aligned such that the indenter contributes minimal diffraction. Circled spots are mirrored about $[1\bar{1}\bar{1}]$ direction indicating faulting on (111) and $(\bar{1}\bar{1}\bar{1})$ planes. (d) Post-mortem DF-TEM image obtained using $(\bar{1}\bar{1}\bar{1})$ reflection showing bright contrast along the faulted region. (e) DF-TEM image obtained using the $(\bar{1}\bar{1}\bar{1})_f$ spot as shown in (c) by the streaked region. Bright region corresponds to the fault planes. (f) In-situ DF-TEM image obtained using $(2\bar{2}0)$ spot when the NC is viewed along [110] direction. This shows the same (111) slip plane shown in (d) and (e) from a different direction. The models in yellow represent the NC and its orientation and the activated {111} slip planes inside it. Scale bar is 10 nm.

Differentiation between isolated stacking faults or twin bands was not possible from these results, since the spatial resolution in DF-TEM images about faulted planes was limited to a few nanometers, similar to the width of potential microtwins [78]. *In-situ* DF-TEM images obtained using the $(2\bar{2}0)$ reflection from a NC viewed along its [110] zone axis (Figure 3.10) revealed Moiré fringes normal to the predicted leading partial dislocation with b = a/6[$\bar{1}\bar{1}2$] or b = a/6[112]. These fringes (Figure 3.9f) can be

explained by crystalline mismatch created by leading partial dislocations on the inclined {111} planes. Calculation of true stress and true strain was challenging due to the decreased visibility of the contact width in dark field, particularly at higher strains, which is why load-displacement is reported. The red-marked Moiré pattern displayed in the fourth frame provides additional evidence of slip by partial dislocations, as shown in Figure 3.9f and Figure 3.10.
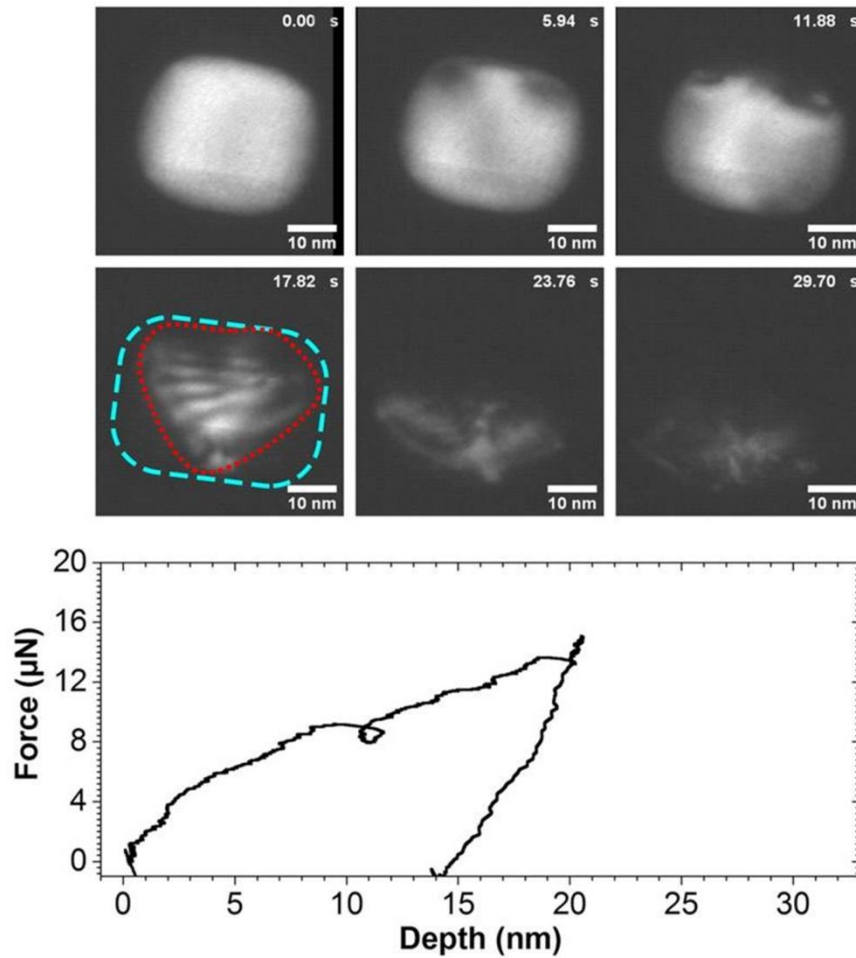
Figure 3.10: (a) In-situ DF-TEM image with g = ($2\bar{2}0$) of a Si NC under [00$\bar{1}$] compression. NC is oriented such that its [110] zone axis is oriented along the beam direction. The full, inclined slip plane, highlighted in red in 17.82 s frame, can be seen starting across the width of the top surface and extending to a corner of the lower surface of the NC outlined in blue. (b) Corresponding force vs. displacement curve.

3.4.4: High Resolution Post-mortem Imaging

Observation of initial {111} contrast in high-resolution TEM image of compressed NCs is also consistent with nucleation of partial dislocations. As can be seen from Figure 3.11a, two bands of contrast extending from the center of the top and bottom contact surfaces towards opposing corners of the NC, respectively. Fourier filtering of the micrograph (keeping only the (111) reflection), as shown in Figure 3.11b, reveals that the outer portions of the crystal are faulted with respect to the center, which is indicative of stacking faults separating the three regions of the crystal. Such stacking faults must be formed by nucleation of a leading partial dislocation.
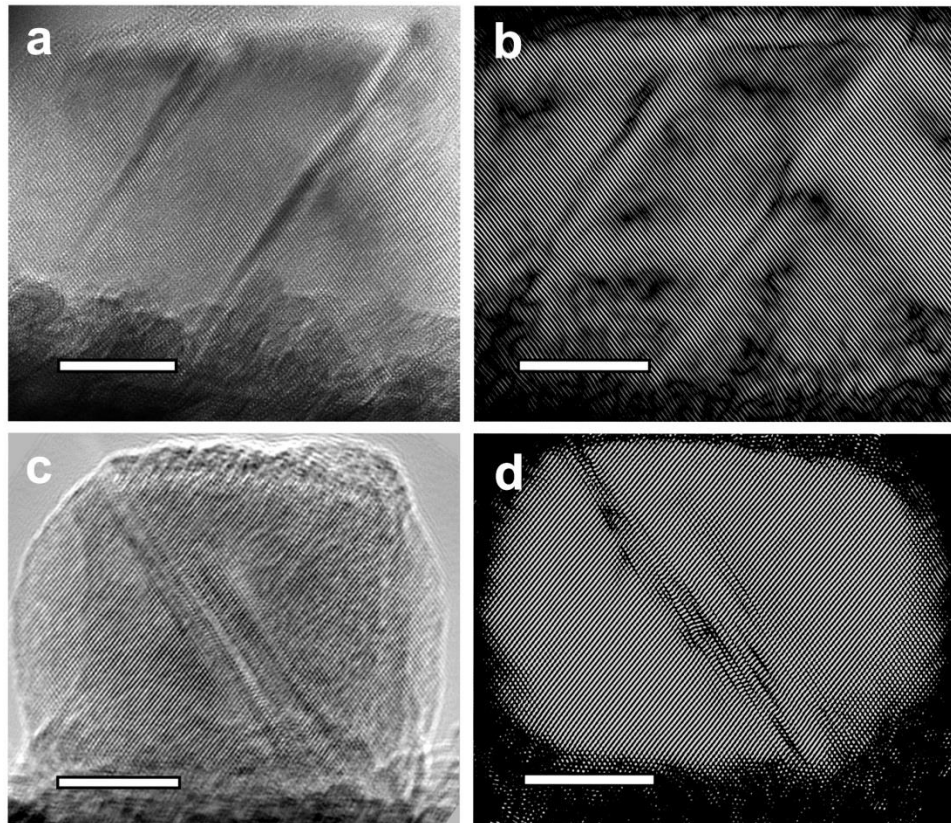
Figure 3.11: (a) Post-mortem BF-TEM image and (b) respective (111) Fourier-filtered image of [$\bar{1}$10]-oriented 36 nm Si NC compressed to the UY point revealing two stacking faults. (c) Post-mortem BF-TEM image and (d) respective (111) Fourier-filtered images of [$\bar{1}$10]-oriented 28 nm Si NC compressed to the LY point. Numerous, closely spaced, stacking faults on its (111) planes can be observed. Scale bar is 10 nm.

Additional compression towards the end of regime (iii) leads to the activation of numerous parallel {111} slip planes (Figure 3.11c,d). No microtwins can be seen here suggesting that nucleation of independent stacking faults is favored over nucleation on adjacent slip planes, i.e. deformation twinning. Furthermore, it was observed that the {111} contrast bands do not appear to multiply considerably prior to hardening, suggesting that the same slip planes are repeatedly slipping. Because the contrast bands also do not disappear, the trailing partials must quickly nucleate and pass through the NC on the same slip plane to allow for subsequent leading-trailing partial dislocation pairs.

3.4.4: Plasticity Mechanism Transition

Having identified $\{111\}\langle11\bar{2}\rangle$ partial dislocations without substantial twinning as the mechanism of plasticity in these NCs, it can be argued that the plasticity mechanism in Si crystals changes at some characteristic length-scale. Conventionally, at high-stress (above 1 GPa) and low temperature (below 400°C), the plasticity in bulk Si is accommodated by the nucleation of perfect dislocations, particularly under large confining pressures [123]. This was also confirmed down to µm-scale by Korte and Clegg [124] using 2 µm Si pillars at 100 °C. These results suggest that a transition from perfect to partial dislocation as the dominant plasticity mechanism occurs at a length scale between micrometer to sub-100 nm.

3.4.5: Multislice Simulations

High resolution imaging of the dislocation core could provide much more definitive answers regarding why partial dislocations are favored at the sub-100 nm scale in compression as observed here. Attempts were made to understand the defect core structure by HR-TEM, however definitive interpretation was not possible due to the non-planar surfaces of the projected NCs, the varying location of the dislocation, and experimental limits of specimen tilting. The lack of a unique solution is apparent when TEM exit wave images for a stacking fault and screw dislocation in these NCs are compared. Multislice simulations [125] of TEM exit waves for perfect screw dislocation and stacking fault in a 37 nm NC are shown respectively in Figure 3.12 and Figure 3.13. Simulation parameters were: $V = 200$ keV, $C_s = 2.0$ mm, pixel resolution was 0.15 Å pixel^{-1} on a 4k x 4k pixel^2 grid. Introduction of 0° to 4° rotation of the NC about the $[1\bar{1}\bar{1}]$ direction was done to account for the slight misalignment observed experimentally. The $(1\bar{1}\bar{1})$ - Fourier filtered images of the Multislice exit waves are shown in Figure 3.14 for a NC containing a single screw dislocation and another NC containing a single stacking fault. Results at 0°, 1°, 2° and 4° tilt show different set of planar fringes, which can be misinterpreted as either partial screw dislocations or partial edge dislocations or 60° dislocations or stacking faults. This ambiguity in observing dislocations by HR-TEM given by the nanocube morphology and experimental constraints should be considered before making any conclusion about the dislocation character.
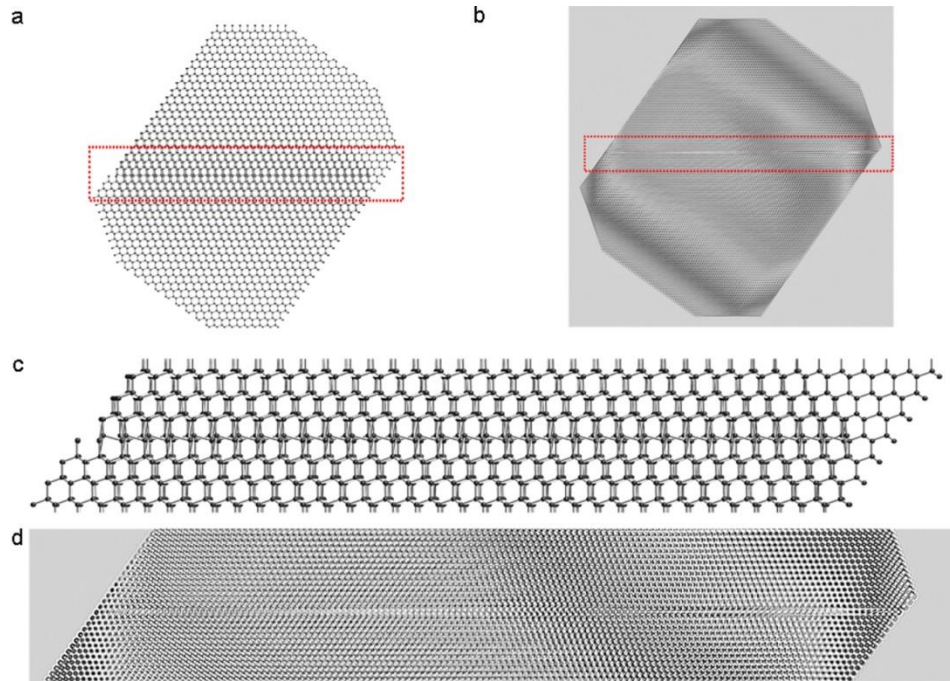
Figure 3.12: (a) Ball and stick model of a single $(1\bar{1}1)[10\bar{1}]$ screw dislocation in a [110]-oriented 37 nm Si NC and (b) the resulting amplitude of the TEM exit wave (V = 200 keV, C_s = 2.0 mm, pixel resolution of 0.15 Å pixel^{-1} on a 4k x 4k pixel^2 grid). (c),(d) Magnified view of the screw dislocation from (a) and (b) respectively.
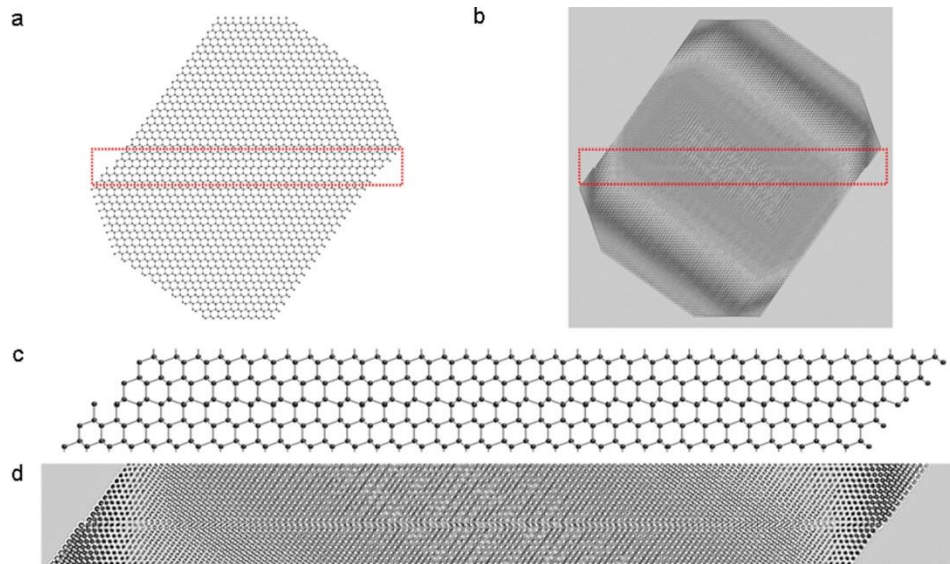
Figure 3.13: (a) Ball and stick model of a single $(1\bar{1}1)[1\bar{1}\bar{2}]$ partial dislocation in a [110]-oriented 37 nm Si NC and (b) the resulting amplitude of the TEM exit wave (V = 200 keV, C_s = 2.0 mm, pixel resolution of 0.15 Å pixel^{-1} on a 4k x 4k pixel^2 grid). (c),(d) Magnified view of the partial dislocation from (a) and (b) respectively.
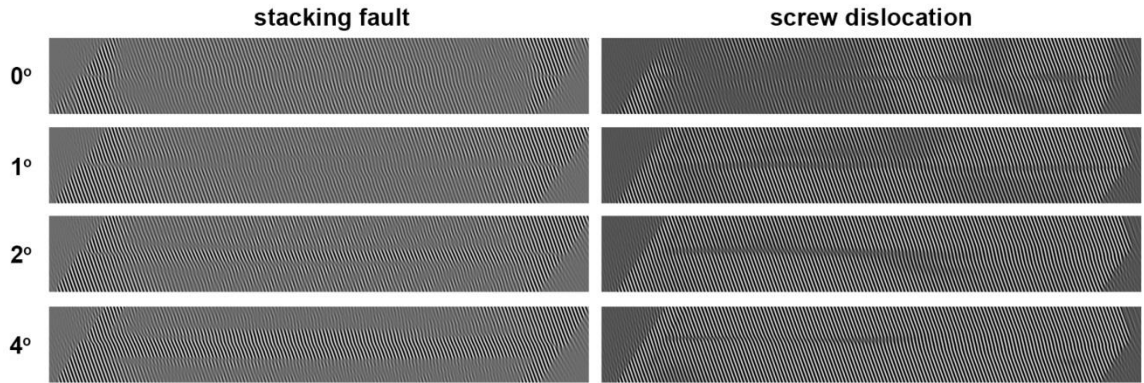
Figure 3.14: A comparison of the $(1\bar{1}1)$-Fourier filtered amplitude of the simulated TEM exit wave (V = 200 keV, C_s = 2.0 mm, pixel resolution of 0.15 Å pixel^{-1} on a 4k x 4k pixel^2 grid) for inclined $(1\bar{1}1)[10\bar{1}]$ screw dislocation and $(1\bar{1}1)[1\bar{1}\bar{2}]$ stacking fault in a 37 nm Si NC. Misalignment of the NC causes the planar fringes to change considerably making interpretation of dislocation character difficult.

3.5: Back Stress Modeling of the Hardening Regime

Nanoscale materials possess an inherent limitation on the number and separation of dislocations within their volume, producing large back stresses relative to the bulk [115,126,127]. Analysis of the discrete contribution of the back stress from dislocations is challenging due to the need for high precision mechanical measurements and imaging, as well as a dislocation-free specimen with a readily interpretable geometry. Here an experimental analysis of contribution of back stresses due to dislocation pile-ups during loading of these single-crystal silicon NCs is presented, which is proposed to be a nearly ideal experiment for studying dislocation back stresses. Selected representative NCs for fitting with a back stress model are shown in Figure 3.15a.
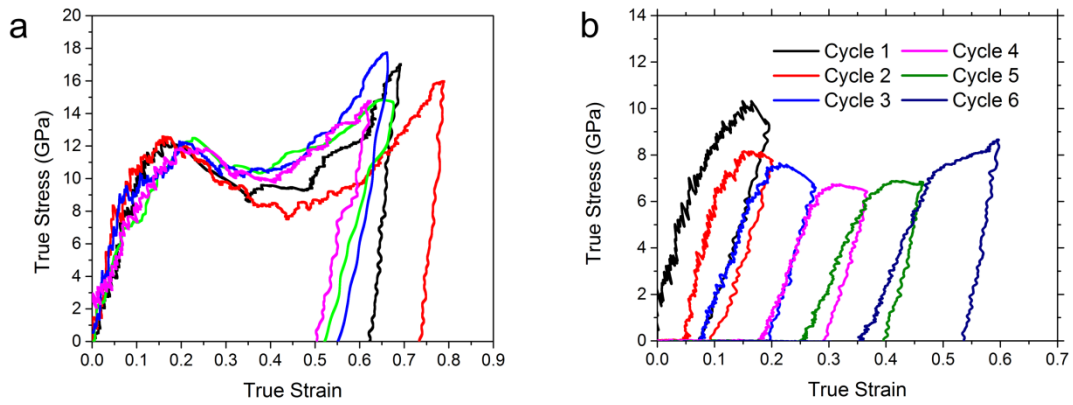
Figure 3.15: (a) True stress vs. true strain curves for selected NCs, all showing identical deformation regimes but with some variance in stress and strain levels for the onset of each. (b) True stress - true strain repeat compression of a 45 nm Si NC in displacement control. NC height was measured between compressions. The first compression was aborted upon observation of {111}-habit contrast. Subsequent compressions were terminated at a target displacement of 5 nm.

3.5.1: Interpretation of Hardening Onset

During the drop from the upper yield point to the lower yield point, it is believed that dislocations are freely terminating at the truncated corners of the NC. This interpretation is supported by repeated compression of a 40 nm Si NC whose stress-strain curves are seen in Figure 3.15b. Initial compression of the NC was aborted at the first sign of yielding, then was repeatedly compressed with displacements of approximately 5 nm. Between each compression the NC height and width were measured and used to offset each curve. The upper and lower yield stresses are comparable to continuous compressions. The mismatch between the unloading NC height at zero load and post-mortem measurement suggests that a significant amount of reverse plasticity, i.e. dislocations reversing their path back to the nucleation surface [128], occurs on unloading. This reverse plasticity means that the dislocations are not trapped and by

70

extension that the NCs are dislocation free at the start of each subsequent cycle until hardening begins.

Back stresses develop in the linear hardening regime as the NC has been deformed to such degree that a fully flat contact is made between it and the indenter and substrate trapping future emitted dislocations as illustrated in Figure 3.16a. This physical interpretation of dislocation confinement would require approximately 33% plastic strain based on the NC geometry, which added to the observed 11% elastic strain matches the observed onset of linear hardening at 45% strain. This estimate of required plastic strain for confinement is based on the observation that the truncations of the NCs resulted in the body and face diagonals to be 1.25 times the NC height.
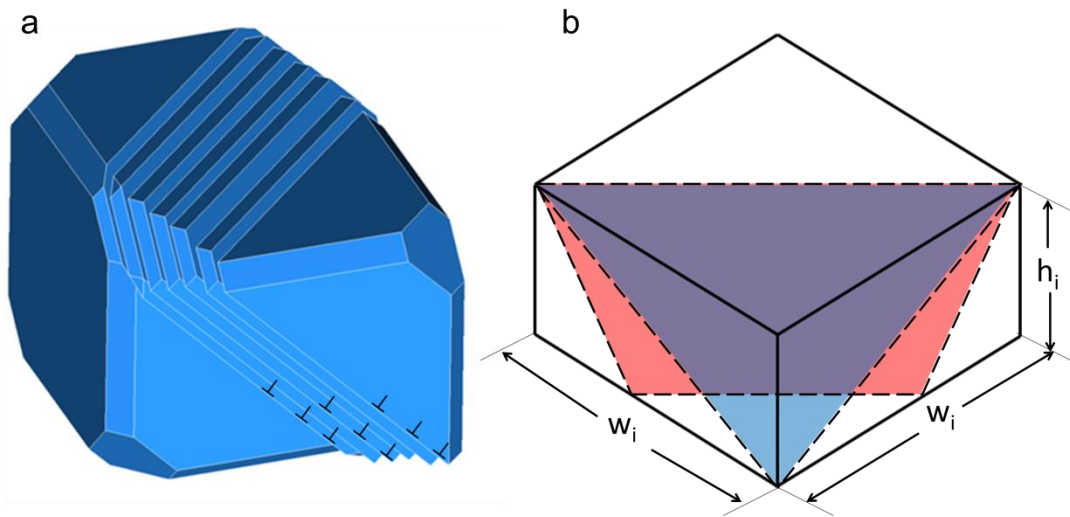
Figure 3.16: a) Illustration showing how a truncated NC achieves confined slip bands after significant plastic deformation. Note this only shows one set of slip bands for simplicity, a more realistic picture would use multiple slip bands to produce homogeneous deformation. b) Illustration of shear area for a compressed cube with two limiting cases, the trapezoidal area in red where the slip plane maintains its original angle and the triangular shear area in blue where the angle changes to its maximum degree.

3.5.2: Development of back stress model

In order to estimate the back stress exerted by dislocations nucleated during the linear hardening regime, a model was developed which was adapted for the specific geometry of these NCs. The Eshelby dislocation pile-up model [129] is given by:

$$\tau_{BS} = \frac{\mu b N_{eff}}{2\pi l_s (1 - v)}. \tag{16}$$

Here, N_{eff} is an effective number of dislocations in a pile-up, μ and v are the elastic constants, b is the Burgers vector and l_s is the length scale of the pile-up.

First, the shear stress needs to be resolved into normal stress acting on the indenter NC contact surface. The shear area needs to be determined, for which two limiting cases are considered, as illustrated in Figure 3.15b. Assuming the slip plane angle remains constant as deformation proceeds the shear area is a trapezoid (shown in red in Fig. 3.15b) which depends on the instantaneous height, h_i, and instantaneous width, w_i, of the NC as:

$$A_S^{tra} = \left(\frac{\sqrt{3}}{2}\right) h_i (2w_i - h_i). \tag{17a}$$

However, some rotation of the slip planes is expected. In the limiting case where the slip plane angle varies to its maximum degree and the corners of the {111} plane remain fixed, the shear area is triangular (shown in blue in Fig. 3.15b) and depends on w_i and h_i as:

$$A_S{}^{tri} = \left(\frac{\sqrt{2}}{2}\right) w_i \sqrt{\frac{1}{2}{w_i}^2 + {h_i}^2}. \tag{17b}$$

The true shape of the slip planes would be somewhere between the limiting trapezoidal and triangular cases described. Multiplying the stress (1) by the shear area (2 or 3) gives the force along the slip direction. With the shear stress, τ_{BS}, equal to half of the normal compressive stress, σ_{BS}, for a uniaxial stress state and resolving the force $F_N = \sigma_{BS} w_i^2$ in the normal direction required to resist the compressive force one finds the force balance:

$$\sigma_{BS} w_i^2 = 2\tau_{BS} A_S \cos\theta. \tag{18}$$

With $\cos\theta$ equal to $1/\sqrt{2}$, $l_s = \sqrt{3/2} h_i$ for the trapezoidal shear area or

$l_s = \sqrt{1/2 {w_i}^2 + {h_i}^2}$ for the triangular shear area, Eqs. (17a or 17b) and (18) can be combined to give the back stress acting over the normal area of the cube face, w_i^2, such that:

$$\sigma_{BS} = F_N \Big/ w_i^2 = \begin{cases} \dfrac{\mu b N_{eff}(2w_i - h_i)}{2\pi(1-v)w_i^2} & trapezoidal \\[2ex] \dfrac{\mu b N_{eff}}{2\pi(1-v)w_i} & triangular \end{cases}. \tag{19}$$

Clearly N_{eff} will need to be estimated not being able to fully characterize the exact arrangement of dislocations or their number. Here, $N_{eff} \propto \varepsilon_{p,confined}$ where $\varepsilon_{p,confined}$ is the confined plastic strain. The onset of the linear hardening regime, $\varepsilon_{0,LH}$ is used as the beginning of confined plastic strain such that $\varepsilon_{p,confined} = \varepsilon - \varepsilon_{0,LH}$ and it is

estimated that $N_{eff} \approx \sqrt{2}\varepsilon_{p,confined}h_0/b$, based on the change in particle height due to the emission of one dislocation.

This model does not directly depend on the dislocation character with the Burger's vector cancelling in the final solution. The presented model is derived for trapped perfect edge dislocations for simplicity even though partial dislocations were observed just after the upper yield point. Additionally, the dislocation character in the hardening regime couldn't be characterized, so this may be reasonable regardless. Furthermore, each pair of partial dislocations would produce a similar stress field to a perfect dislocation with the only difference resulting in the spacing of the pile-up. Lastly, the dislocation character would affect the stress field of each individual dislocation through the (1-ν) factor, with a perfect screw dislocation requiring a change of (1-ν) to 1 and thereby the lowest possible stress field per dislocation.

A few other important considerations exist. It is assumed that dislocations do not mutually annihilate or react to form Lomer locks [130] and dislocations do not escape in the hardening regime through other means such as climb. Additionally, it is assumed that the spacing of the dislocation array does not affect the back stress (which is an effect observed in [131]). Lastly, the choice of μ and ν for a highly anisotropic material such as silicon is not straightforward. The most basic assumption is to use μ=67GPa and ν=0.22 which represents the isotropic averaged values, but directional values could also be utilized, such as values on the {111} plane in <110> directions of μ=62.4GPa and ν=0.22 [132].

It is clear from the *in-situ* imaging that severely constrained plastic flow builds up large back stresses that contribute to the total flow stress. For a constrained volume, it is proposed that the flow stress minus the back stress is a nearly constant effective stress

$$\sigma_{eff} = \sigma_{flow} - \sigma_{BS} . \tag{20}$$

As has been discussed for decades, the appropriate effective stress for dislocation velocities in equations of state should be the applied stress as reduced by a back stress [41,115,133-138]. In these constrained volumes the continued motion of dislocations is limited by the size of the NC and plasticity is controlled by additional dislocation nucleation.

3.5.3: Results of Fitting

The final result is shown in Figure 3.17 where the compressive applied stress is determined from contact areas measured from *in-situ* videos, the back stress is calculated from Eq. (4) for and the difference is the effective stress as indicated in Eq. (5). Calculations are performed according to both the trapezoidal and triangular shear area methods. Additionally, shading for each method is utilized to demonstrate the maximum changes due to variation of μ from 58GPa to 80GPa and variation of ν from 0 to 0.28. The onset of linear hardening tended to occur at stress levels very near the observed upper yield stress, resulting in the mean of the average effective stress for all the analyzed NCs to be 10.22 GPa. For these very small volumes under compression it appears then

that it may not be the initial yield strength that is length scale dependent but rather the flow stress which is back stress dependent in constrained flow. Additionally, it can be argued that the effective stress is that required for nucleating the next dislocation rather than being one associated with dislocation velocities. This would imply that the dislocation velocity controls the strain rate sensitivity [137] and in the present case through the effective stress. Such data will become necessary for appropriate validation of atomistic simulations as the temporal and temperature refinements become a reality [139-141].
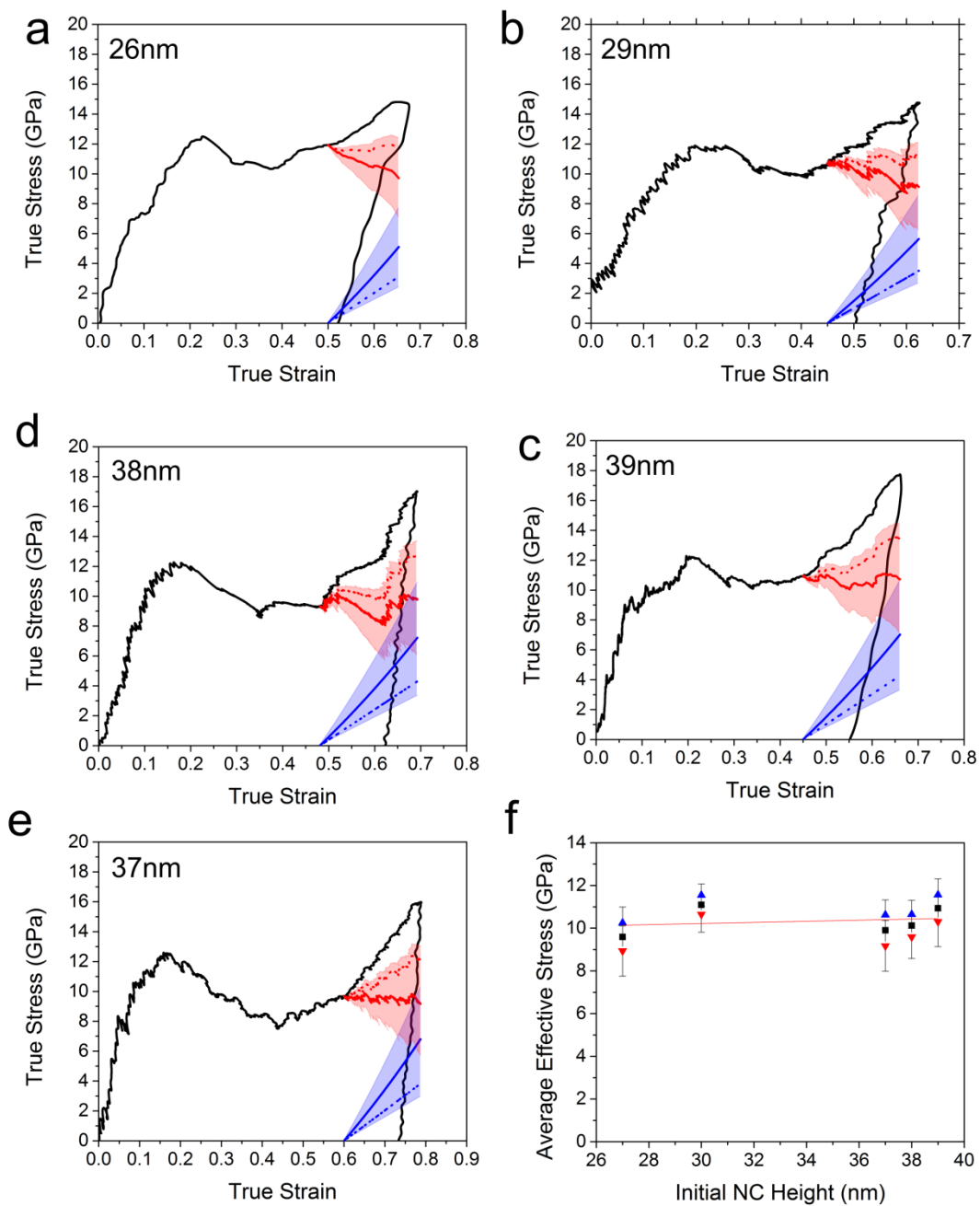
Figure 3.17: The calculated back stress (red) and resulting effective stress (blue) with shading showing the range of fits based on the selection of μ and ν for particles of different sizes is shown in (a-e). Dotted lines represent the triangular shear plane model and solid lines represent the trapezoidal shear plane model with μ=67GPa and ν=.022. In (f), the average effective stress is shown versus size in black squares, with the average for the triangular model in blue triangles and the average for the trapezoidal model in red triangles. Error bars represent the variation of μ and ν.

3.6: Conclusion

Silicon NCs, 20 nm to 65 nm in size range and having {100} facets with slight edge/corner truncation were compressed along the [00$\bar{1}$] direction. The linear elastic strain limit was found to be ε_T = 0.07. Upper yield stresses of 11 GPa at ε_T = 0.20 were observed before plasticity occurs by activation of {111}<11$\bar{2}$> slip systems. A practical size invariance of upper and lower yield stresses, corresponding strains, and elastic modulus were observed over the range tested, suggesting that the reduction of size was no longer a factor for dislocation nucleation and propagation. Dislocation embryos, which appear to be β-tin phase Si, were observed to form and initiate plasticity. The hydrostatic stresses developed at the contact surface due to friction can be responsible for producing these β-tin phase embryos. Substantial plastic deformation by partial dislocations with b = a/6<11$\bar{2}$> slipping in {111} planes was also observed, in agreement with calculated Schmid factors.

Back stress modeling of the hardening rates resulted in an approximately constant effective stress during the hardening regime. This partially explains the high plastic strains achieved, which could be considered surprising for a semi-brittle material like Si, and the late onset of hardening. Back stress models become increasingly important as understanding of mechanical behavior on a fundamental level improves, such as dislocation shielded crack models for the DBT as described in later chapters of this dissertation.

3.7: Future Work: Doped Si Nanocubes

   Recently, new particle reactors have been constructed by the Kortshagen group which enables the synthesis of doped nanocubes of a similar size to the particles presented here. Groundwork to characterize the morphology and defectiveness of different synthesis processes for phosphorus-doped nanocubes has already been performed along with some initial particle compression data. Variations in plasma power and synthesis gas flowrates resulted in a surprisingly diverse assortment of particle morphology, but the best were formed using: 10% doped particles, 0.25sccm SiH4, 0.12sccm PH3, 9.8sccm Ar at 130W power. Two examples of the resulting particles with this recipe are shown in Figure 3.18a,b. As can be seen, these particles are no longer cubic, possessing more facets than the previous Si cubes. Additionally there is a small discrete number of preexisting defects, especially for larger particles as can be observed in Fig 3.18b.
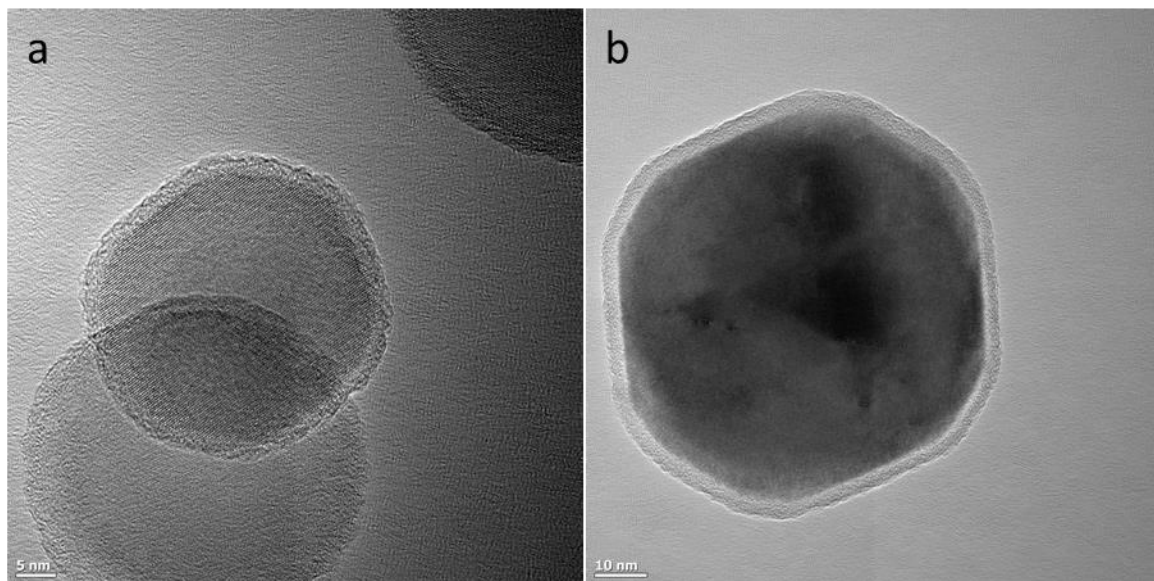
Figure 3.18: High-resolution bright field TEM of two 10% P-doped Si NCs a) a smaller and apparently defect free NC and b) a larger NC with native defects.

A doped particle compression experiment is shown with a composite of true stress- true strain data and video frames shown in Figure 3.19a-f. It is worth noting that the indenter-particle alignment is not ideal and portions of the contact surfaces are hidden as the compression proceeds which coupled with the more complex morphology dictates some caution. The full compression curve is not analyzed as the particle becomes too obscured by the point of unloading. It can be seen that the particles undergo a similar upper-lower yield phenomenon as the undoped particles with a fairly close match in strain levels for the occurrence of each. The displayed particle appears to have a reduced lower yield stress compared to the undoped particles, resulting in a stress drop during the progression from upper to lower yield of 5-6GPa versus 3-4GPa on average for the undoped particles. The effects of phosphorous doping on silicon have typically shown enhanced dislocation mobilities at high stresses [142,143] due to the elastic shielding effect of the dopant atmosphere which could explain the enhanced drop from upper to lower yield as dislocations begin to cascade. This enhanced mobility also is believed to be partially due to a reduced Peierls barrier, so why there is not a reduction in the upper yield stress is unclear at this point. Further compression experiments, especially ones with better indenter alignment and more careful characterization of the plasticity mechanisms and particle geometry as was done for the undoped particles would provide many answers. Furthermore, the comparison in dislocation energetics between the doped and undoped particles would have a large impact on modeling efforts and the current understanding of dislocation energetics in general.
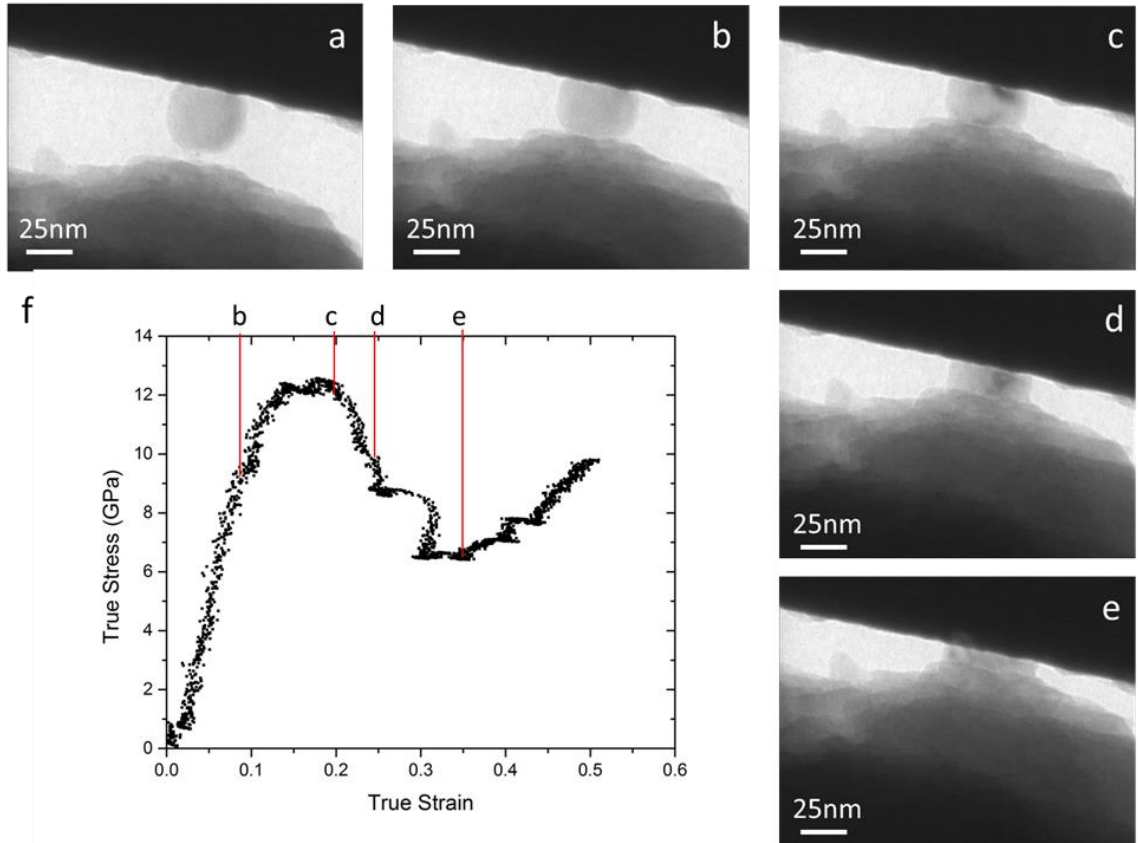
Figure 3.19: (a-e) Montage of 10% P-doped NC compression showing strong contrast likely associated with dislocation activity in c, d and e and f) the corresponding partial true stress – true strain data.

Chapter 4: *In-situ* Pre-notched Fracture Testing by Bending

Chapter Overview: A new experimental method for measuring fracture toughness *in-situ* the SEM and TEM is explored. Studies are performed for a model ductile material, Nitronic 50, an austenitic stainless steel and a model brittle material, silicon. This chapter follows a progression in techniques, experimental and analytical, needed to develop accurate fracture testing methodologies which can be employed at the nano/micro scale while simultaneously providing good visibility of cracking processes.

Adapted from:

Hintsala, E., Kiener, D., Jackson, J., & Gerberich, W. W. (2015). *In-Situ* Measurements of Free-Standing, Ultra-Thin Film Cracking in Bending. Experimental Mechanics, 1-10.

Collaborators: Daniel Kiener, John Jackson, Roberto Ballarini

4.1: Motivation

Two materials are studied in this chapter: a model ductile material, Nitronic 50, and a model semi-brittle material, silicon.

For silicon, failure of MEMS/NEMS devices [144,145] and delamination in microelectronics [146,147] is a continuing concern as these technologies mature. Devices continue to shrink, forcing the same current through smaller channels which may result in more local heating [148-151] and requiring increased applied strains to achieve the necessary mobility for device performance [95-98]. From an industrial standpoint, developing methods to measure fracture toughness at these scales as well as characterize the crack propagation mechanisms are needed to continue to improve optimization and reliability. The effects of doping, temperature and strain rate all need to be considered.

In addition to this, considerable ranges of opinions about the DBT in single crystal silicon have arisen over the last few decades [64,89,123,152-157]. Recently, interest in this topic has increased due to a number of findings of room temperature plasticity in silicon at the nanoscale [64,89,123,152-154,157]. In compression this can lead to plastic strains of over 50 percent at 300K without fracture as was demonstrated in Chapter 3. Though compression testing has the least favorable stress state for brittle fracture, some tension and bending experiments have also demonstrated large plastic strains [92,100,102]. Excellent progress has been made in understanding the high temperature (800°C) DBT in silicon using phenomenological power laws that, when coupled to mechanics or atomistic simulations give realistic representations [155,156]. The low temperature, i.e. below 300°C, DBT in silicon has not yet been characterized to

a similar degree. It has become generally accepted that it is the ease of dislocation nucleation and/or mobility at very high stresses which allows dislocation shielding and a corresponding increase in the toughness [64,152,158,159]. For temperatures below 300°C, small 100 nm scale volumes under compression have shown K_{IC} values in the range of 1-10 MPa-m$^{1/2}$ [159] and 1 to 4 µm beams under bending [160] showed K_{IC} values range from 1-4 MPa-m$^{1/2}$. It is proposed that the amount of scatter in these measurements could be reduced by more refined experimentation.

For Nitronic 50, both free-standing and supported metallic thin films are utilized in a variety of applications including microelectromechanical devices [161,162] and interconnects [163]. These undergo multiple failure mechanisms such as delamination [164], channel cracking [165,166] and surface cracking which can be coupled by time-dependent damage from load cycling [167] and environmental degradation [168]. While multiple techniques and analyses exist for studying delamination or channel cracking of deposited thin films, direct measurements of fracture toughness values are relatively rare. Some fracture toughness measurements have been made for relatively brittle ceramics, graphene sheets or semiconductors as a function of length scale in the range of 10nm to 10µm [169-171], Recent efforts to study fracture toughness in more ductile materials have been undertaken, for example in NiAl [172] and Cu/CuSiAl multilayers [173].

For thin ductile films in general, greater fracture resistance and more stable crack advance with decreasing film thickness B would generally be expected as this has been the size effect trend in other materials ("Smaller is tougher" [159]). However, fracture instabilities could result from the increase in yield strength and a possible decrease in plastic energy dissipation as thickness, B, is reduced. The work per unit fracture area in

thin materials is proportional to the volume of the plastic region ($\alpha B^2 a$) divided by the crack extension area (Ba), where a is crack length and α is a constant relating the plastic zone size to a. This has been extensively studied both experimentally [174,175] and theoretically [173,177], as recently reported by Hosokawa *et al*. [178]. At nano-scale thicknesses, relatively small applied stress intensities for crack initiation and growth have been found for Au (0.45 MPa-m$^{1/2}$) and Al (0.515 MPa-m$^{1/2}$) [179]. These stress intensity values may reflect a plastic tearing process rather than true fracture instability, therefore characterization of the cracking process is needed to properly assess failure.

The predominant existing techniques for studying fracture at the nano/micro scale include nanoindentation, bulge testing, *in-situ* straining holders and MEMS devices. Traditional thin film nanoindentation techniques are powerful for studying supported films but cannot be applied to free-standing films [180]. For free-standing films, thin film bulge testing [179], MEMS devices[181], and *in-situ* straining holders for both TEM and SEM [178,182] can be applied, but only straining holders allow characterization of the cracking process. Though straining holders give high stability for imaging, they are severely limited in the extraction of mechanical data, as the load or stress is mostly unknown. A possible solution is to use *in-situ* nanoindenters which can provide both mechanical data and imaging [183], but a specialized testing geometry is needed to apply them to studying fracture properties. To this end, a novel doubly clamped *in-situ* three-point bend test, as recently introduced by Jaya *et al*. [184-186], was utilized to explore fracture processes at the micro and nanoscale. Samples were prepared for both *in-situ* SEM and TEM using FIB milling to explore the range of applicability of this technique and the evaluation of possible size effects.

The initial experiments were performed on the Nitronic 50 specimens, from which several issues were identified. Technique refinements based on these issues were applied to the silicon fracture specimens. This sequence is preserved in this chapter, such that the structure is a progression in both experimental methods and analysis techniques, which is fitting for development of novel experimentation.

4.2: Experimental Procedure for Nitronic 50 Bending Beams

4.2.1: Sample Preparation

All specimens were taken from a 20% cold-rolled bar of Nitronic 50, a purely austenitic (FCC) stainless steel. Nitronic 50 is an alloyed designed for high corrosion resistance and fracture toughness while maintaining reasonable strength. The "Nitronic" comes from the 0.50% N in the material, which added to increase the strength via interstitials to produce dislocation drag. The chemical requirements for Nitronic 50 are shown in Table 1.

Table 1: Chemical Composition of Nitronic 50

Chemical Requirements							
	Ni	Cr	Mo	Mn	C	Si	Fe
Max	13.5	23.5	3.00	6.0	0.06	1.00	Bal
Min	11.5	20.5	1.50	4.0			

The number average grain size for this material was found to be ~10μm by EBSD as shown in Figure 2.13. Lamellae of approximately 10μm thickness were prepared using a combination of electrical discharge machining, mechanical polishing, and electro-polishing as described in [187]. A special holder was used to fix the lamella which was

compatible with SEM, FIB and TEM. A multi-step FIB processes was used to produce bending beams of different sizes with a constant 4:2:1 (Length:width:thickness) aspect ratio with thicknesses of 2500nm (for SEM), 500nm (for SEM) and 100nm (for TEM). These dimensions were chosen to match the ASTM E 399 standard for three-point bending [188,189]. Beyond this point, some differences in the approach were necessary for the specimens designed for *in*-situ TEM. Accurate thickness measurements were performed for the 2500nm and 500nm thickness specimens by tilting the lamella 90° to an upright position in the SEM, but for the 100nm thickness specimens this method was found insufficient due to resolution limits of the SEM. Instead, the zero-loss peak was compared to the plasmon peak from electron energy loss spectrums as commonly done for thickness mapping, estimating an average atomic number of 26 [79].

FIB milling of a prepared lamellae, as shown in Figure 4.1a, to a final bend test specimen, Figure 4.1b, was accomplished using a Zeiss LEO1540XB operating at 30keV by multiple steps shown schematically in Figure 4.2. First, the rounded electropolished edge was cut flat using a large beam current of 10 nA from the side, shown as Cut 1. The sample was then turned and reinserted into the FIB and milled on both sides to produce lamellae of thickness appropriate for the size of samples being fabricated, typically 3x thicker than the final bending beam geometry, utilizing 10nA current, shown indicated by Cut 2. At this point, the beam current was reduced to 0.5nA to create the basic shape of the bending beams by removing material above and below the beam, see Cut 3. Next, careful reduction in size to the final dimension, smoothing the sides and removing FIB tapering was achieved by multiple cuts at 50pA. This required reinsertion into the instrument to cut from both the top and from the sides and was accomplished by using a

beam current of 50pA and tilting by 2° into the side walls of the bending beam to reduce

FIB taper from redeposition.
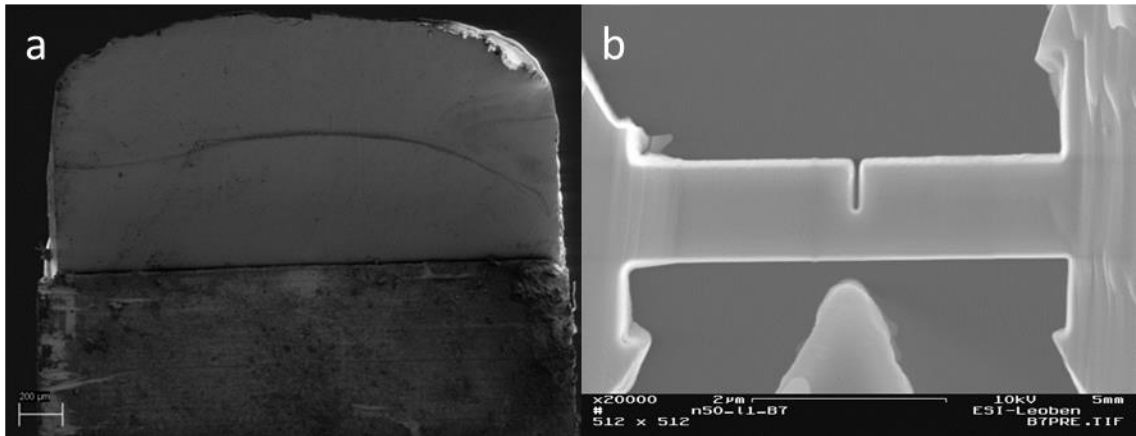
Figure 4.1: a) SEM micrograph of a Nitronic 50 lamella after electro polishing b) SEM micrograph of a completed 500nm thick bending beam sample
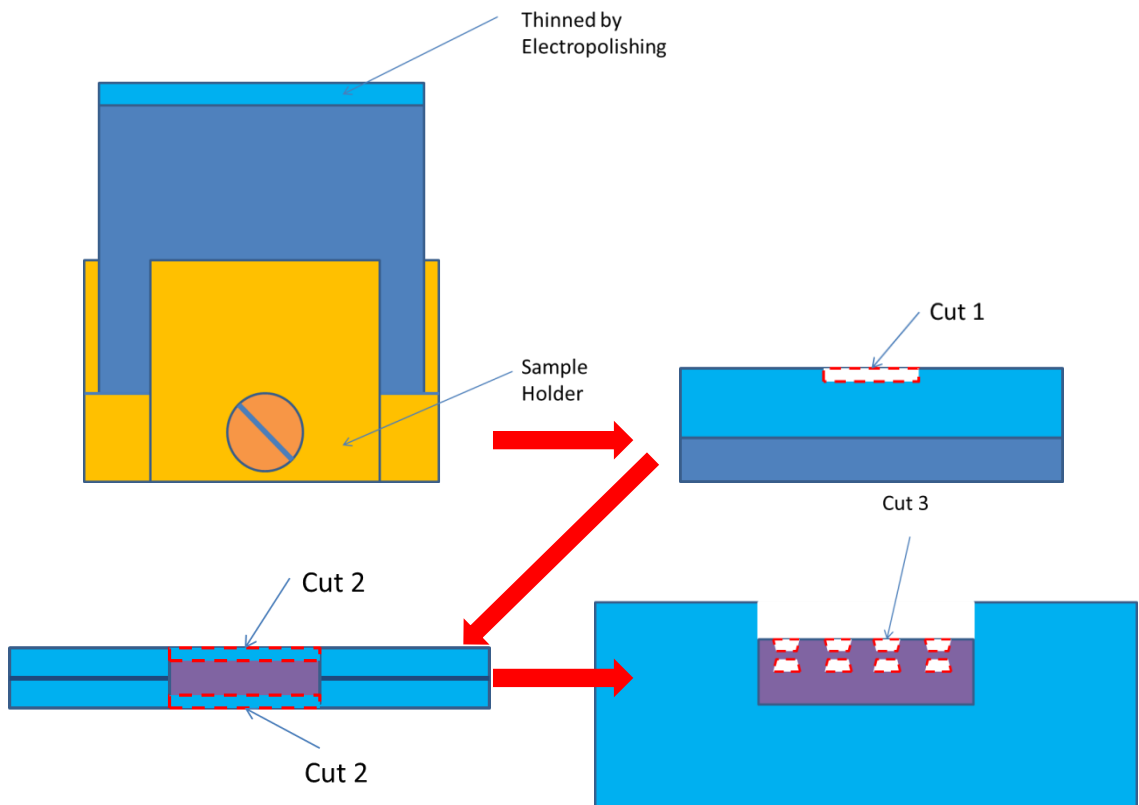
Figure 4.2: Schematic showing the multistep process to fabricate testing specimens by FIB indicated as Cuts 1-3

4.2.2: Pre-notching

All specimens also possessed a pre-notch traversing half the length of the bending beam, which is the most critical part of the sample preparation. The minimum available FIB current of 10pA is capable of producing a notch approximately 200nm in width due to resolution limits for a typical FIB. Consequently, for a 100nm thick beam with an 800nm span, the notch as fabricated by the FIB would have been about one fourth of the length of the beam, as also observed by Kumar *et al*. [190,191]. To improve this, a much sharper notch was produced by a novel method utilizing the fully converged TEM beam to locally sputter material, resulting in a notch radius of approximately 5nm.

Do these notches realistically replicate a sharp crack? Focusing of the ion or electron beam used to produce these notches is imperfect and results in a radius of curvature at the root of the notch. One way of viewing the problem was developed by Drory *et al*. [192]:

$$K'_{IC} = \left(1 + \frac{\rho}{2x}\right) K_{IC} \tag{21}$$

where the effective stress intensity factor K_{IC}' is modified from the ideal K_{IC}. The ratio of the radius of curvature, ρ, to a somewhat ambiguous length scale factor, x, determines the magnitude of this effect. This was later refined by Pugno *et al*. [193] and applied by Armstrong *et al*. to *in-situ* fracture testing [194], by introducing an asymptotic correction:

$$K'_{Ic} = \sqrt{1 + \frac{\rho}{2d_0}} K_{Ic} \tag{22}$$

where d_0 is given by:

$$d_0 = \frac{2}{\pi} \frac{K_{Ic}^2}{\sigma_u^2} \tag{23}$$

where σ_u is the ultimate strength of the material. Considering the FIB notched 500nm and 2500nm bending beams, reasonable values to use are an ultimate strength of 1 GPa measured previously from pillars of Nitronic 50 of a similar size, 1.5µm width as shown in Figure 4.3, a rough average measured value for K_I of 10 MPa-m$^{1/2}$ (shown later), and a radius of curvature of 100nm, one gets a correction factor of .079%. Clearly this correction is of minor concern.
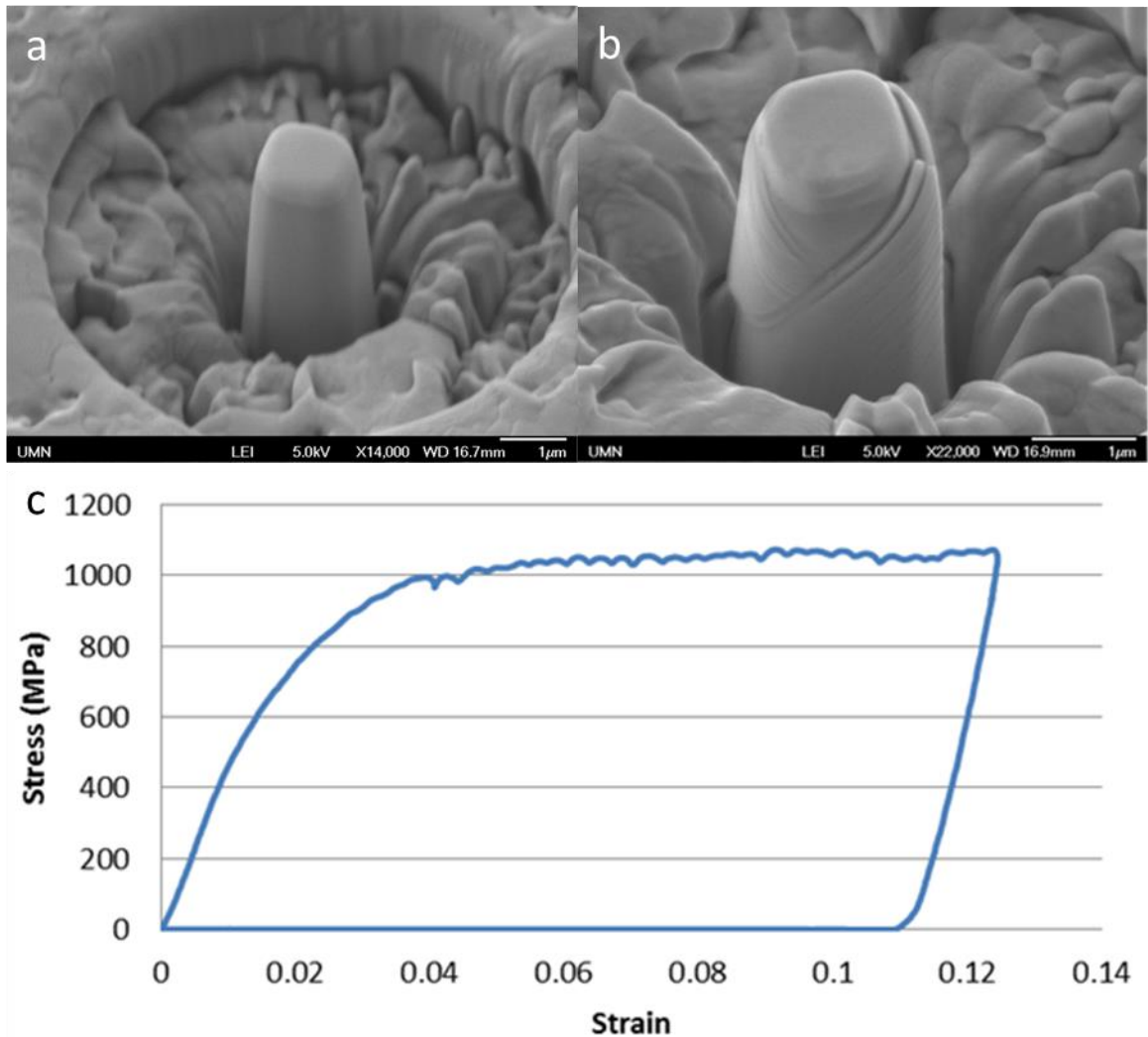
Figure 4.3: a) SEM micrograph of Nitronic 50 micropillar with width 1.5µm pre-compression b) SEM micrograph of the Nitronic 50 pillar post-compression c) Corresponding stress-strain curve

4.2.3: Characterization and Testing

An example of a 100nm thick bending beam being tested in the TEM is shown in Figure 4.4, where the thickness B is into the page, a_0 is the prenotch length, L the span, and b is the ligament such that the total bending beam width $W = b+a$. It is duly noted that FIB preparation results in residual damage from Ga implantation and is a concern here. However, rapidly varying contrast, typical for local lattice damage, was not significant compared to other materials FIB prepared for *in-situ* mechanical testing as in [77].
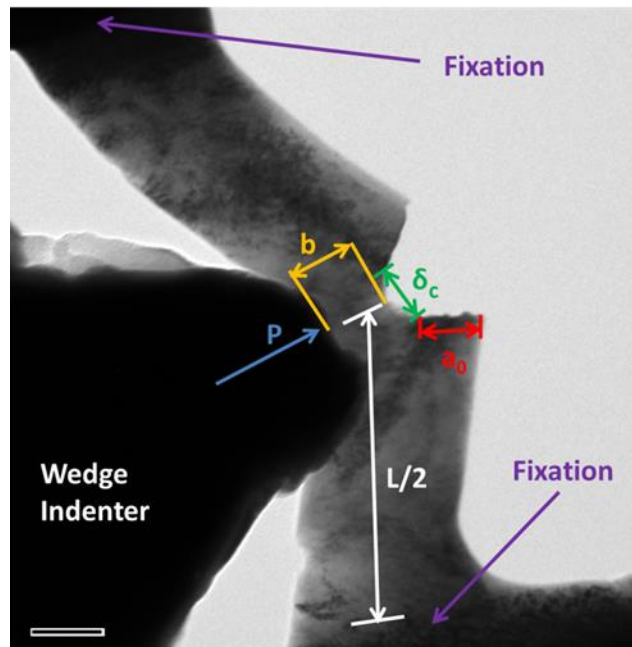
Figure 4.4: Experimental setup during in-situ TEM loading, with important features and measurable quantities labeled where P is the applied load, L/2 is half the span, b is the ligament, a_0 is the initial crack length, and δ_c the crack tip opening displacement. Scale bar is 100nm.

The FIB-fabricated 3-point bending beams were tested with two separate *in-situ* testing instruments, dedicated for use in the SEM and in the TEM, respectively. The *in-situ* SEM instrument utilized was an Asmec system inside of a Zeiss Leo 982 SEM as

shown in Figure 4.5a,b. Imaging was performed using 10 keV accelerating voltage in the secondary electron mode. For the TEM experiments, a Hysitron PI-95 Picoindenter holder was utilized *in-situ* in an image aberration-corrected JEOL 2100F operating at 200keV. For both instruments, testing was performed utilizing a wedge geometry tip (purchased from Synton-MDP, Nidau, CH) in displacement controlled mode, and strain rates were varied systematically from 0.0005 to 0.1 s^{-1}. Here, strain is defined as the maximum bending strain, $6\delta b/_{L^2}$, where δ is the indenter axis displacement. The strain rate variation was performed to account for possible strain-rate sensitivity [195] but had no apparent effect on the present results and will therefore not be discussed further. The wedge tip had a radius of curvature of ~200nm for the SEM indenter system and ~100nm for the TEM indenter system, respectively. The specimens were deformed using multiple (usually 4-6) loading cycles, which were typically about .05 to 0.1 bending strain in magnitude. Differences in approach distances and drift in the indenter system occurred which were corrected by measuring the true indenter motion in the acquired video.
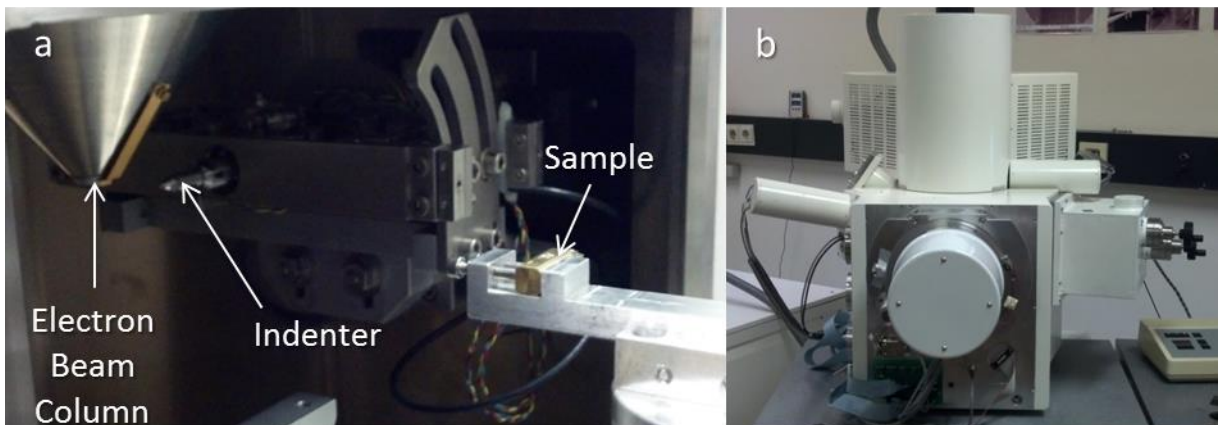
Figure 4.5: a) The Asmec indenter system b) The Zeiss Leo 982 SEM the Asmec is housed inside.

To explore characterization methods beyond imaging when utilizing electron microscopy, EBSD was utilized to track changes in grain size and crystal orientation with plastic deformation using a Zeiss LEO1525 operating at 30keV and a step size of 0.10 μm. It was found that only the 2500nm thick specimens provided enough usable signal for EBSD evaluation. Additionally, since deformation and EBSD were performed in different instruments, some oxidation/contamination occurred, thereby reducing the quality of the EBSD data. Still, one high quality example of a 2500nm beam was obtained is shown in the results section. Orientation mapping techniques could also be extended into the TEM by using a scanning probe to gather diffraction data [196] for mapping local deformations during testing procedures.

4.3: Nitronic 50 Bending Beam Results

4.3.1: 2500nm beams

Figure 4.6 presents EBSD scans of a representative 2500nm beam which underwent 5 load cycles, with cycle number increasing from top to bottom. Figure 4.6a shows grain orientations using the inverse pole figure (IPF) data, and Figure 4.6c depicts the local misorientation relative to the grain average. The load-displacement data for this 2500nm beam tested *in-situ* in the SEM are presented in Figure 4.6b with individual frames from the corresponding video at maximum deflection. As can be seen in Figure 4.6a, the plastic deformation in the later stages of testing gives grain rotation in conjunction with the transition from elastic to plastic deformation in the load-displacement data. Large rotational changes appear to occur along the grain boundaries

and are concentrated in the ligament region. For example, the tensile side just left of the notch begins with an orientation between the (001) and (111) axes and during loading rotates to an orientation between the (001) and (101) axis. A nearly perfectly opposite orientation change occurs just to the right of the notch on the compressive side, consistent with dislocation plasticity. There is a growing region of signal loss on the compressive side of the beam, which corresponds to a residual indenter impression. Additionally, the local misorientation shown in Figure 4.6c exhibits significant changes. For example, the grain directly underneath the notch exhibits first a relaxation in local misorientation when the loading is predominantly elastic (Figure 4.6c i-iii), while upon significant plastic deformation a strong misorientation localization is emerging right at the crack tip (Figure 4.6c iv-v). Thus, the most significant changes in the EBSD data occur corresponding to the transition to fully plastic behavior in the load-displacement data, which is indicated by a flattening of the load versus displacement data. In the video frames presented in Figure 4.6b, the transition to plastic behavior is accompanied by a permanent retained opening of the crack. It should be noted when comparing Figure 4.6b to Figure 4.6a&c that the EBSD data is taken when the specimen is fully unloaded, so that reverse plasticity could occur during unloading. As a note, cycle iv in Figure 4.6 deviates from the rest of the tests due to slight indenter misalignment.
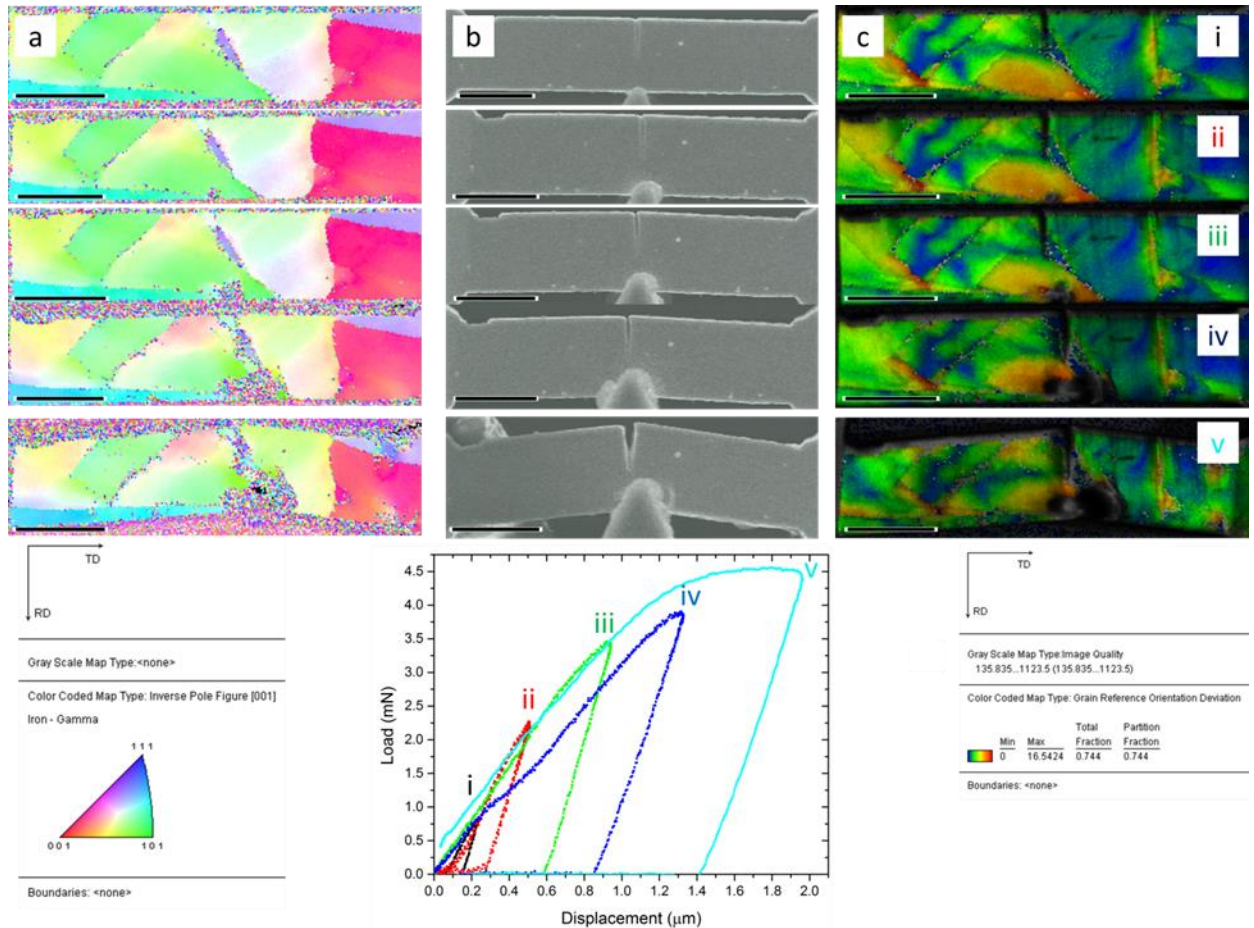
Figure 4.6: An exemplary 2500nm notched beam during stepwise loading a) Inverse pole figure map and corresponding color code b) In-situ SEM frames at maximum cycle load and recorded load displacement data c) Local misorientation map relative to the grain average. The scale bar is 5 μm long. i-v indicates the test cycle number. Note that the in-situ SEM frames are at peak load, while the EBSD data are after unloading.

4.3.2: 500nm beams

As previously stated, EBSD data could not be collected from individual beams as was possible with the 2500nm beams. Instead, an EBSD scan of the entire lamellae the beams were fabricated on is presented in Figure 4.7, with markings to show the spacing of the beams as a visual aid. The horizontal line shows the approximate line of the neutral axis for the fabricated beams.

95
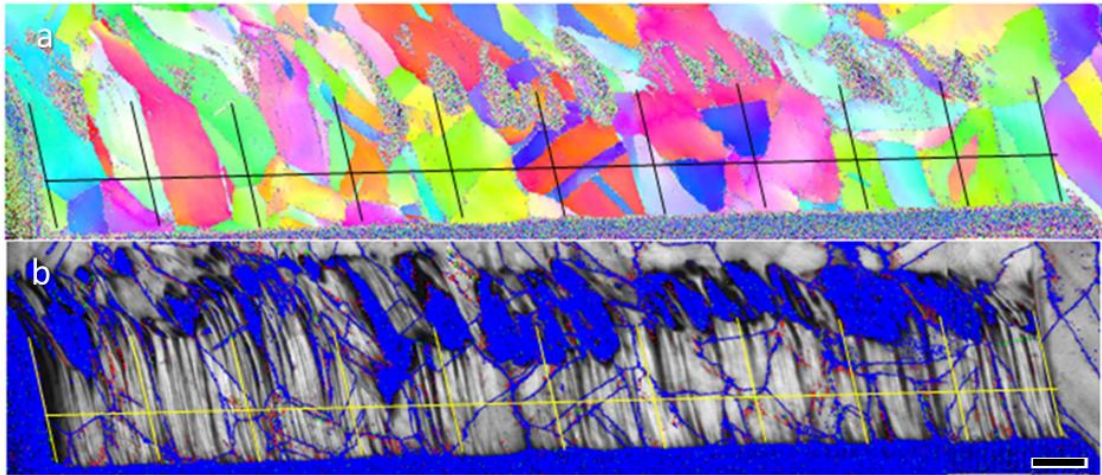
Figure 4.7: a) IPF Map and b) IQ Map with boundaries for the entire lamellae which the 500nm beams were fabricated on. Lines show the approximate locations of the beams made, scale bar 5um.

Figure 4.8 shows the load-displacement data for a representative 500nm beam, with selected frames from the corresponding SEM video. The same highly ductile behavior is observed as in the 2500nm beam, though the applied strains are much larger. The elastic region turns over to plastic as the plastic zones from the indenter tip and the crack tip overlap, creating a fully plastic hinge in the center of the beam which can support no further increase in load. As plastic deformation proceeds, the crack tip continues to open, such that a critical crack condition is not achieved. However, the crack advances slightly through what appears to be a ductile tearing mode (Figure 4.8 iii-v). The indenter was also observed to leave a residual impression for specimens of this size.
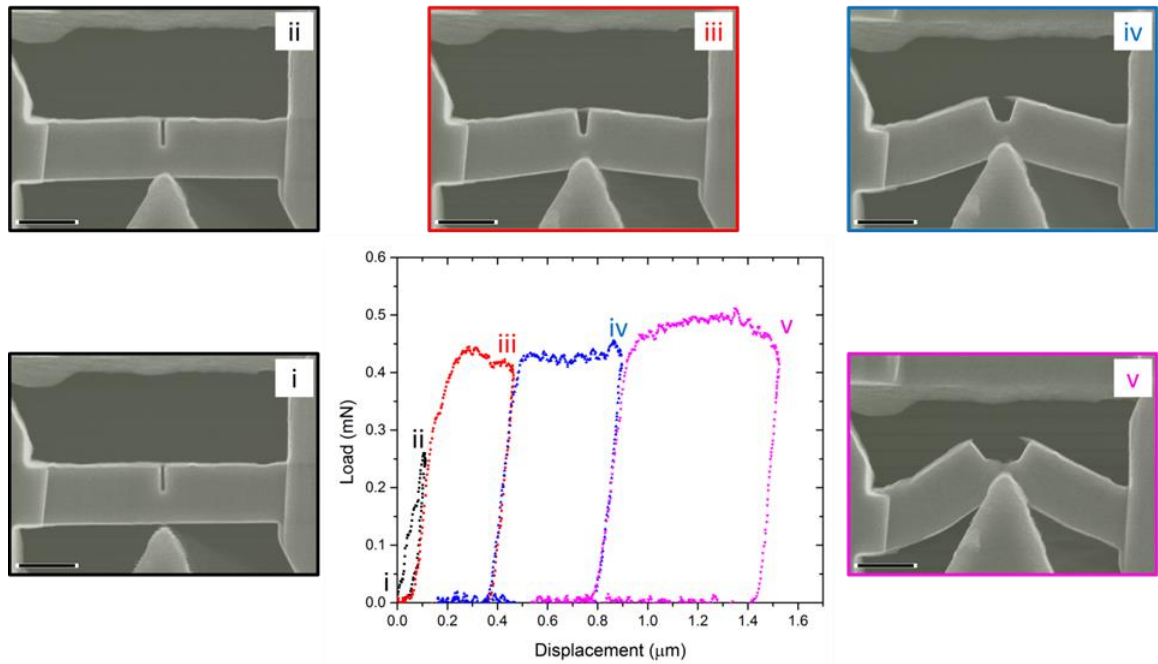
Figure 4.8: In-Situ SEM images and corresponding Load-displacement data for a 500nm beam with indication for the location of SEM video frames i-v. Scale bar is 1 μm.

4.3.3: 100nm beams

Figure 4.9 shows the load-displacement data for an exemplary 100nm beam, with selected frames from the corresponding *in-situ* TEM video. Qualitatively, deformation appears to proceed similar to the larger specimen sizes. All 100nm beams tested were single crystalline. The predominant contrast feature observed as deformation occurs is related to strain or bending contours in and out of the viewing plane. In addition to the bend contours, there is a dark region that develops directly underneath the indenter tip, which is retained upon unloading shown in Figure 4.9 iie and iiie. This could be related to a higher dislocation density, such that this dark region corresponds to the plastic zone in front of the crack tip. The load-displacement data shows expected highly ductile behavior, but in the plastic regime, the load slightly decreases in a steady manner with

97

each testing cycle. This may be attributable to the formation of secondary cracks on the compressive side of the bending beam near the clamped ends where a stress concentration from the clamping constraint exists. The sudden rise in load after cycle vi is likely caused by the indenter running out of clearance and making additional side contact, but it was not obvious from the acquired video exactly where this occurred. It should be noted that the sharpness of the indenter tip relative to the size of the bending beam is greatly reduced for these specimens, resulting in a reduced indentation from the indenter into the specimen.
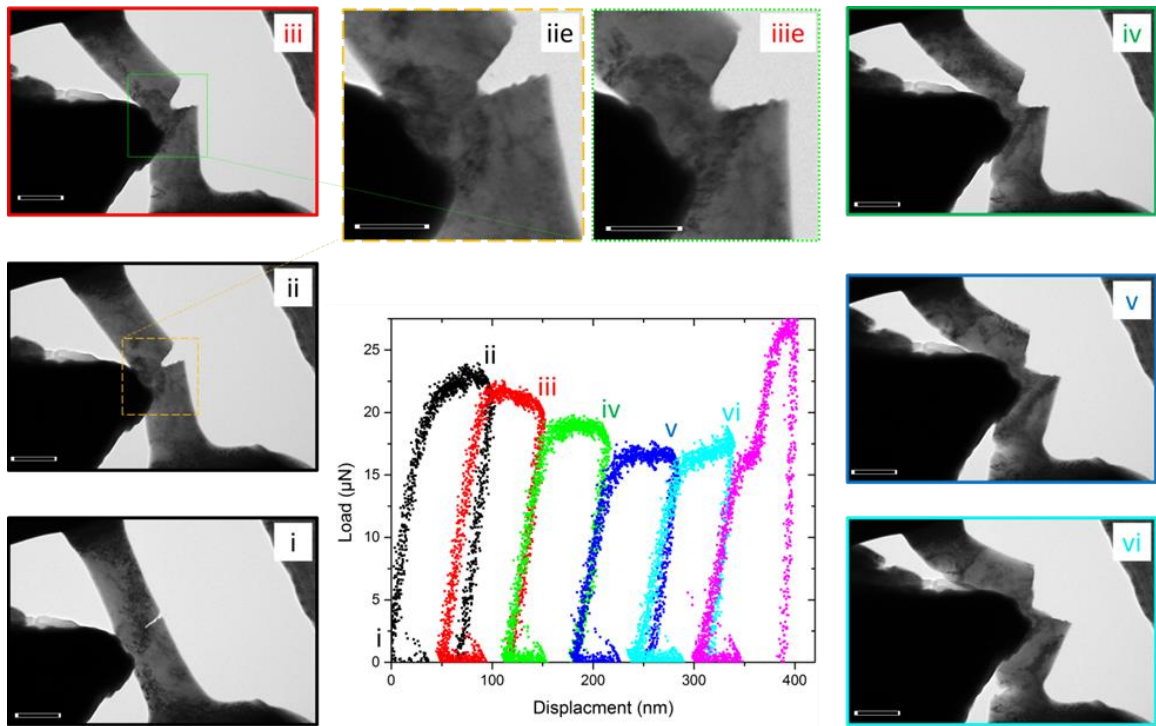
Figure 4.9: Load-displacement data for a 100nm beam with indicated positions of frames i-vi from the in-situ TEM video. Two enhanced magnification images (noted by a hatched box and an e) show evidence of a plastic zone directly under the notch root. Scale bar is 200nm in all images.

4.4: Analysis Procedures for Nitronic 50 Bending Beams

4.4.1: Discussion of Complications

There are a number of currently unaddressed issues with this experimental design. First, these deeply cracked bend beams experience a rapidly increasing K_I as the crack approaches the back free surface. Second, the support of the nanoindenter on the compressive side, while giving good stability to the system as previously discussed by Jaya *et al*. [184-186], does represent a contact stress gradient. This introduces added complexity to the stress analysis as the plastic zone from the indentation will interact with the plastic zone at the root of the notch, as described by Chen and Bull [197]. An indentation stress calculation demonstrated a substantially smaller stress from a plasticity standpoint. Using the contact cross-section to estimate the contact flow stress based upon load and imaged contact area, this was determined to be about half of the bending stress. Notably, the situation improves for smaller beams, where the reduced bending loads limit the penetration depth (Figure 4.9). Additionally, clamping of the beam is a necessary feature, but this results in mechanical work being dissipated into the clamped region that is not correctly accounted for in the applied *J*-integral method. Furthermore, the end constraints apply an additional moment that acts to close the crack front as the ends are not free to rotate. Given these challenges, it is clear that Finite Element (FE) or other advanced computational methods are needed to accurately determine applied stress intensity values.

Secondly, the LEFM or *J*-integral approach may not be the best descriptor for these very small beams. Earlier studies [198] raised questions about whether or not

LEFM or LEFM-based J-integral analysis was always correct. Atluri, *et al* [199] showed that a T* criteria may be more appropriate for the complete unloading and reloading format of Figure 4.7-4.9. Their concern was that the path-independent integral, *J*, could be quite different if the plastic zone was elongated to include plasticity in the crack wake rather than just the plasticity at the front of the crack. In one of the 100nm beams there was an indication of dislocations in the crack wake, shown in Figure 4.9 iiie, where a dark contrast feature is seen along the notch flank. As this is a bright field image, this is still an open question and not a certain proof. However, it is clear in Figure 4.9 that substantial dislocation plasticity was generated during the crack growth process. These observations for the first two load and re-load curves shown in Figure 4.9 represent K_I values according to Eq. (26) of 3.2 and 4.2 MPa-m$^{1/2}$. Using a first-order estimate of the plastic zone diameter of $\pi(K_I/\sigma_{ys})^2$, one evaluates plastic zone sizes at least a factor of four larger than those observed in Figure 4.9. It is apparent that additional numerical approaches are required to address plasticity-based slow crack growth in such small-scale bend beams. Lastly, the *J*-integral approach utilized here from Eq. (26) is standard; a possible refinement would consider the local plastic deformation at the root of the crack and the corresponding local yield stress specifically [200].

These issues could largely be resolved by utilizing two important revisions. First, a flat tip simulating a four point bending test would simplify the stress field from the indenter and reduce indentation of the tip into the specimen. Secondly, finite element analysis would be able to analyze the complex stress state, especially with a stress-strain law determined by supporting pillar compression experiments, such as the analysis method proposed by Shih [201].

4.4.2: K_I Analysis Methods

Despite these issues, analysis efforts were carried out. In order to determine applied stress intensities, a linear elastic fracture mechanics method (LEFM) for 3-point bending is applied. An LEFM method by Bakker [202] allows larger a/W ratios up to 0.95 as compared to the ASTM E 399 standard for 3-point bending. From the tabulation of $f_k(\alpha)$ for various values of $\alpha = a/W$ and crack lengths the stress intensity can be determined from:

$$K_I = \sigma_b \left[\frac{f_k(\alpha)}{(1-\alpha)^{3/2}} \right] \sqrt{\pi a} \qquad (24)$$

where σ_b is $(3PL)/(2BW^2)$, where P is the load, L is the span, B is the thickness and W is the width and $f_k(\alpha)$ is:

$$f_k(\alpha) = \frac{1.0731 - \alpha(1-\alpha)(1.1980 - 5.1240\alpha + 7.3327\alpha^{\frac{3}{2}} - 3.1403\alpha^2}{1 + 1.8706\alpha}. \qquad (25)$$

A *J*-integral approach to account for plasticity occurring during the fracture process was also utilized. The result for deep cracks was again given by Bakker [202]:

$$J_I = \left[\frac{(1+\alpha_0)}{(1+\alpha_0^2)} \right] \frac{2A_{total}}{Bb} \qquad (26)$$

where b is the remaining ligament in front of the crack, A_{total} is the total area under the load-displacement curve, B is the beam thickness and α_0 is given by:

$$\alpha_0 = 2\sqrt{\left[\left(\frac{a}{b}\right)^2 + \left(\frac{a}{b}\right) + \frac{1}{2} \right]} - 2\left(\frac{a}{b} + \frac{1}{2}\right). \qquad (27)$$

4.4.3: Analysis Results

Using the theoretical procedures described in Eq. (24-27), the K_I and K_{IJ} values were determined for all tested 100nm and 500nm beams, as plotted versus crack length a in Figure 4.10. It was determined that the 2500nm beams possessed too much indenter punch in and are not presented here. It is observed that the values of K_{IJ} are significantly higher than K_I as expected due to the ductile nature of the material being studied. It should be emphasized that all these values represent a lower bound estimate of K_{IC}, as the crack does not achieve an unstable opening displacement and thus is not in the critical state.
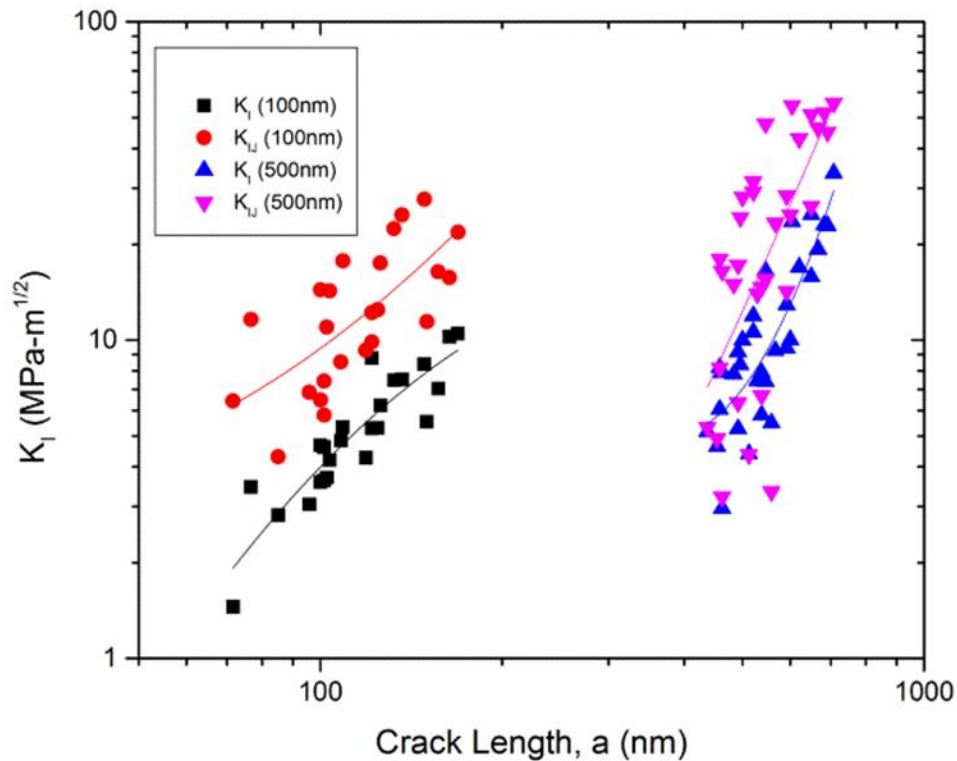
Figure 4.10: Stress intensity factor vs. crack length a for 100nm and 500nm beams, with both K_I calculated by Eq. (24) and K_{IJ} calculated by Eq. (26), respectively.

Evans and Suo [203] demonstrated and verified that the strain energy release rate for channel cracking was proportional to the film thickness, such that $G_I \sim \sigma_{ys}^2 h/E$. In our case, the resistance does appear to shift to higher values with increasing thickness in Figure 4.10. As can be seen from Eq. (24), the only difference in K_I emerges from the term $a^{1/2}$ if a/W is kept constant. In LEFM then, one might expect K_I to be about $5^{1/2}$ larger for the thicker 500nm beam which is consistent with our experimental observations. However, the steepness in dK_I vs. da is more pronounced for the thick beam than the thinner one. This is shown in detail Figure 4.11 where dK_I vs. da/W (a is normalized by W for comparison purposes) is approximately flat for the 100nm beam, but increasing with a rate of 0.11 MPa-m$^{1/2}$/nm for the 500nm beams. It is difficult to compare these measurements directly to other literature, given the novelty of the testing presented here, but these values seem reasonable for a plastic tearing process in a high toughness material. Paviot and Vlassak [179] found stress intensity values for thin film crack growth for Au (0.45 MPa-m$^{1/2}$) and Al (0.515 MPa-m$^{1/2}$), which is an order of magnitude less than what is measured here. The ratio of applied stress intensities for ductile tearing in these film films is approximately the same as the ratio between their bulk plane strain fracture toughness values.
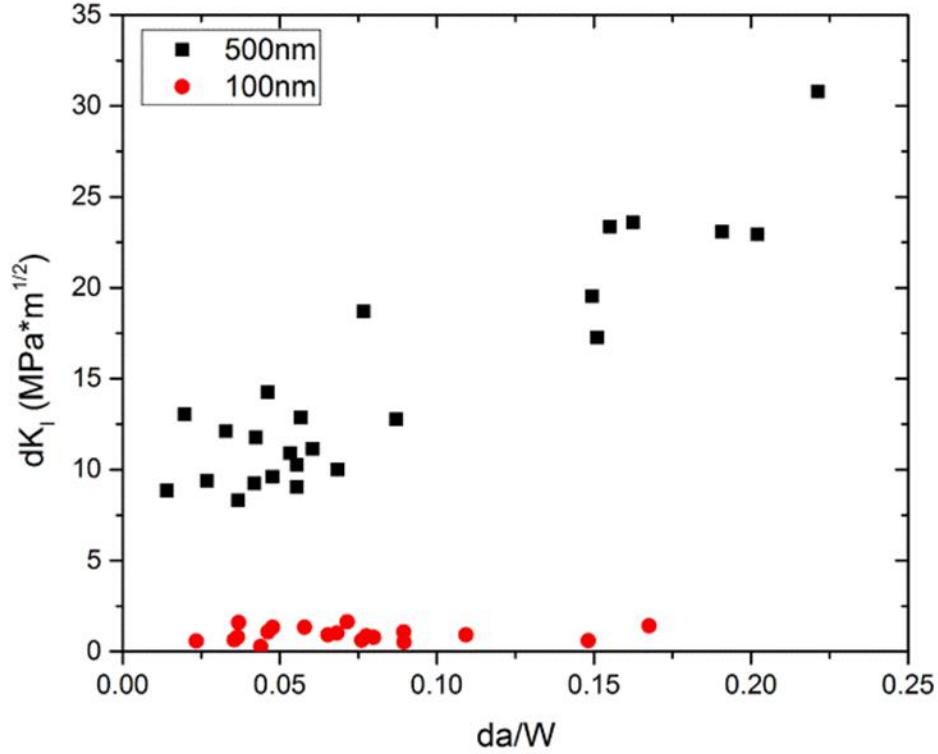
Figure 4.11: dK$_I$ vs. da/W for 100nm and 500nm beams; da is normalized by the beam width for comparison of the different sizes

4.4.4: Crack Tip Opening Displacements as a Verification Technique

In order to determine the viability of the analysis in equations (24-27), they were compared against applied stress intensity factors calculated by crack tip opening displacement [204], δ_c, which is given for plane stress as:

$$\delta_c = \frac{K_I^2}{\sigma_{ys}E} \tag{28}$$

where K_I is the opening mode applied stress intensity, σ_{ys} is the yield strength and E is the modulus of elasticity. Given that flow stress is enhanced with reduced dimensions, estimation of a reasonable yield stress to use in conjunction with Eq. (28) required extrapolation of previous data. The yield strength was extrapolated from FIBed nano-

pillar compression data for Nitronic 50, as shown in Figure 4.3, and from the austenitic phase of duplex steel [205]. The data are shown in Figure 4.12a for a range of pillar diameters ranging from 300nm to 10µm. The extrapolation to 100nm gave a flow stress of approximately 1900 MPa.
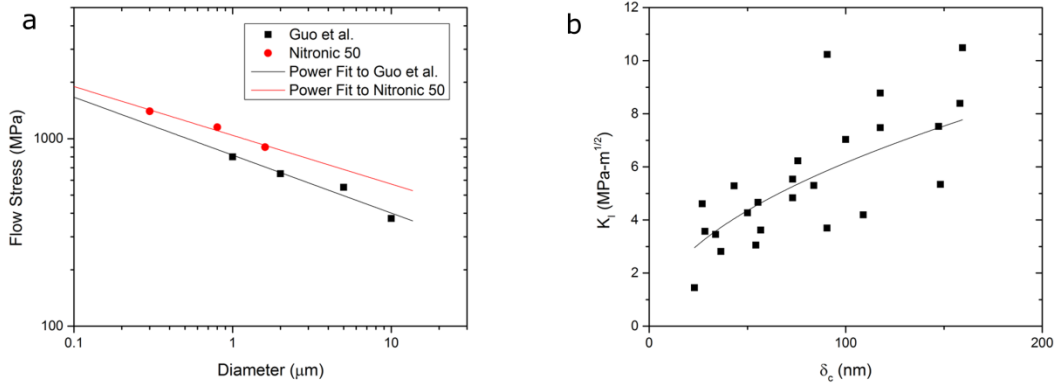
Figure 4.12: a) Flow stress vs. size from micropillar compression data on Nitronic 50 extrapolated to 100nm b) Stress intensity values derived from Eq. (26) versus the measured crack opening displacement (points) and the prediction from Eq. (28) (line) for 100nm beams.

Values of δ_c were measured directly from the video using the standard 90 degree intercept method. Values of K_I calculated by Eq. (26) were plotted against measured δ_c values as shown in Fig. 4.12b, with the extrapolated flow stress of 1900 MPa inserted into Eq. (28) to produce the overlaying fitting line. This shows that there is good agreement between analysis using Eq. (28) and Eq. (26) for beams of 100nm thickness. This analysis assumes no strain hardening, which appears reasonable as repeated loading exhibits little hardening as one would expect as the 100nm section thickness allows easy dislocation termination at surfaces.

4.5: Experimental Procedure for Silicon Bending Beams

4.5.1: Technique Refinements

Further studies were performed on silicon micro and nano bending specimens using a similar testing methodology. Here, the primary goal was to refine many of the issues discovered during testing of the Nitronic 50. Silicon serves as a model brittle material which undergoes critical failure by sudden crack jumps, unlike Nitronic 50, which undergoes steady crack advance via a ductile tearing mode. This makes identifying and evaluating critical values much easier, and limits the complications due to plastic deformation.

Two types of experiments were perfomed on pre-notched silicon beams: nanoscale *in-situ* TEM fracture experiments and elevated temperature microscale bending beams *in-situ* SEM. For both experiments the specimen geometry was improved. The effects of the clamping constraints were reduced by slightly increasing the length aspect ratio to 5:2:1 and the crack tip indenter interactions were reduced by decreasing the initial notch length to only traverse 1/3 of the specimen width. A slightly blunter tip relative to the bending beam size was also used to reduce complexity of the crack-indenter interactions and reduce indenter punch-in. Additionally, HF etching to remove FIB damage and FEM analysis to understand the complex stress fields was performed.

Single crystal Si wedge substrates as sold by Hysitron, which were lightly boron-doped and <110> oriented, were utilized for specimen preparation. Specimens were FIB-fabricated using a similar technique as the Nitronic 50 bending beams at 30keV using an FEI Quanta dualbeam FIB/SEM, with final shaping cuts performed at a 2° tilt into the specimen wall in order to reduce natural FIB tapering from redeposition.

For the nanoscale Si bending beams, three different specimen sizes were tested to see which would result in favorable final geometries after HF etching and explore any possible size effects. The three beam thicknesses tested were 100nm, 200nm and 300nm. Final specimen thickness was determined using the same CTEM EELS technique applied to the Nitronic 50 specimens, assuming a Z=14.0 [79]. Pre-notching was again performed using the converged electron beam technique as used on the Nitronic 50. Experiments were carried out using a Hysitron PI-95 PicoIndenter equipped with a specially FIBed wedge tip with a contact width of ~100nm at an applied displacement rate of 1nm/s. The utilized microscope was an FEI Tecnai F30 operating at 300keV.

For the microscale Si bending beams, specimens were fabricated to have a nominal 1µm thickness. Testing was performed using a Hysitron PI-87 PicoIndenter *in-situ* SEM using a FEI Versa dualbeam FIB/SEM and a specially FIBed wedge indenter tip. The wedge indenter had ~500nm radius of curvature. Indentation was performed in displacement control using a displacement rate of 2nm/s for all tests. Figure 4.13 shows an SEM micrograph of the FIBed wedge tip used for the microscale testing and the silicon wedge substrate with an as fabricated specimen on the left and a just tested specimen on the right.
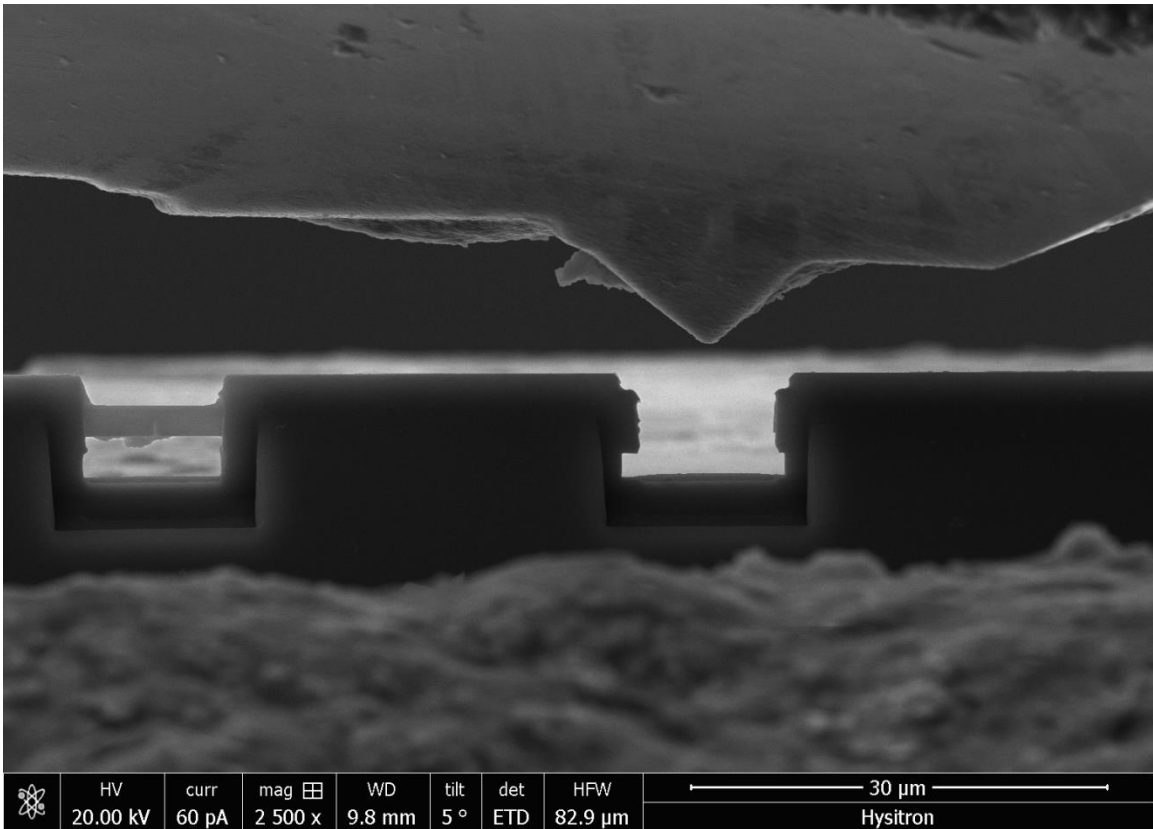
Figure 4.13: Silicon microbeam testing showing FIBed wedge tip and Si wedge substrate the specimens were fabricated into.

Temperature control was accomplished using a Hysitron prototype "stub" heater which mounted directly into a zirconia thermal isolation sleeve with the sample mechanically clamped to the heater. This sleeve was attached to a water cooled aluminum chilling block which mounted to the stage of the PI-87. Temperature was controlled using a feedback-equipped Lakeshore 372 temperature controller and monitored via thermocouples to control heater power. Temperature curves versus heater power were calibrated before testing. Additionally, all samples were annealed at 800°C for 30min before testing to limit variation due to impurity diffusion during testing, particularly implanted Ga from the FIB fabrication. This is expected to reduce the effects

of FIB damage similar to the method proposed by Kiener [77] but this was not yet quantified using chemical analysis.

Specimens were tested at room temperature, 150°C and 300°C, with future plans to extend to 450°C and 600°C. These higher temperature tests required a more thermally stable tip which was not yet available.

4.5.3: HF Etching to Remove FIB Damage

The removal of FIB damage was attempted by using an HF etching technique for the nanoscale bending beams. Here, 5% HF and 3% HCl in DI water was used as an etching agent, which the entire wedge substrate was submerged into while being held with polymer tweezers. The as FIB-fabricated bending beam is shown in Figure 4.14a with the specimen well aligned to the <110> zone axis. The FIB-damaged outer region is obvious due to the zone axis alignment and use of an objective aperture. After 2 separate HF treatments for 1min and 5min of etching time, the end result is shown in Figure 4.14b. Total removal from the front of the specimen and substantial reduction on the opposing side of the specimen of the damaged region can be observed. This unfortunately resulted in the buildup of contaminant from the etching process, which was not removable by a 30min plasma cleaning cycle. However, the tradeoff of the contamination versus FIB damage seems very favorable. A secondary drawback to the HF etching process was changes in final specimen geometry from what was targeted via FIB.
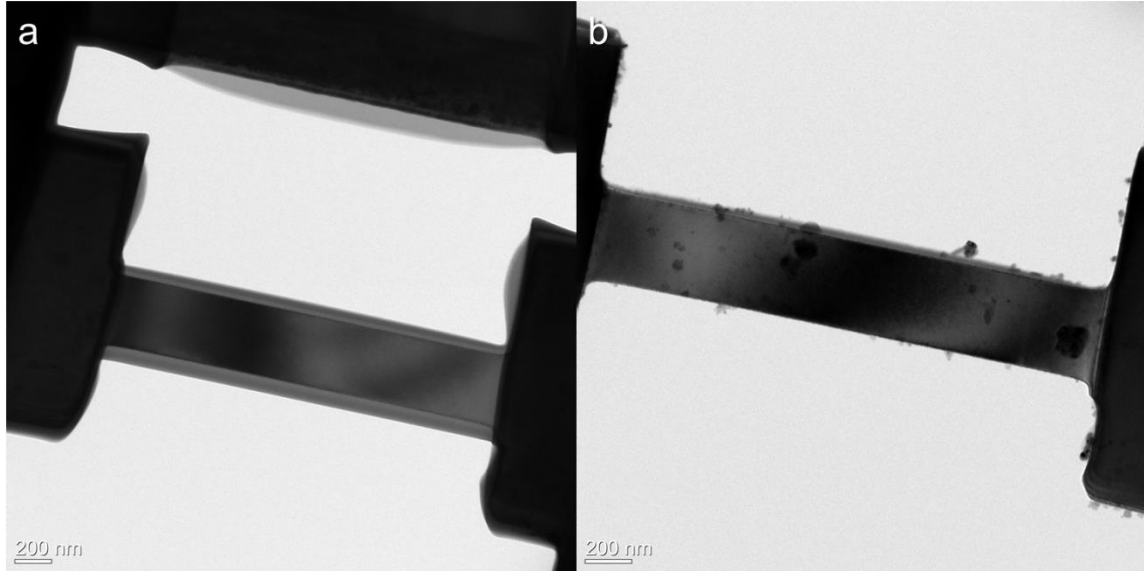
Figure 4.14: a) TEM micrograph of a 200nm thick silicon nanobeam before HF treatment taken along <110> zone axis in bright field conditions b) Bright field TEM micrograph of 200nm silicon beam after 6min of exposure to HF etching solution.

4.6: FEM Analysis

Initial FEM modeling efforts were employed to characterize the complicated stress state described in Section 4.4.1. The utilized mesh is shown in Figure 4.15a and the resulting K_{IC} per μN applied load vs. crack length for a 200nm thick bend specimen is shown in Figure 4.15b. The FEM model assumed isotropy and used values of $E = 160$ GPa and $v = 0.22$ [132]. It can be seen that following a brief plateau, the elastic stress concentration factor takes a bell-shape, initially rising to a maximum value around 150nm or 40% of the beam width, then falling drastically with increasing crack length. This behavior is due to the clamping constraint at the ends which prevents their rotation and produces a closing of the crack tip which was unaccounted for by the Bakker LEFM analysis. These findings are in agreement with the predictions of Jaya et al. [184,185], though the aspect ratios of the Si specimens presented here are different, which was shown to have effects on K_I in [185].

a
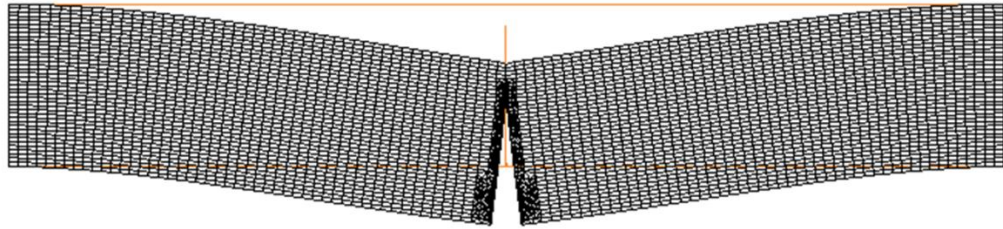
b
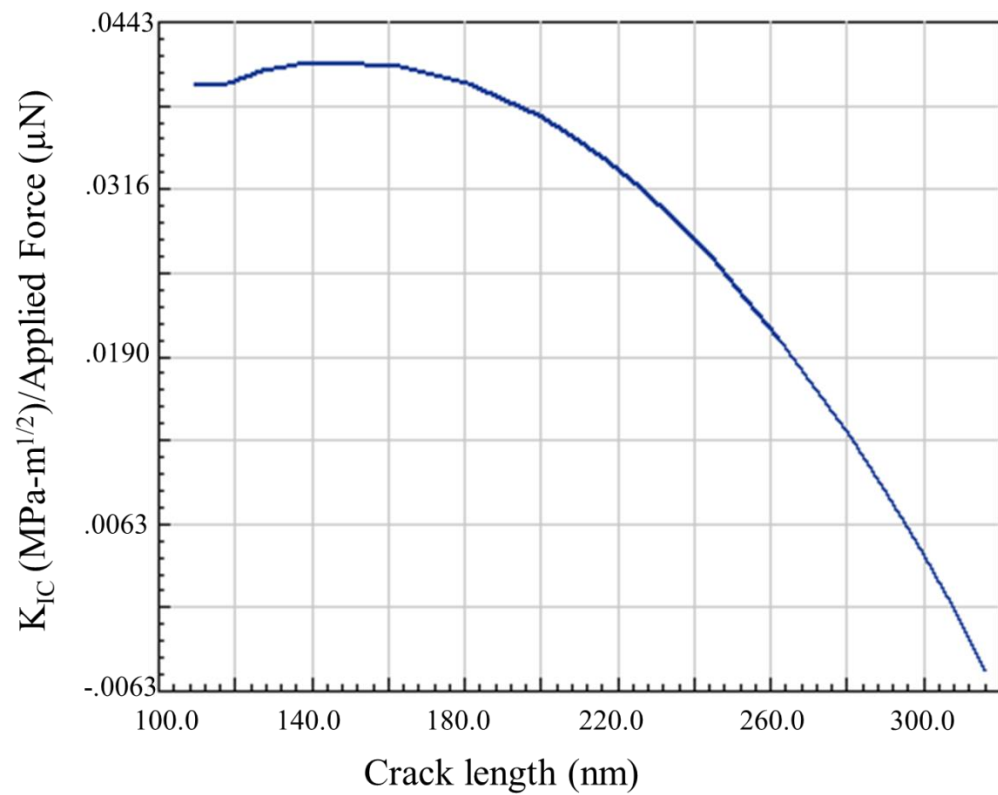
Figure 4.15: a) Mesh utilized for FEM modeling of a nominally 200nm thick Si bending beam b) resulting K_{IC} per applied force vs. the crack length.

This FEM solution was determined for the geometry of one specific nanoscale Si

bending beam of 200nm nominal thickness, as shown in Figure 4.16.
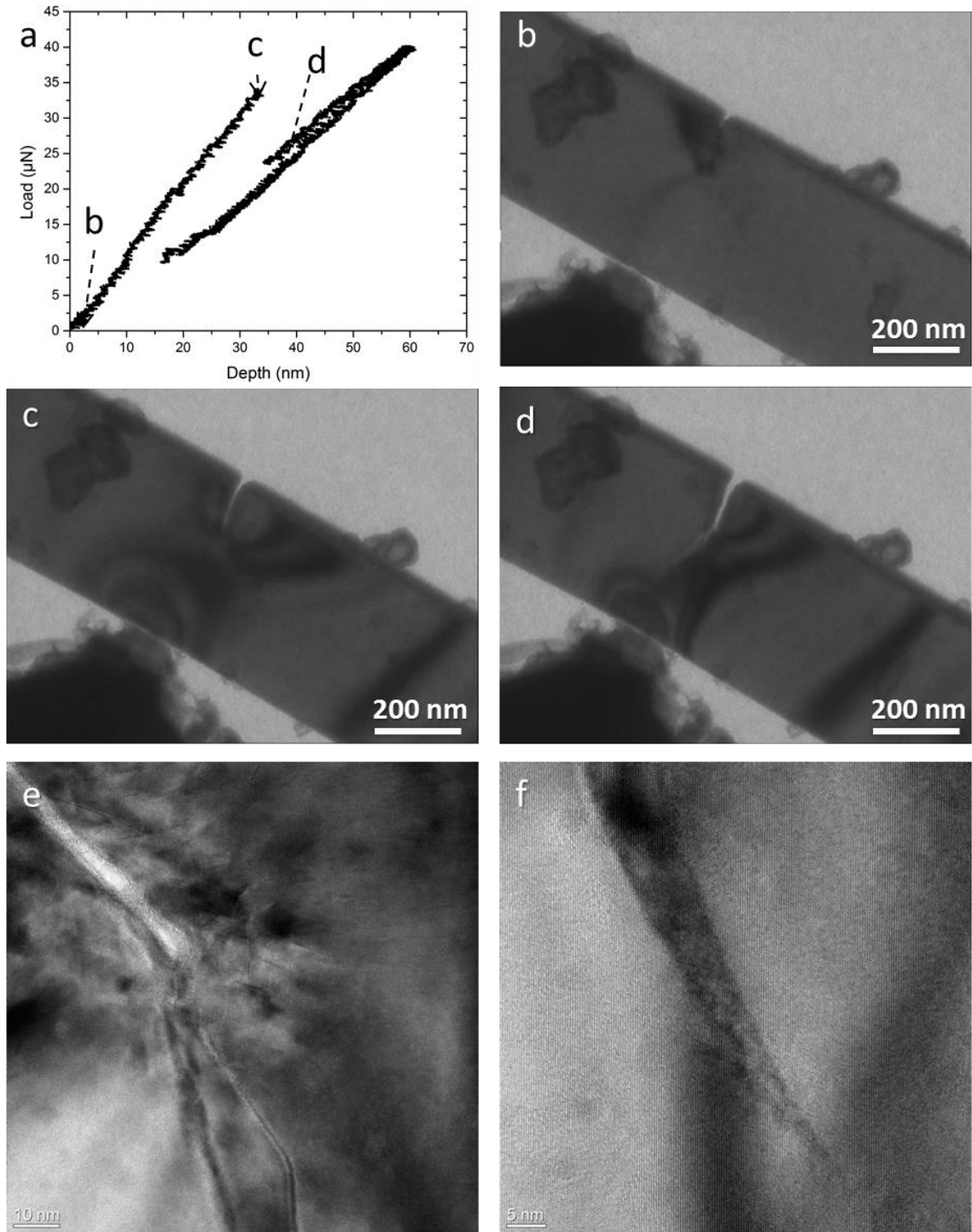
Figure 4.16: a) Load-displacement curve for a nominally 200nm thick Si bending beam (b-d) In-situ TEM video frames at a) unloaded pre-testing, b) just before fracture and c) just after fracture. (e,f) Post-mortem high resolution imaging of the e) base of the fabricated notch showing dislocations surrounding the notch f) end of the extended crack which is dislocation free.

The fracture toughness as determined by the FEM analysis was 1.33 MPa-m$^{1/2}$ at crack initiation as shown in Figure 4.16c. This is in good agreement with other micro/nano scale measurements of silicon fracture toughness [64,89]. The crack can be observed to propagate along a different path from the prenotch, likely following a cleavage plane as seen in 4.15d. The angle of the crack is ~35° offset from the pre-notch, which matches closely to the projection a {111} plane onto the bending beam surface. The {111} plane is the lowest energy cleavage plane in Si with an ideal Griffith fracture toughness of 0.627 MPa-m$^{1/2}$. The calculated stress intensity at the crack arrest point was 0.57 MPa-m$^{1/2}$, which compares reasonably well. The enhanced fracture toughness of the crack initiation from the notch could reasonably be attributed to two factors. First, the pre-notch possesses a radius of curvature, though small (~5nm) that reduces the applied stress intensity. The notch sharpness correction factor in Section 4.2.2 predicts an 18% correction factor for this effect, assuming a K_{IC} = 1.0 MPa-m$^{1/2}$ and σ_u = 10GPa. Secondly, it can be observed in the post-mortem imaging in Figure 4.16e that significant numbers of dislocations surround the notches which are not present at the end of the crack arrest as shown post-mortem in 4.15f. These dislocations would produce a back stress on the notch, resulting in a higher K_{IC} value.

4.7: Results for Silicon Bending Beams

4.7.1: Results for Silicon Nanoscale Bending Beams

An example of a nominally 100nm thick bending specimen is shown in Fig. 4.17. Here, irregular behavior was observed as the crack advanced through multiple small steps rather than one large jump. This crack also appears to be deflected along a {111} plane similar to the 200nm specimen shown. The front of the crack shows the expected strain contrast due to the stress concentration effect of the crack. Why the crack growth is steady here compared to the other tested specimens is not clear. One possible explanation could be the lack of dislocations surrounding the notch as shown by post-mortem high-resolution imaging in 4.19b. Futher experiments might yield more of this behavior and potentially allow it to be correlated to some aspect of the specimen geometry.
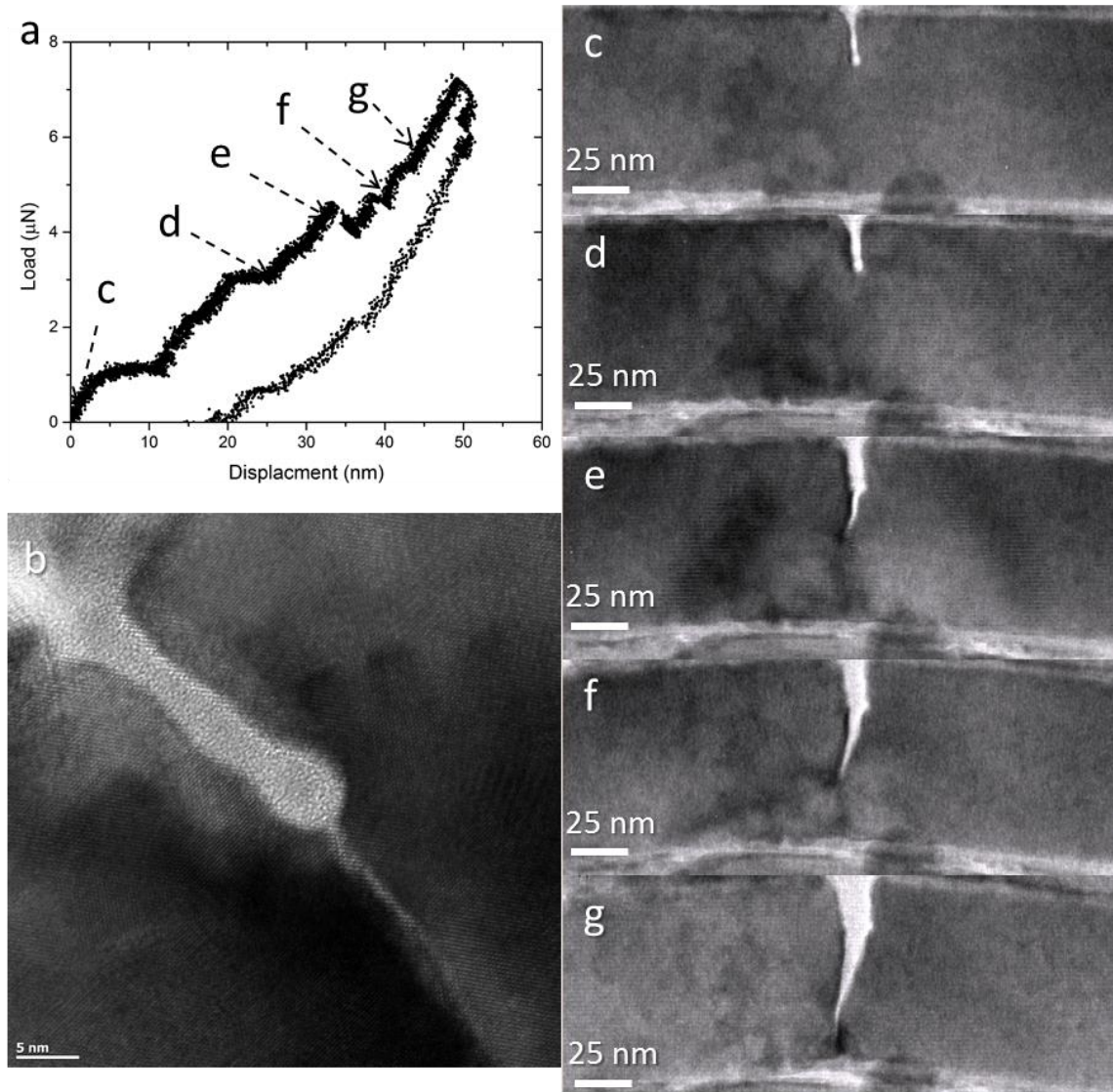
Figure 4.17: a) Load-displacement curve for a nominally 100nm thick beam Si bending beam with b) post-mortem high resolution TEM of the notch with the crack extending from it and (c-g) TEM image series taken from the corresponding *in-situ* video.

An example of a nominally 300nm thick specimen is shown in Figure 4.18. Here a large singular crack jump is observed, but this time with a straight trajectory in line with the loading direction. Several other nanoscale bending beams displayed undeflected cracking as well. What loading conditions or bending beam geometry govern the crack

trajectory is currently not known, though from an analytical standpoint, more refined

crack tip stress field calculations can predict this using a quantity known as the T stress.
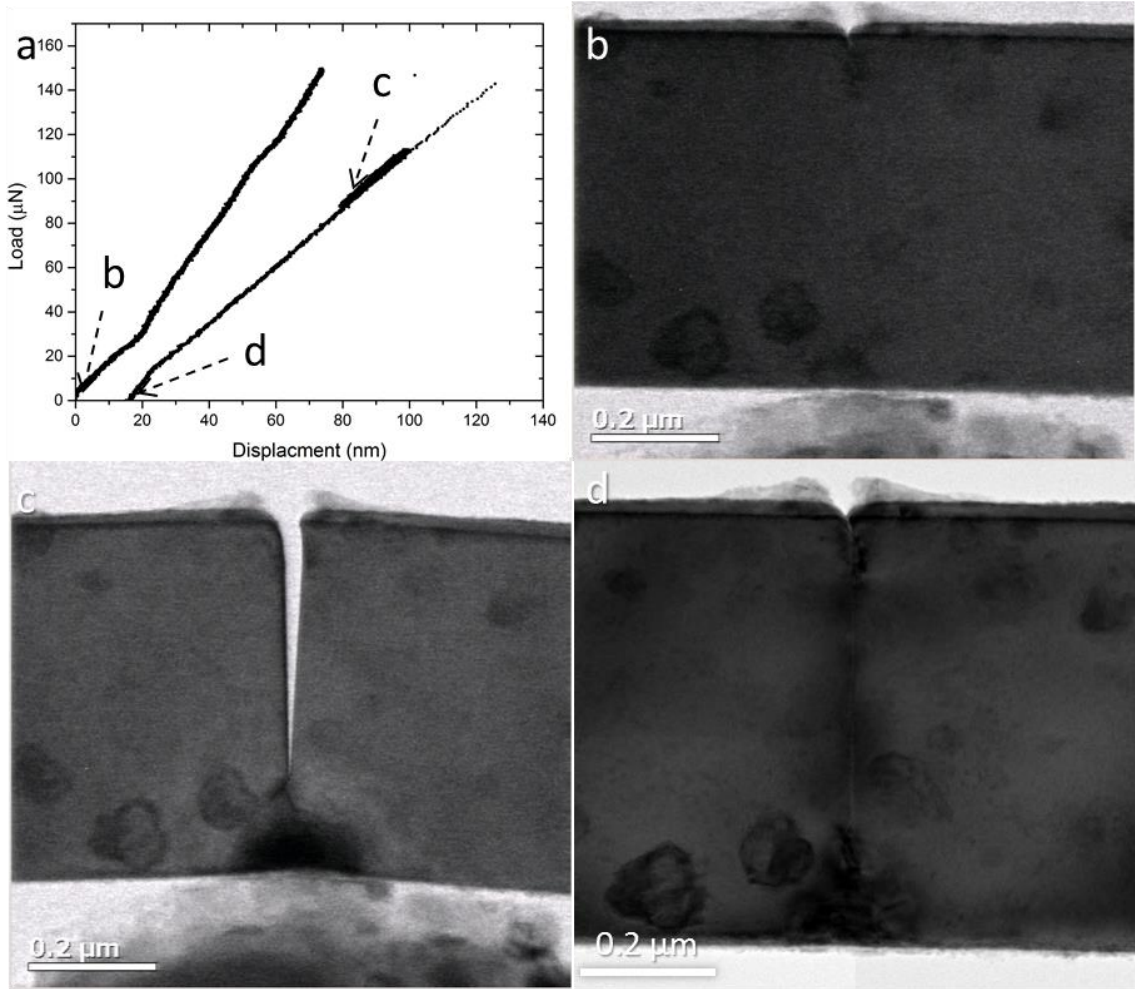
Figure 4.18: a) Load-displacement curve for a nominally 300nm thick beam Si bending beam with TEM image series taken from the corresponding *in-situ* video where b) is in the unloaded state c) is directly after crack initiation and d) is fully unloaded.

The load-displacement data for 18 separate nanoscale bending experiments is was

analyzed utilizing the FEM analysis shown in Section 4.6 scaled to the dimensions of

each of the bending beams. This was done by normalizing the crack length to W and by

normalizing the load to bending stress using $\sigma_b = (3PL)/(2BW^2)$. Based upon the

variation in stress intensity with changing geometry shown by Jaya et al. [185], this is not

116

ideal as each specimen should have an FEM analysis adapted to its precise geometry. The results are shown in Figure 4.19. All the same, a size effect seems to be observed both on the mean value of the fracture toughness, which was reduced as the specimen thickness increased, and in the amount of scatter in the data. These effects could be reasonably explained by dislocation shielding if one considers that the amount of dislocations from the notching is constant with specimen size, constituting a larger effect at the smaller scales. The scatter would arise from the random distribution and orientation of these dislocations.
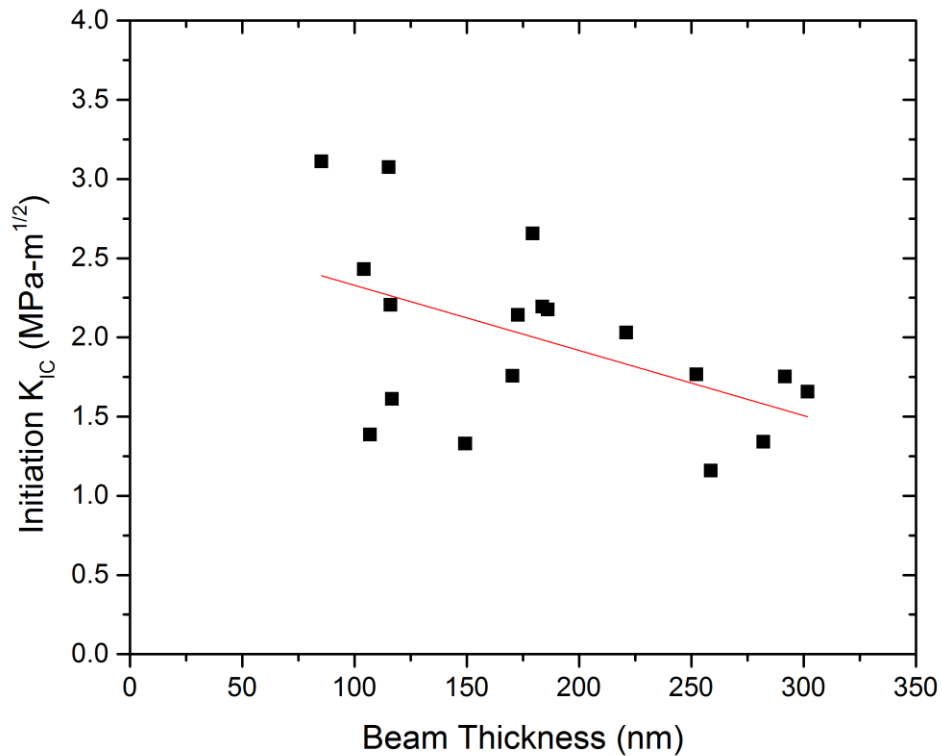
Figure 4.19: K_{IC} values at crack initiation for 18 separate Si nanobeams vs. beam thickness.

An example load-displacement curve with corresponding *in-situ* SEM imaging of a microscale silicon bending beam is shown in Figure 4.20 at room temperature. It should be noted that the room temperature are planned to be repeated with a shorter notch length. This specimen nucleated a small crack in a previous cycle which can be seen to open partway through the loading in Figure 4.20d. The load-displacement cycle shown in Figure 4.20 ends with full catastrophic failure.
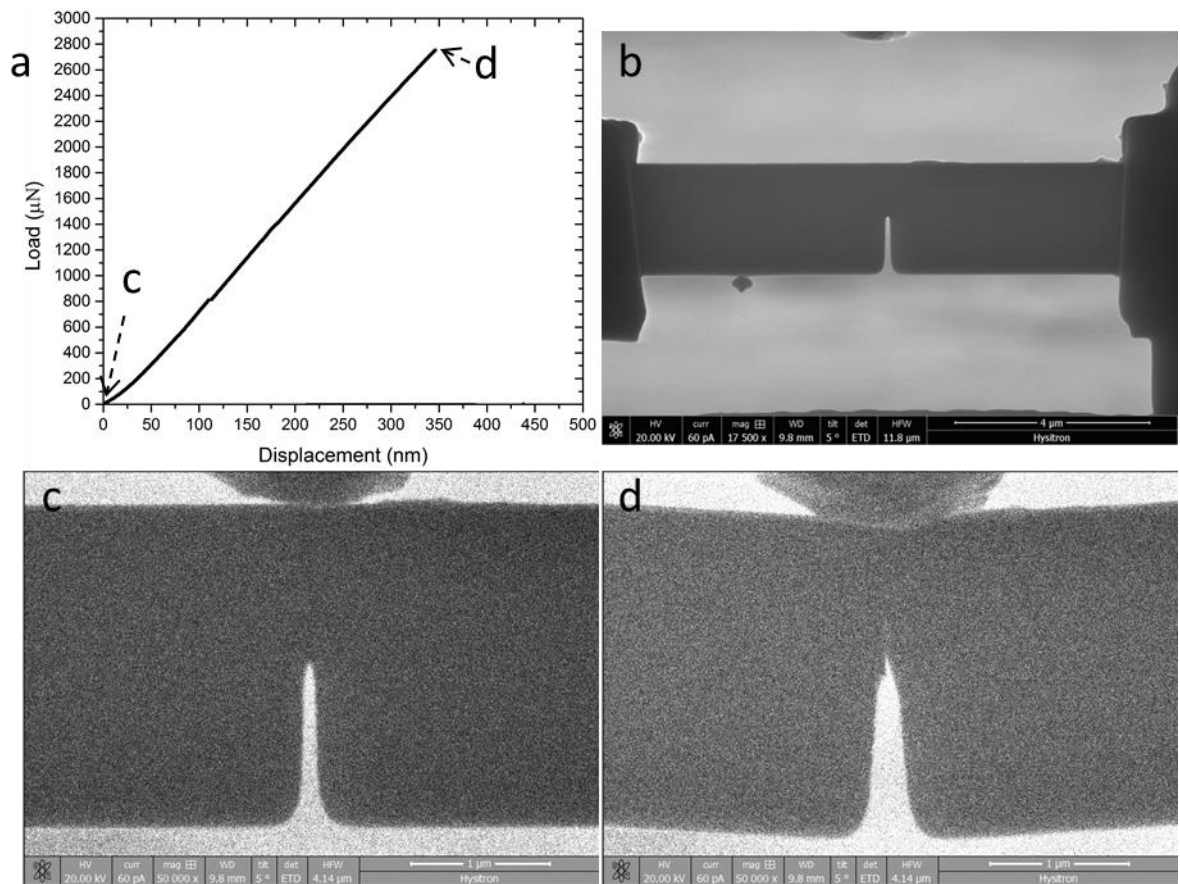
Figure 4.20: a) Load-displacement curve for a 1μm thick beam Si bending beam tested at room temperature b) SEM micrograph of the bending beam before testing and (c,d) images taken from the *in-situ* SEM video.

An example load-displacement curve with corresponding *in-situ* SEM imaging microscale silicon bending beam at 300°C is shown in Figure 4.21. It can be observed that the bending beam underwent multiple discrete crack jumps representing an advance/arrest behavior of cracking with a total of 3 major jumps. At the upper applied load in 4.21f it also appears a slight curl over of the load-displacement curve could indicate plastic deformation, as this curl-over matches the residual displacement upon unloading.
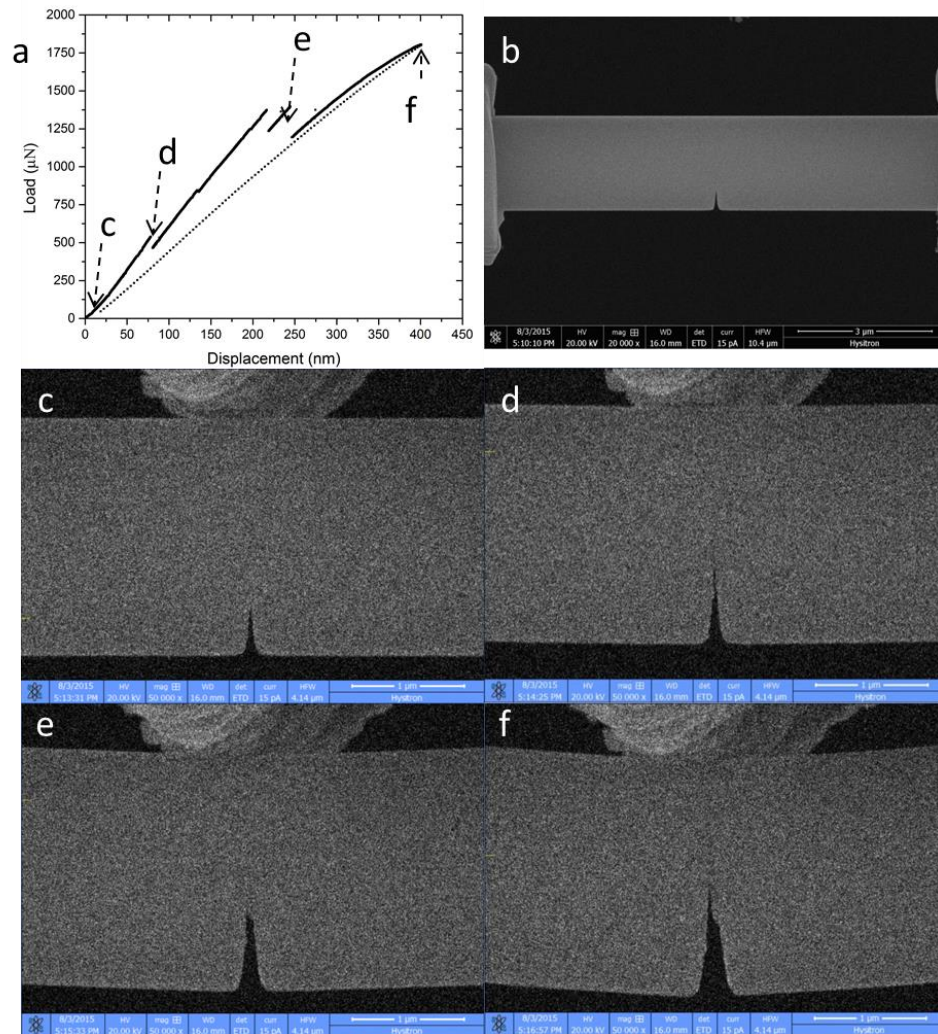
Figure 4.21: a) Load-displacement curve for a 1µm thick beam Si bending beam tested at 300°C b) SEM micrograph of the bending beam before testing and (c-f) images taken from the *in-situ* SEM video showing advance/arrest behavior with slight blunting of the crack tip.

Analysis of the fracture toughness was approximated by using the FEM analysis shown in Section 4.6 scaled in the same manner discussed in Section 4.7.1. Here, the geometrical variation in the bending beams was significantly lower than the nanoscale bending beams, and were a good match for the example case 200nm beam that was analyzed with FEM. The results of this analysis are shown in Fig. 4.22 for K_{IC} versus the crack length a normalized by W. A fairly strong temperature effect is displayed, with decreasing fracture toughness as temperature increases. This is perhaps not intuitive since increased temperature should ease dislocation nucleation and motion and dissipate more energy during the cracking process. It can be observed that as the temperature goes up, more crack tip blunting occurs by comparing Figures 4.20 and 4.21. As shown in Fig. 2.5, the barrier to dislocation nucleation can be greatly reduced at 300°C compared to room temperature. However, the effects of easier dislocation nucleation/motion might not be so straightforward, as dislocations nucleated at a lower stress would move more slowly and provide a stronger shielding effect on the crack tip. The proposed additional experiments at 450°C and 600°C should help understand the transition behavior greatly, as this would cross the traditionally defined DBTT of Si at approximately 400°C. It it hypothesized that drastic increases in K_{IC} would be observed.
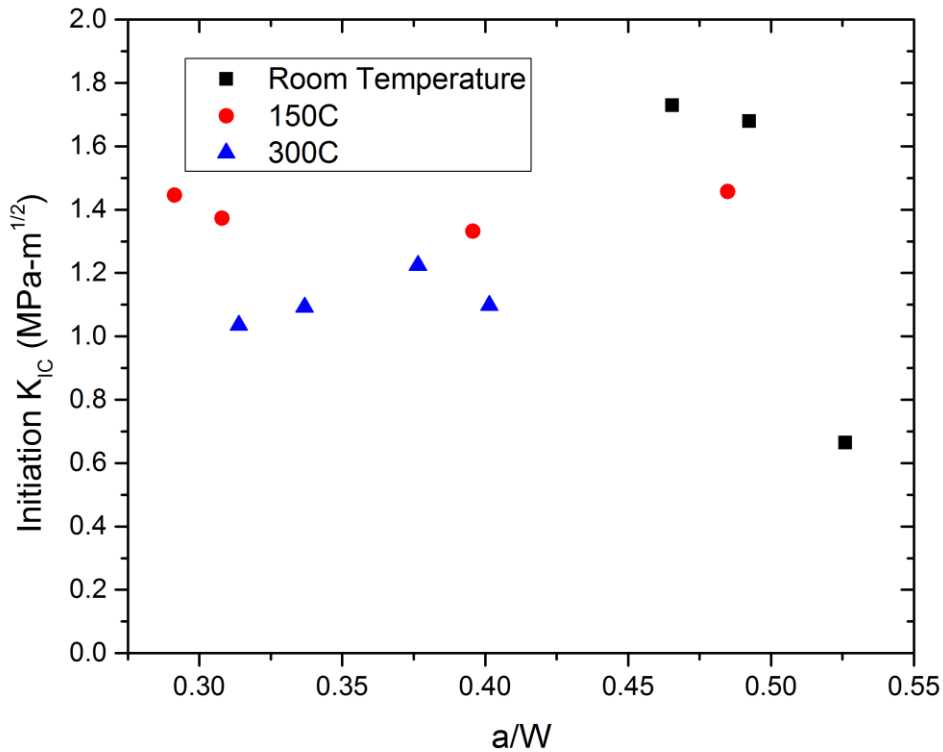
Figure 4.22: K_{IC} values analyzed 1μm thick silicon bending beams vs. a/W, the crack length normalized by the width at three temperatures: RT, 150°C and 300°C.

4.8: Conclusions

In-situ doubly-clamped bending beam experiments were performed *in-situ* in the SEM and TEM, respectively. This testing scheme was demonstrated to give high visibility of the crack tip behavior and stability of the crack front allowing the use of further characterization techniques. This is demonstrated by EBSD scanning between deformation cycles which showed measureable changes in the grain orientations and evolution of the local misorientation ahead of the crack tip in Nitronic 50. Improvements in notch sharpness were also achieved using an electron beam notching approach. Initial analysis showed a reasonable scaling for applied stress intensities with size based upon

available plastic dissipation volume yet the values should not be taken as absolutes considering the number of complicating factors.

This method was then applied to single crystal silicon fracture specimens. Improvements in specimen geometry were employed based on lessons learned from Nitronic 50 testing, including longer span, shallower notches and a blunter tip. Additionally, HF etching techniques to remove FIB damage were successfully employed. A FEM analysis was utilized to determine the effects of the end clamping, which showed a reduction in measured K_{IC} values versus those predicted by the Bakker analysis. A size effect on the fracture toughness was observed across 100-300nm bending beam thickness of decreasing K_{IC} and scatter in K_{IC} with increasing thickness. Bending beams with 1µm thickness were tested with a temperature variation from room temperature up to 300°C. This produced decreasing K_{IC} with increased temperature.

4.9: Future Work

4.9.1: Hydrogen Embrittlement

As discussed in the background section, presence of impurities can have a strong effect on the DBT. It has long been observed that hydrogen can embrittle a variety of metals, particularly high strength alloys like Nitronic 50 which is used as a material for chemical plants and nuclear reactors. Due to its high strength, applications which could supply an ample source of environmental hydrogen could compromise its useful life. The resistance of Nitronic 50 to hydrogen embrittlement is largely unknown.

In order to introduce hydrogen into a material, a number of processes may be utilized. Three methods have been extensively utilized by researchers in the past:

electrochemical, gas phase, and plasma methods. The goal is to produce atomic hydrogen at the surface of a component and drive it into the material with high temperature diffusion. Previous work showed substantial oxidation and contamination on micro/nano scale specimens during electrochemical and gas phase charging for micropillars. It is most dramatic for electrochemical methods that rely on a redox reaction with water, however gas phase charging needs to be performed in an ultra-high purity furnace to avoid oxidation. A comparison of pillars charged by the three methods is shown in Fig. 4.23a,b,c.
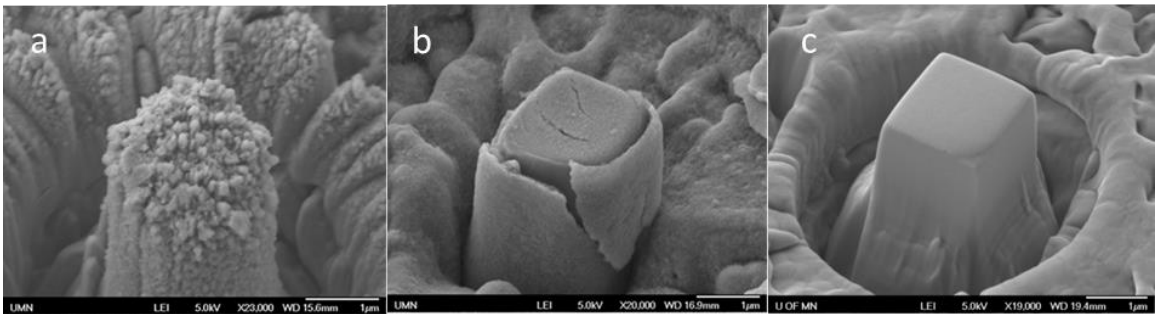
Figure 4.23: SEM micrographs of Nitronic 50 micropillars charged with hydrogen by three methods: a) Electrochemical b) Gas phase c) Plasma.

Plasma charging method produces minimal damage to the pillars. Fig 4.24a shows the pillar in Fig. 4.23c after testing and the corresponding stress-strain curve is shown in Fig 4.24b. It can be seen that the stress values are enhanced compared to the pillar shown in the experimental section, Fig. 4.4, and that qualitatively it appears to have undergone more brittle behavior. How these effects might culminate in the measured fracture toughness of a pre-notched bending beam would be of great interest.
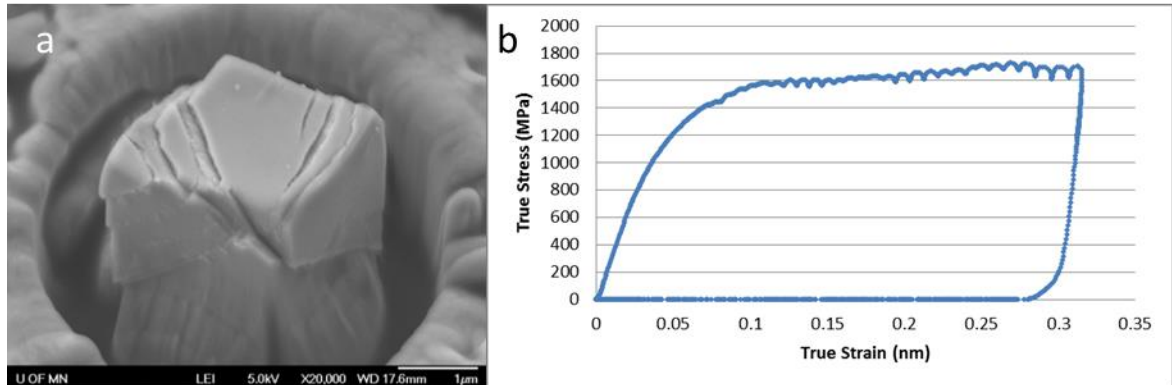
Figure 4.24: a) Post-compression SEM micrograph of plasma hydrogen charged pillar b) Corresponding stress-strain curve.

4.9.2: Other Materials

The techniques presented in this report may be extended to other materials of interest. For metallic systems, tungsten could prove very interesting due to its inherently high brittleness for a metal. It is a material that is of significant engineering interest due to its high stiffness and wear resistance, as well as a barrier layer for fusion reactors [25,206-208]. Another material that can be studied is Fe-3%Si. This material is typically used as a model material for a simple BCC system [208-212] and being a single crystal eases analysis issues such as grain boundaries, grain orientation and migration of alloying elements. Additionally, BCC lattices undergo very strong BDT due to their inherently higher energy dislocation processes.

With some modification to the methodologies used, the experiments presented here could also be performed on insulating brittle material. Specifically, the electrochemical polishing steps could be replaced by ion milling or wedge polishing to produce an area of suitable thickness for FIB fabrication of test specimens. With the addition of a conductive coating for insulating materials, performing identical experiments should be possible. Materials that would be of interest include ceramic

materials that are commonly found in the earth's crust [213,214], such as spinel, MgO, and others. There is some interest in the DBT of such materials, as this is suspected by some geologists to be important for fault formation.

Chapter 5: Analytical Modeling of Dislocation-Crack Interactions

Chapter Overview: A model for the DBT based on the interaction between crack tips and shielding dislocations is developed. The model is validating using example case of hydrogen and strain rate effects for single crystal Fe-3%Si. Next, applications to nano/micro scale experiments are considered, with complicating variables explored using insights gained from the previous chapters.

Adapted from:

Hintsala, E., Teresi, C., Wagner, A. J., Mkhoyan, K. A., & Gerberich, W. (2014). Fracture transitions in iron: Strain rate and environmental effects. Journal of Materials Research, 29(2014), 1513-1521.

E. Hintsala, R. Ballarini and W.W. Gerberich. Future Nanomechanical Approaches to Brittleness Transitions. (In preparation)

E. Hintsala, C. Teresi and W.W. Gerberich. Linking Nanoscales and Dislocation Shielding to the Ductile-Brittle Transition of Silicon. (In preparation)

Collaborators: Claire Teresi, Andrew J. Wagner, Roberto Ballarini

5.1: Motivation

The DBTT is a material property that has important consequences for safety and reliability in applications, but also requires an understanding of the energetics of fundamental deformation processes. It is strongly affected by both strain rate and environment, but a clear understanding of the mechanisms are is still elusive.   What is needed is an analytical model that accounts for all the important parameters governing the DBTT. Steps towards developing such a model are undertaken in this study; the authors contend that the critical concept for understanding the DBTT is crack tip shielding by dislocations, which is strongly affected by temperature, strain-rate and hydrogen. The goal of this study is to develop such a model with a particular focus on the energetics of crack tip plasticity. This model will then be tested by applying it to previously published data, first on fracture toughness measured at different strain rates and secondly on fracture toughness with and without the presence of hydrogen, both as a function of temperature. Next, application of this model to micro and nanoscale specimens is explored. A number of important parameters and variables that need to be accounted for are discussed and a first attempt at fitting to microscale silicon data is presented.

The ultimate goal would be a DBT mechanism map as a function of normal stress, strain-rate, temperature and length scale for a given material. With nanomechanical devices increasingly being employed, the need for such understanding has sufficiently increased to suggest that DBT mechanism maps may become a reality one day. An example of how such a DBT map for silicon might look is shown in Figure 5.1, however there is much lacking data. Here, the x-y plane is the normal temperature-stress axes

with the z-axis being the length scale. This accommodates the length scale effect of increasing flow stress with decreasing size. For yielding, it suggests a transition near 100 nm where the strength increases more rapidly but then drops as 1 nm is approached. This would shift in 3-D space as strain rate either increases or decreases. The strain rate shift is depicted on the back plane where a proposed transition to bulk behavior occurs at 10µm. This crude mechanism map is shown to illustrate the need for models which can simultaneously incorporate time, temperature and length scale to predict critical fracture toughness.
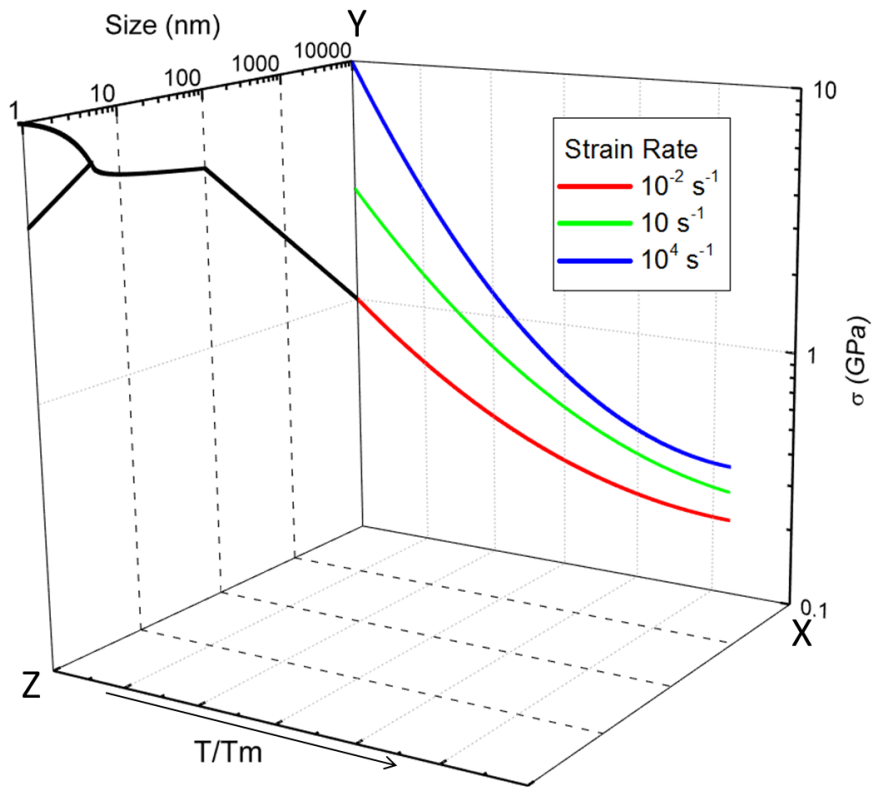
Figure 5.1: Idealized DBT mechanism map for Si as a function of temperature, size and strain rate.

5.2: Model Development

To utilize the crack-tip shielding concept, a kinetic-based, thermally-activated barrier model for the ductile-brittle transition conditions is appropriate. Environmental conditions can be taken into account by modifying the thermal activation parameters. This would include test temperature and applied strain rate (or stress-intensity rate). The basis for such an analytical model was taken from a previous study wherein the dislocation mobility approach of Roberts and Hirsch [30,31] was adopted with a slight variation [215]. This was originally done to evaluate a fracture toughness K_{IC} size effect that had been largely measured on silicon nanoparticles and nanopillars of less than about 500 nm in diameter [64,216,217]. The basis for the model from Appendix B of [215] is presented as Eq. (29), where the critical strain energy release rate, G_{IC}, can be expressed as:

$$G_{IC} = \frac{\eta_0 V^* \sigma^* \varepsilon_p}{\mathrm{b}^2} \qquad\qquad (29)$$

where η_0 is a constant based on Poisson's ratio, V^* is the activation volume for dislocation emission from the crack tip, b the Burger's vector, σ^* the thermal component of the yield stress and ε_p the plastic strain. As such, G_{IC} is proportional to the plastic strain energy in the activation volume divided by the area of initiation of b^2. In Eq. (29), the original derivation used the yield stress σ_{ys} rather than σ^* due to the usage of a different dislocation velocity law than that which will be presented here.

The previous model used the stress dependency as a power law and a corresponding stress free activation energy in the exponential. Here two refinements of the previous model [215] are introduced: a stress-dependent activation energy and a

129

thermally-dependent dislocation velocity law. A stress-dependent activation energy allows for fitting of soft transitions might as well as hard transitions found in silicon. This stress-dependent activation energy can be defined as:

$$H_\sigma = H_0 - \sigma^* V^* \tag{30}$$

where the stress-free activation energy, H_0, is reduced by the stress work. Here, σ^* is the thermal component of the flow stress and is given in terms of how the yield stress σ_{ys} is reduced by an internal or back stress, σ_i, which arises from other strengthening mechanisms such as grain size or pre-existing precipitate or dislocation structures. This gives the thermal component to be:

$$\sigma^* = \sigma_{ys} - \sigma_i \tag{31}$$

as Cottrell and others [22,218] had accomplished previously. Regarding the second proposed change, rather than an empirical power law dependency of σ^m where m might be 1 or more, the Cottrell approach uses a dislocation velocity v of:

$$v = v_0 \exp\left\{- \frac{H_0 - \sigma^* V^*}{kT}\right\} \tag{32}$$

where the prefactor v_0 is a constant. Importantly, this approach incorporates temperature, where the previous did not. Applying Eq. (32) to Eq. (29), with $\dot{\varepsilon}_p = \rho b v$ (where ρ is the dislocation density), in the same way as was developed in Appendix A of the previous model [215], G_{IC} becomes:

$$G_{IC} = \left\{\frac{V^* \Psi_1 \sigma^* \varepsilon_p v_0}{b \dot{\varepsilon}_p}\right\} \exp\left\{- \frac{H_0 - \beta \sigma^* V^*}{kT}\right\} \tag{33}$$

130

with $\Psi_1 = \eta_0 \rho$ (with units m^{-2}) and β a fitting parameter which will be discussed presently. To simplify, one can make the assumption that a failure criterion exists at a single value of $\Psi_0 = \Psi_1 \varepsilon_p v_0 b$, such that

$$G_{IC} = \left\{ \frac{V^* \Psi_0 \sigma^*}{b^2 \dot{\varepsilon}_p} \right\} \exp\left\{ -\frac{H_0 - \beta \sigma^* V^*}{kT} \right\}. \tag{34}$$

Here, Ψ_0 is a fitting parameter as the dislocation density and pre-exponential velocity coefficient are unknown; however all contained parameters could be measured. Here, Ψ_0 would have s^{-1} units and qualitatively is consistent with the order of strain rate effects observed. However, it is unknown how σ^* and V^* will be impacted upon by high strain rates. Since $\sigma^* \sim V^{*-1}$ in many cases, this might not be a serious deficiency outside the exponential as in [215], but inside as proposed here it is more problematic.

There is caution here in that two ways have been used to describe strain rate, one through the dislocation density, $\rho b v$, and one through Eq. (32) such that these must be locally consistent. Roberts [30] has shown nearly a factor of three change in fracture toughness with a change in strain rate of an order of magnitude. Similarly, a drop in K_{IC} of tungsten by a factor of two was observed by Gumbsch, et al [25] with an order of magnitude increase in stress-intensity loading rate. These roughly translate into a drop in G_{Ic} by a factor of 4 -9 meaning that for some materials a linear drop in strain energy release rate might approach that depicted by Eq. (34).

Finally, β represents the local stress variation away from the crack tip such that dislocation velocities decrease with distance after crack-tip emission. This is because the local stress at the crack tip driving emission is different from the stress in the plastic zone

131

responsible for dislocation motion. This is partially due to the crack-tip stress gradient and partially the back stress from the prior dislocation emission. As a result there are unknown increasing stresses resulting from an increase in stress intensity during loading and unknown decreasing stresses from dislocation shielding. Assuming these nearly cancel for a simple analytical solution, a single value of β is picked with which to predict the effects of strain rate, test temperature and thermally-activated parameters on the DBT. As such this is a two-parameter fitting procedure.

The influence of the dislocation velocity on shielding of the crack-tip is proposed to be the dominant factor governing the temperature strain-rate dependence of the fracture toughness. It should be emphasized that because σ^*V^* appears both in the prefactor and in the exponential of Eq. (34) there is a strong coupling of the stress terms. Also still undetermined is the strain rate dependence of σ^*V^*, which may vary based on the material system. Therefore, at this stage of development, the prefactor term is necessarily ad hoc; however, the prefactor of Eq. (34) is still based upon fundamental ideas and can be improved as more definitive experimental data becomes available.

5.3: Experimental Applications to compact tension of Fe-3%Si

To test the model's accuracy, two sets of previously published data on Fe-3%Si [212,219] were used. Fe-3%Si has been utilized frequently as a model material for studying the DBT and hydrogen embrittlement as it can easily be produced as a single crystal.

One data set contains polycrystalline Fe-3%Si with varying strain-rate and the second set contains single crystal Fe-3%Si that has been exposed to atmospheric

hydrogen. For the polycrystals [219], experimental techniques involved small compact round test samples 2.0 mm thick, in a temperature range of 160K to 300K, loaded at an applied stress intensity rate of 0.15 MPa-m$^{\frac{1}{2}}$s^{-1} to 1000 MPa-m$^{\frac{1}{2}}$s^{-1}. For reference, the orientation of the compact round fracture toughness samples with respect to the rolling direction is shown in Figure 5.2. For the single crystals [212], compact round specimens with a thickness of 4.8mm were used, in a temperature range of 100K to 400K at an applied stress intensity rate of 0.035MPa-m$^{1/2}$s^{-1}, both with and without atmospheric hydrogen gas flow. Full experimental details can be found in the referred material. [211, 212,219]
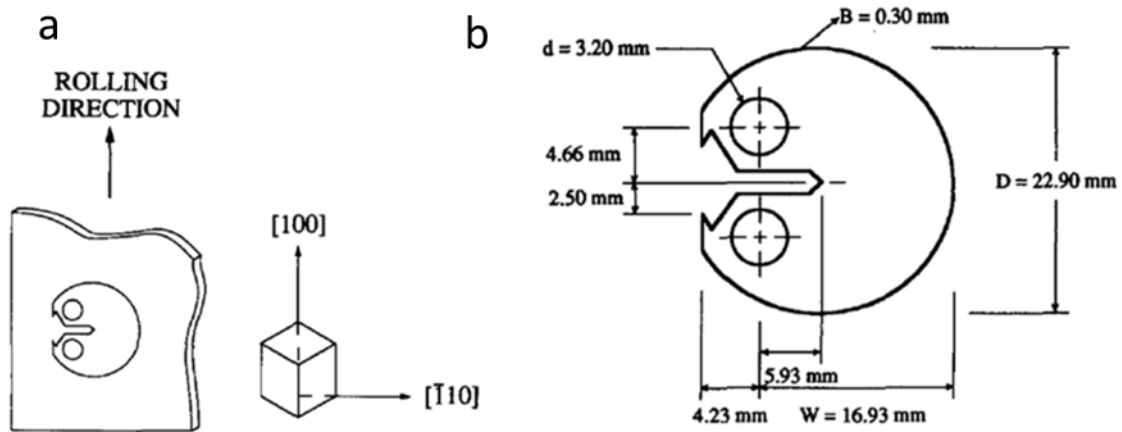
Figure 5.2: Fe-3% Si coarse-grain-oriented samples: a) rolling and crack growth directions; b) compact round tension specimen dimensions. (See Ref. [219]).

5.3.1: Strain Rate Variation of Polycrystalline Fe-3%Si

For the non-hydrogen charged polycrystals, thermally-activated rate parameters of σ_{ys}, σ_i, σ^* are based on data from a study where the yield strengths from the coarse-grain crystals were consistent with reported yield strengths of single crystals at room

temperature (300 MPa for both). With a reasonable value for the internal stress of σ_i = 210 MPa, taken as one intermediate to those between Garafalo [220] and Chen and Gerberich [221], it was also determined how V^* varies with σ^* as shown in Figure 5.3. V^* is typically in the 2 to 100 b^3 range for body-centered cubic iron and its alloys at low temperature [220-224]. The only unknown besides Ψ_0 and β was the strain rate. With these thermally-activated parameters, as summarized in Table 2, Figure 5.3 and Figure 5.4, measured stress intensity fracture toughness values could be compared as a function of strain rate.
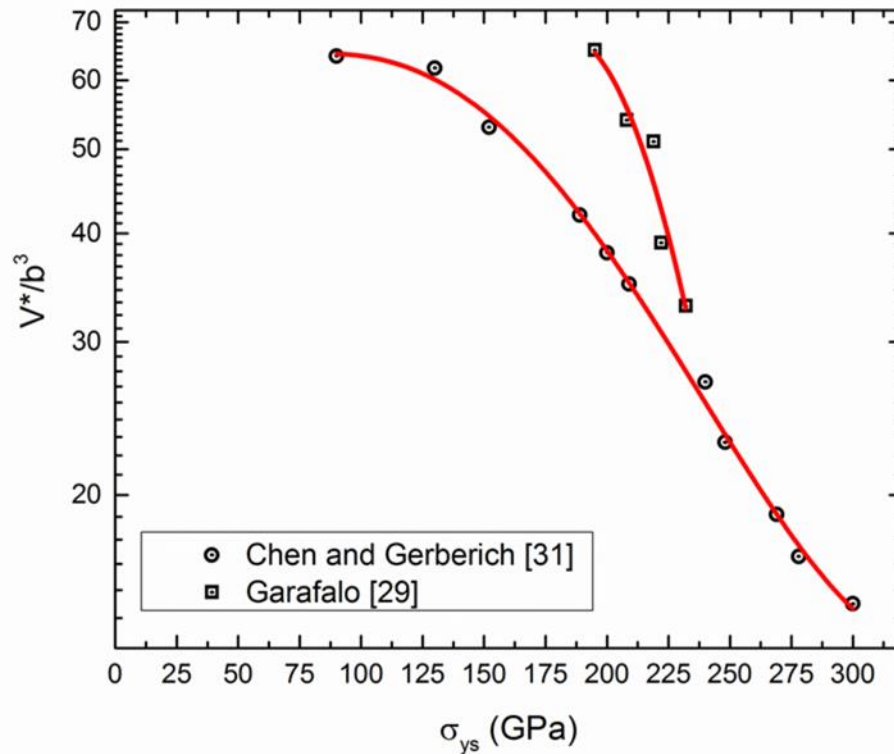
Figure 5.3: Activation volumes in Fe-2.4% Si [220] and Fe-3% Si [221] as a function of the effective shear strength at various temperatures. Red lines represent a power fit of the data.

Table 2: Thermal Activation Stresses and Activation Volumes with and without hydrogen

T	160	180	200	220	240	260	280	300	350
τ^*	210	190	170	151	133	117	103	90	63
V^*	6.7	7.5	8.6	9.8	11	12.1	13.5	15	-
τ_H^*	129	117	105	93	82	72	63	55.5	39
V_H^*	53	62	62.5	63	64	64	64	64	64
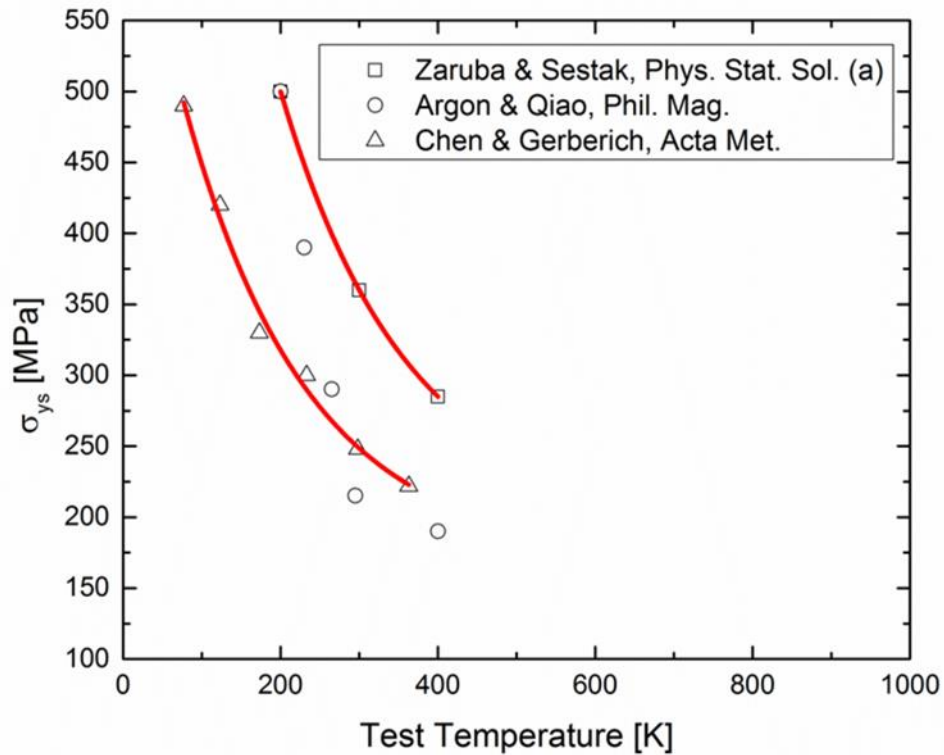
Figure 5.4: Data for yield strength and activation volumes versus temperature as summarized from three sources [210, 212, 225]. Red lines represent a power fit of the data.

For the three selected applied stress intensity rates, strain rates were calculated at the elastic-plastic boundary to be $1.8\text{x }10^{-5}\text{s}^{-1}$, $1.6\text{x}10^{-3}\text{s}^{-1}$ and 0.11 s^{-1}. Use of the yield stress in determining the effective stress and the strain rate from Eqs. (34) and (37) required selecting the distance from the crack tip to be the elastic-plastic boundary. This is accomplished here using a plane-strain estimate for the early stages of yielding, knowing that the same equation also applies to plane stress at the later stages. From McClintock and Irwin's early paper on plasticity at crack tips [226], the continuum representation of the strain distribution for the Mode I analogy of the Mode III result is

$$\varepsilon_p = \frac{R_p}{r}\left(\frac{\sigma_{ys}}{E} - 1\right) \sim \frac{R_p}{r} * \frac{\sigma_{ys}}{E} \tag{35}$$

where R_p is the plastic zone diameter, σ_{ys} and E are the yield strength and modulus and r is the distance from the crack tip. Given that $R_p = \frac{K_I^2}{3\pi\sigma_{ys}^2}$ using the inverse method approximation for the plastic zone size, this gives

$$\varepsilon_p = \frac{K_I^2 \sigma_{ys}}{3\pi\sigma_{ys}^2 Er} \tag{36}$$

This is differentiated with respect to time giving $d\varepsilon/dt$ as $\dot{\varepsilon}$ at $R_p = r$ to be

$$\dot{\varepsilon} = \frac{2\dot{K}_I \sigma_{ys}}{EK_I} \tag{37}$$

A value of $K_I \simeq 30$ MPa-m$^{1/2}$ was used which approximately represented the mean value of K_I applied. Choosing a different value of K_I would only shift the curves in Figures 5.5 and 5.7 slightly, which could be shifted back with a slight variation of Ψ_0. The results for

temperature varying from 160 to 300°C for the three applied stress intensity rates used

are given in Table 3. Values of yield strength from Figure 5.4 were utilized.

Table 3: Values of strain rate, $\dot{\varepsilon}$, vs. temperature for three stress intensity rates

$T =$	160	180	200	220	240	260	280	300	K
0.15 MPa-m$^{1/2}$/s:	2.15	2.00	1.90	1.80	1.71	1.64	1.57	1.50	x10^5 s^{-1}
14 MPa-m$^{1/2}$/s:	1.96	1.87	1.77	1.68	1.60	1.54	1.47	1.40	x10^3 s^{-1}
1000 MPa-m$^{1/2}$/s:	0.14	0.133	0.127	0.120	0.114	0.109	0.105	0.100	x1 s^{-1}

For all three applied stress intensity rates of 0.1 MPa-m$^{1/2}$s^{-1}, 14 MPa-m$^{1/2}$s^{-1} and

1000 MPa-m$^{1/2}$s^{-1}, calculated strain rates were determined over the entire loading range.

These varied about ±15% s^{-1} for each case. For the lowest applied stress intensity rate,

the strain rate ranged from 2.1x10^{-5} s^{-1} to 1.5x10^{-5} s^{-1}, for the intermediate from 1.964x10^{-3} s^{-1} to 1.4x10^{-3} s^{-1} and for the highest from 0.14 s^{-1} to 0.1 s^{-1}. Since variations were small,

singular average values of 1.8x10^{-5}, 1.7x10^{-3}, and 0.12 s^{-1} were used to represent the

stress intensity of 30 MPa-m$^{1/2}$.

5.3.2: Hydrogen Charged Single Crystal Fe-3%Si

For the second part of the analysis, the parameters for the single crystal hydrogen

charged samples are developed. All of the thermal activation parameters coupled with

hydrogen effects could be measured but were not presently available. Some assumptions

regarding how these parameters are affected by hydrogen are made instead. These

assumptions are based on experimental observations originally made by Barnoush and

Vehoff [227] on the ease of dislocation nucleation promoted by hydrogen during

nanoindentation and the conceptual modeling of Kircheim [225] on why this might be so. The critical concept in Figure 5.6 illustrates the difference between no hydrogen and hydrogen-affected dislocation shielding. As used by others [25,29,31,227], it is known that the faster dislocations move away from the crack tip the more shielding one can get. If it takes a high stress to nucleate the first dislocation, then this rapidly moves away from the nucleation site, e.g. the crack tip as illustrated in Figure 5.6a. Alternatively, if a low stress exists due to hydrogen promoting double kink nucleation at the crack tip, the dislocations nucleated move slowly, due to the much lower stresses, as they move out of the high concentration region. This is indicated in Figure 5.6b. As a result, much lower shielding exists with hydrogen than without.

Quantification of this process requires identifying how hydrogen affected both thermal activation parameters, σ^* and V^*. It is assumed that V^* in the presence of hydrogen increased concordantly with the decrease in yield stress as the initial dislocations were emitted. This is indicated in Table 2. Due to the local hydrogen environment, dislocation emission was much easier as has been discussed by Robertson, Sofronis and Birnbaum [48,228] and Kircheim [225]. Also, it was recently confirmed by Barnoush and Vehoff [227] that hydrogen reduced the stress for dislocation nucleation by 61.6 percent. Assuming this reduction was the same for both yield initiation and the thermal component of the flow stress, the tabulated results in Table 2 give much lower values of the thermal component of the flow stress, σ^*_H. As a result, again assuming the scaling could be applied to Figure 5.3, the activation volumes, V^*_H, in the presence of hydrogen were larger by a factor of four to eight. Note here that it was considered that

the shielding was better represented by edge dislocations for the Mode I stress intensity at the crack tip.
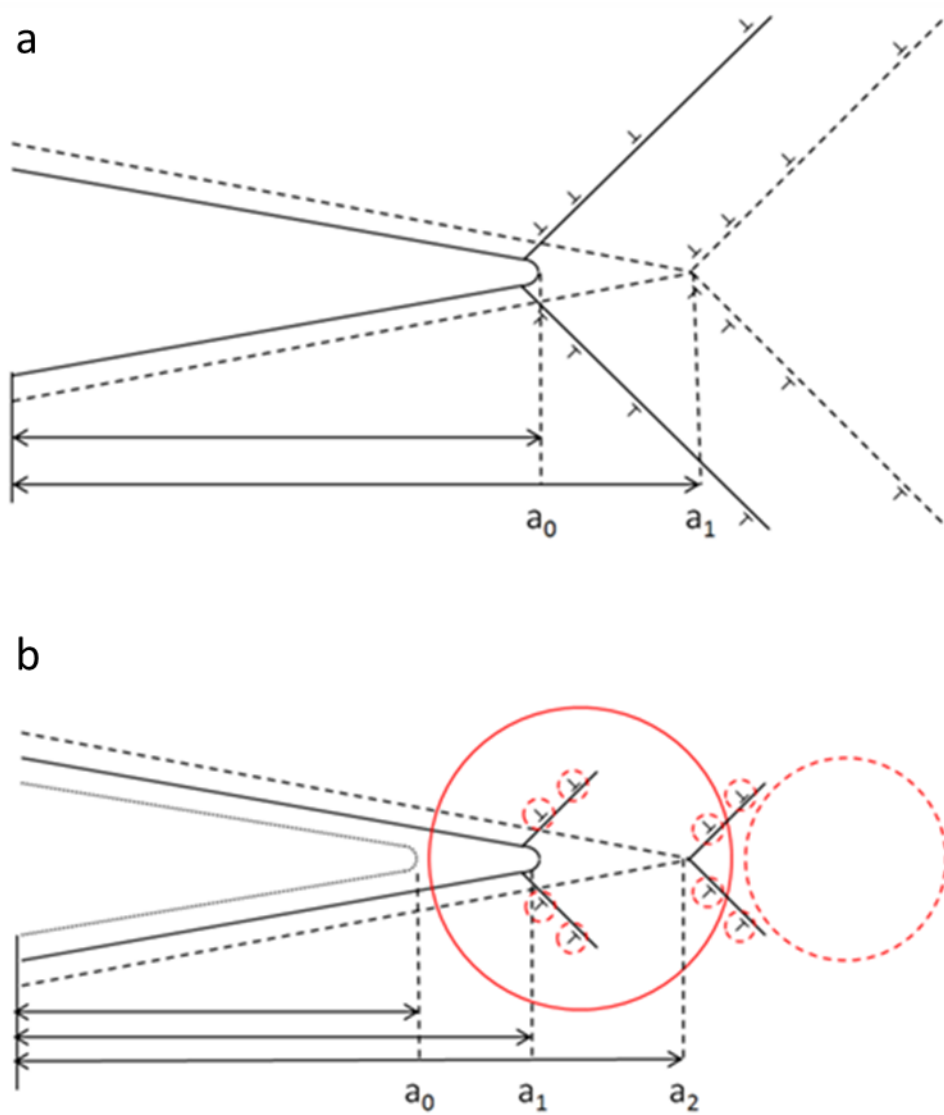
Figure 5.5: Schematic of crack-tip shielding by dislocation for Fe-3% Si (a) without and (b) with hydrogen. Here, a_0, a_1, and a_2 are crack lengths at different stages of propagation, with length increasing with the subscript value for both parts (a) and (b). The circles in (b) represent a hydrogen atmosphere. The number of dislocations in (b) is significantly less than (a).

5.4: Results of Fitting to Fe-3%Si

For the first objective of modeling strain rate effects, using the data from Figures 5.3, 5.4 and Table 2, a two parameter fit was conducted with some success for these polycrystalline samples. This was done for the parameter ranges cited in Table 4 with β and Ψ_0 as the adjustable parameters. For the higher initial dislocation density or density of nucleation sites in the polycrystals, Ψ_0 was higher compared to the single crystals. Here, β was 2.3 and represents an elevation of the local stress associated with the crack tip stress field compared to the uniaxial stress of tension experiments which are normally used to measure dislocation velocities. Ideally, one would utilize a discretized dislocation velocity approach to represent realistic shielding of the crack. While the present analytical approach is inferior to such multi-scale models, it nevertheless captures the shift in transition temperatures as shown in Figure 5.6. It is noteworthy that the slower the applied stress intensity rate, the greater the deviation between the model and experimental data. This is due to the inapplicability of a few of the thermal-activation parameters which were measured on other polycrystalline samples [212,221] because they don't allow for dislocation-defect interactions, which are maximized at slower test rates. In terms of the K_{IC} shift, one finds at 30 MPa-m$^{1/2}$ a shift of 50K and 100K from the lowest to the intermediate and highest strain rates, both experimentally and with Eq. (34). One can rationalize why an upwards shift of the DBTT with increasing strain rate results if this decreases the amount of time for dislocation mobility, thereby decreasing the amount of crack-tip shielding.

Table 4: Summary of parameters used with Eq. (34) to produce theoretical curves in Fig. 5.6 & 5.7

Without Hydrogen	With Hydrogen
Single Crystal	
$H_0^\dagger = 0.8$ eV $= 1.28 \times 10^{-9}$ J/m^2	$H_0^\dagger = 0.8$ eV
160 to 360K: $V^* \sim 6.7$ to 14.9 b^3	$V^* \sim 53$ to 64b$^{3\ \dagger\dagger}$
160 to 360K: $\sigma^* \sim 210$ to 63 MPa	$\sigma^* \sim 129$ to 39 MPa ††
160 to 220K: $K_{IC} \sim 1.24$ to 114 MPa-m$^{1/2}$	$K_{IC} \sim 0.224$ to 17 MPa-m$^{1/2}$
$\psi_0 = 4.4 \times 10^{10}$; $\beta = 3.08$	$\psi_0 = 4.4 \times 10^{10}$; $\beta = 0.58$
Average: $\sigma^* = 136$ MPa; $V^* = 10.8$b^3	Average: $\sigma^* = 80$ MPa; $V^* = 63$b^3
with β: $H_0^* = 0.589 \times 10^{-19}$ J/m$^2 = 0.368$ eV	$H_0^* = (1.28 - 0.447) \times 10^{-19}$ J/m$^2 = 0.521$ eV
Polycrystals	
$H_0^\dagger = 0.8$ eV; $\psi_0 = 9.4 \times 10^{11}$; $\beta = 2.3$	-
160 to 300K: $V^* \sim 6.7$ to 14.9b^3	-
160 to 300K: $\sigma^* \sim 210$ to 90 MPa	-
$\dot{\varepsilon} = 1.6 \times 10^{-3}$ s^{-1}: $K_{IC} \sim 0.125$ to 127 Mpa-m$^{1/2}$	-
Average: $\sigma^* = 130$ MPa; $V^* = 11.2$b^3	-
with β: $H_0^* = 0.709 \times 10^{-19}$ J/m$^2 = 0.444$ eV	-
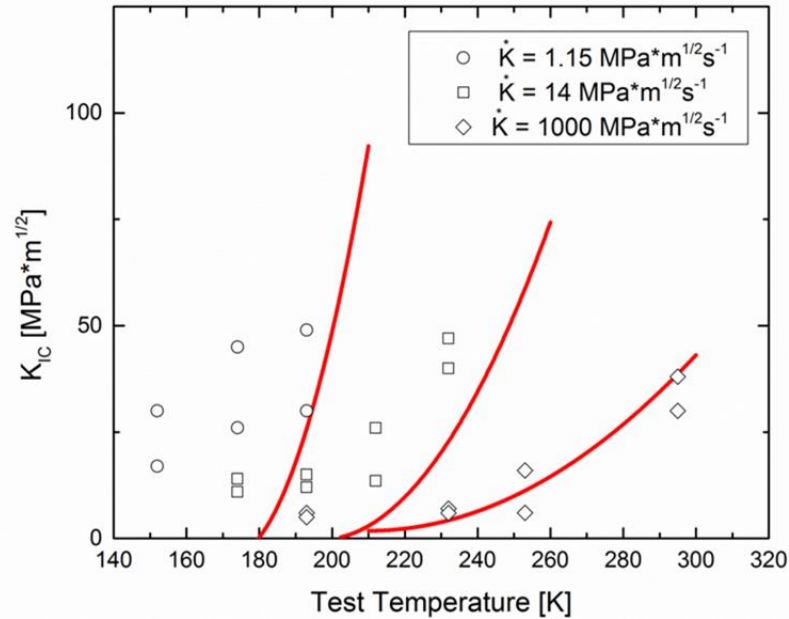
Figure 5.6: Effect of stress-intensity loading rate on coarse-grain fracture toughness showing a shift of 100 K in DBTT with an increase of three orders of magnitude in rate in polycrystalline Fe-3%Si. Solid red curves represent KIC evaluated using Eq. (34) and parameters from Tables 2 and 4.
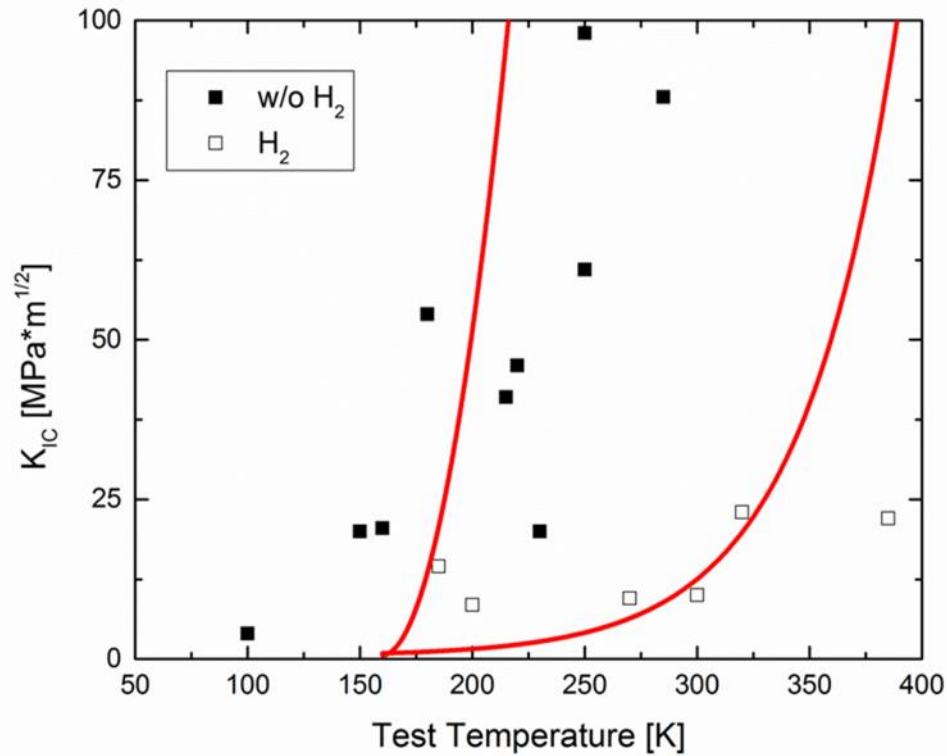
Figure 5.7: K_{IC} vs. temperature at constant applied stress intensity rate for single crystal Fe-3% Si with and without the presence of gaseous hydrogen. Solid red curves represent K_{IC} as determined by Eq. (34) using parameters from Tables 2 and 4.

For the second objective of modeling hydrogen effects, with the parameters of Tables 2 and 4, calculations of the strain energy release rate were conducted and compared to single crystal fracture toughness values in Figure 5.7. Here, β was 3.08 without hydrogen and 0.58 with hydrogen. The model fit to the data using two parameters does capture both the low and higher temperature results, with hydrogen producing a 20K K_{IC} shift at very low temperature and a 150K K_{IC} shift at higher temperatures. It is emphasized that even though the same activation energy of 0.8 eV is used for both cases with and without hydrogen in Table 4, the stress-dependent activation

energy $H_{\sigma*}$ is much different. Here it is 0.368 eV without hydrogen compared to 0.521 eV with hydrogen. The change in $H_{\sigma*}$ and β is consistent with hydrogen trapping or slowing of dislocations which provide less dislocation shielding and higher DBTT temperatures.

5.5: Discussion of Assumptions

A discussion of the assumptions regarding the effects of hydrogen embrittlement is needed, since the situation is complex and they are crucial for the results presented in Figure 5.7. To reiterate, it is assumed that hydrogen decreases $\sigma*$ and increases $V*$, such that their product does not change largely. Nibur, et al [229] demonstrated that hydrogen softens FCC austenitic stainless steel, and Barnoush and Vehoff [227] have found similar results in BCC Fe-3% Si. Theoretically, Kircheim [225], Devincre and Roberts [32] and Itakura, et al [230] also found softening in BCC iron. Alternatively, as deformation proceeds, the resistance to dislocation motion with concentrations of hydrogen can cause hardening, as proposed by Kircheim [225]. Some theoretical and experimental studies [48,227,228] have strongly suggested that hydrogen should lower both the flow stress and the activation volume. Other studies have theoretically and experimentally concluded that hydrogen should either soften or harden the host material depending on the circumstance [32,37,48,228,225,227]. What should be illustrated at this point is that the effects of hydrogen on crack-tip plasticity require additional study. Nevertheless, the moderate success of the model fit in Figures 5.6 and 5.7 should support the physical interpretation outlined in the Methods section and Figure 5.5. Regarding the fitting of Figures 5.6 and 5.7, the polycrystalline and single crystal data could have differences in impurity content, initial dislocation content and unrevealed sub-surface grain boundaries which would cause some of the variation in the values of Ψ_0 and β utilized.

143

It is potentially significant that this simple modeling predicts that the DBTT with hydrogen closely approaches that which is hydrogen free at low temperature. A macroscopic interpretation of this could be that hydrogen does not decrease the cohesive properties of iron as described by the theory of hydrogen-enhanced decohesion (HEDE). One must acknowledge, however, that there are too many assumed or unknown factors that require substantiation prior to making such conclusions.

5.6: Variables affecting the DBT in Silicon

Recent studies by disciplines ranging from geology [231], physics [232], civil engineering [233], materials science [89,157], to theoretical and applied mechanics [234,235] have identified the important materials properties for low temperature DBTs in silicon but a comprehensive theory remains elusive. In Table 5 the key properties related to this phenomenon are listed. These factors have a strong impact on dislocation character, nucleation and mobility which changes plastic energy dissipation processes. These properties themselves are affected by subsidiary variables such as confining pressures [64], state of stress doping levels (e.g. n-doped and p-doped) [236], radiation enhanced dislocation glide (REDG) [237], and length scale [123,238]

Table 5: The DBT: Key Variables Affecting Flow and Fracture

Key Variables:
b - the Burgers vector for full or partial dislocations occurring at the DBTT
σ_{ij}- the applied stress tensor governing pressure, plastic flow and fracture
$\dot{\varepsilon}$- the applied strain rate
T – the temperature
H_0 – an activation energy for dislocation nucleation or mobility
v - the dislocation velocity
E, v- appropriate elastic moduli and Poisson's ratio
γ_s - surface energy
γ_{eff}- an effective "surface energy" which includes plastic energy dissipation
G_{IC} - strain energy release rate related to surface and plastic energies
K_{IC} - fracture toughness thru $[E*G_{IC}]^{1/2}$
V^* - activation volume, same as an activation area times b
τ^* - an effective stress for dislocation nucleation or mobility

Next, three of these parameters are discussed in detail: the flow stress, σ_{flow}, the effective normal or shear stress, σ^* or τ^*, and the activation volume, V^*. This is necessary as the mechanism for producing plasticity may change as dictated by a unique combination of length scale, strain rate and temperature.

5.6.1: Flow Stress

One of the crucial parameters is the flow stress, which is affected by temperature, strain rate, length scale, loading conditions and impurities. Five different studies [64,123,153,159, and Chapter 3] show five different flow stress to length scale relationships. In the 20-100 nm scale regime, near theoretical strengths are observed which then decrease at larger size. The slopes in Figure 5.8 are somewhat similar but at a given length scale, the flow strengths can decrease by more than a factor of two depending on the study. At least some of these differences are due to doping type and

145

concentration [236], contact geometry based on the type of specimen (affecting the state of stress) or REDG effects from *in-situ* experiments [237]. Specimen types included confined bulk pressure [123,153], nanopillars[153,159], nanospheres[64,159] and nanocubes (Chapter 3). This demonstrates the need for careful studies of flow stress to determine the impact of such variables precisely.
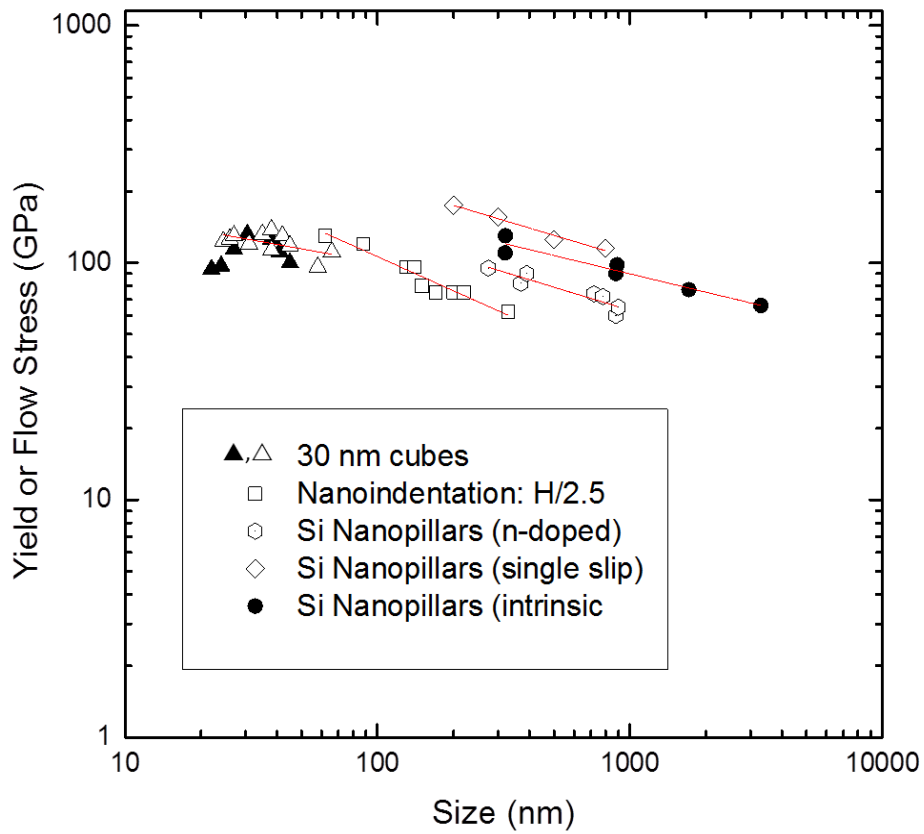
Figure 5.8: Effect of stress state, specimen shape and impurities on the strength/size relation.
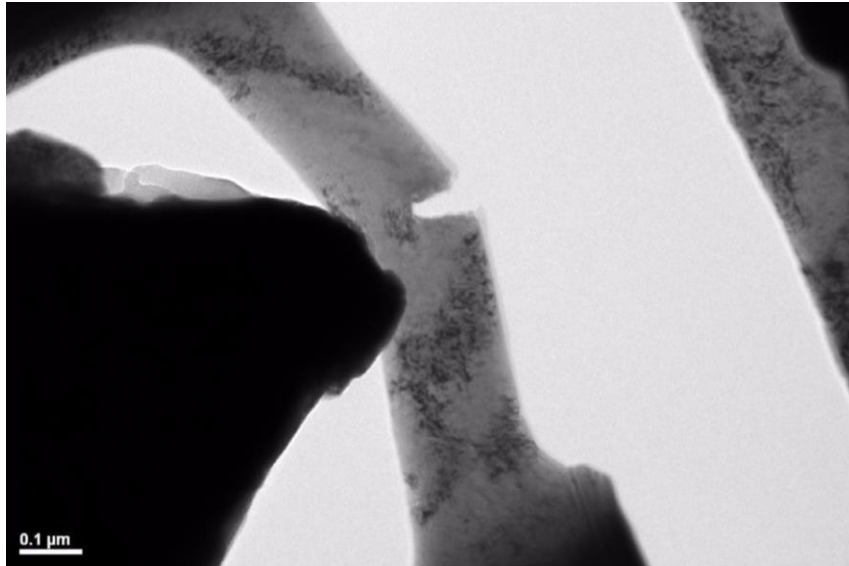
Figure 5.9: Plastic zone size during in-situ loading of a 100nm Nitronic 50 bending beam specimen at peak load.

In terms of dislocation nucleation and motion, the shear stress is the variable of interest for overcoming the Peierls barrier at a given temperature. Determining shear stress requires two things: resolving the applied stress onto the active slip system and subtraction of internal stresses such as the back stress from previously emitted dislocations. Consider the 100nm thick Nitronic 50 pre-notched bending beam sample shown in Figure 5.9, with an initial CTOD of 9.3nm. This image was taken from an *in-situ* TEM video at the maximum plastic zone size for this specimen. This specimen was a single crystal due to the grain size and had the properties, loading conditions for 3-pt. bending, and measurement as shown in Table 6.

Table 6: Back stress estimate from crack-tip emitted dislocations

Material Constants[*]:	b	δ_{tip}	R_p	σ_{bend}	σ_{ys}	E	μ	K_I
nm, GPa or MPa-m$^{1/2}$	0.588	27.63	34.66	4.36	1.8	193	77	3.1

Calculations:

(i) (no back stress) $\qquad K_I = [\sigma_{ys} E \, \delta_{tip}]^{1/2} \;=\;$ $\qquad$ 3.1 MPa-m$^{1/2}$

(ii) (no back stress) $\qquad R_p = K_I^2/2\pi\sigma_{ys}^2 = $ $\qquad$ 1118 nm

(iii) $\qquad\qquad\qquad \sigma_{BS} = 3.41\ GPa$ $\qquad$ See Eq. (16)

(iv) Recalc. w/ BS $\qquad K_{Ieff} = [(4.36 - 3.41)/4.36\,] \, x \, 3.1 \;=\;$ $\qquad$ 0.675 MPa-m$^{1/2}$

(v) Recalc. w/ BS $\qquad R_p = K_I^2/2\pi\sigma_{ys}^2 = $ $\qquad$ 22.38 nm

The back-stress, not knowing the actual slip systems involved, was estimated using Eq. (16) with $l_s \approx 45.7$ nm, $\mu = 77$ GPa, $\nu = 0.28$, $b=0.588$nm with the measured tip displacement of 16.9 nm and an estimate for N, the number of dislocations. N can be estimated using the crack-tip opening displacement of 27.63 nm minus the original CTOD of 9.3nm to find $N= \delta_{tip}/b \approx 31$ which gives a shear back stress of 3.41 GPa if assumed to be resolved to oppose the crack opening with a factor of 0.5. The factor for resolving the stress is a total unknown, but as it varies from 0-1, 0.5 could be considered the most reasonable value. This produced the above recalculated applied stress intensity of 0.675 MPa-m $^{\frac{1}{2}}$. This reduces the calculated plastic zone size to 22.38 nm, which is a factor of .646 of the observed plastic zone size. Reverse calculation yields that a value of 0.466 for the stress resolution would give the exact answer. This oversimplifies the issue for a few reasons. First, it is unknown how many dislocations would be able to escape to the free-surface, or how they might rearrange themselves due the high stress fields in

equilibrium from the crack tip and indenter. Secondly, the effect of tightly packed slip systems is not accounted for here. Another unknown is that even though the neutral axis in the bending beam moves down as the crack grows, which provides the dislocation back stress, the crack-tip region is likely experiencing some of the far field indenter stress field beyond the produced dislocation back stress. This would further reduce the applied stress intensity field, hence diminishing the plastic zone size. Ideally with more careful experimentation, two beam conditions and appropriate g vectors for dark field could allow counting individually all the dislocations present, though this extremely challenging due to the lack of beta tilt capability for the PI-95 PicoIndenter. Regardless, these calculations indicate that the back stress is producing substantial shielding on the crack tip. What this illustrates is that dealing with nanoscale volumes represents few dislocation nucleation sites which are strongly affected by back stresses from even a small number of dislocations.

5.6.3: Activation Volume

With regard to very small length scales less than 10 nm, most work has involved atomistic simulations. One such study explores two important issues. Kang and Cai [239] used a modified embedded-atom-method (MEAM) to study [110]-oriented silicon nanowires under tension with diameters of 2 to 7 nm, strain rates of 5×10^8 sec^{-1} and temperatures of 100 to 1200K. These simulations demonstrated that the [110] wires could undergo a DBT at $d > 4$ nm but failed by ductile shear for smaller dimensions. This size could be shifted by reducing the strain rate to experimental levels, resulting in much larger length scales than 4nm as material fracture resistance diminishes. Regarding

nucleation vs. velocity control, they concluded that the DBT was nucleation controlled in this instance. Clearly, for bulk silicon at high temperature, a strong case for dislocation velocity to be controlling the DBT has been made [155,156]. However, at sub-micron length scales and low temperatures where extremely high stresses promote high dislocation velocities, there might be a transition [240,241].

This transition in activation volume likely signals a mechanism change affecting the activation volume-stress relationship for dislocation nucleation and/or mobility. Consideration of high stresses in metals by Groger *et al*. [240] and silicon by Rabier and Demenet [241], respectively, shows what happens to the dislocation core structure at high stresses. For example, they demonstrate a very gradual change of V^* at shear stresses of 400 to 800 MPa in Mo (close to the Peierls stress) as $V^* \sim 1\ b^3$ is approached. At these stress levels, the core structure could undergo complex changes which would affect the kink formation rate [240].   A similar effect was suggested for Si by Rabier and Demenet [241], who used weak-beam TEM imaging to show full dislocations splitting into two a/6[112] partials. In Chapter 3, it was demonstrated that near-theoretical stresses of 12GPa could be achieved in the initial stages of deforming dislocation-free nanocubes compressed along the [001] axis. Continued deformation then dropped to 8GPa, followed by strain hardening. Based on this stress drop, it seems that high internal stress (>1GPa) is responsible for the activation volume transition. This in turn would change the effective stress for continued plastic flow.

Generally, it is most appropriate to use an effective stress to assess activation volume. This is not essential if crack initiation occurs in dislocation free single crystals. For that reason low dislocation density single crystal silicon are used to determine V^*,

recognizing that repeated strain-rate jump tests may be performed in increasingly dislocated regions which would increase the magnitude of any back stress. It is assumed here that an average back stress contribution would slightly vary V^*.

Nanowires or nanopillars have typically been used to measure activation volumes in tension or compression as defined by [242]

$$V^* = {k_B T}/{S} \tag{38}$$

where S is the strain rate sensitivity defined by $= k_B T \ (\partial ln\dot{\gamma}/\partial\tau)_T$, giving

$$V^* = k_B T \ (\partial ln\dot{\gamma}/\partial\tau)_T. \tag{39}$$

Using this to determine V^* from literature data [152,236,243] for both high temperature data from bulk single crystals [236,243] and low temperature, high stress-data from nanopillars[152], gives the relationship in Figure 5.10. Here it is seen that the macroscopic data has a fairly steep rise above 600K. The micro/nano data depend more gradually on temperature above 600K and below are nearly independent of temperature. This is perhaps not surprising since the volumes below 600K are near 1 b^3 and it seems unlikely that either nucleation or mobility could have activation area much less than the spacing between atoms. Others have discussed the existence of a mechanism change below 600K [152,239,244]. With τ^* increasing as temperature is lowered below 600K and V^* being relatively constant, the product of the two increases. Using the normal thermally-activated stress dependent activation energy for dislocation mobility, H_σ, as given previously by Eq. (30), $H_\sigma = H_0 - \beta\tau^*V^*$, results in reduced activation energy with a strong impact on the DBT. This allows for an apparent energy to be measured based

upon a stress-free activation enthalpy, H_0 , and the effective stress – activation volume term.
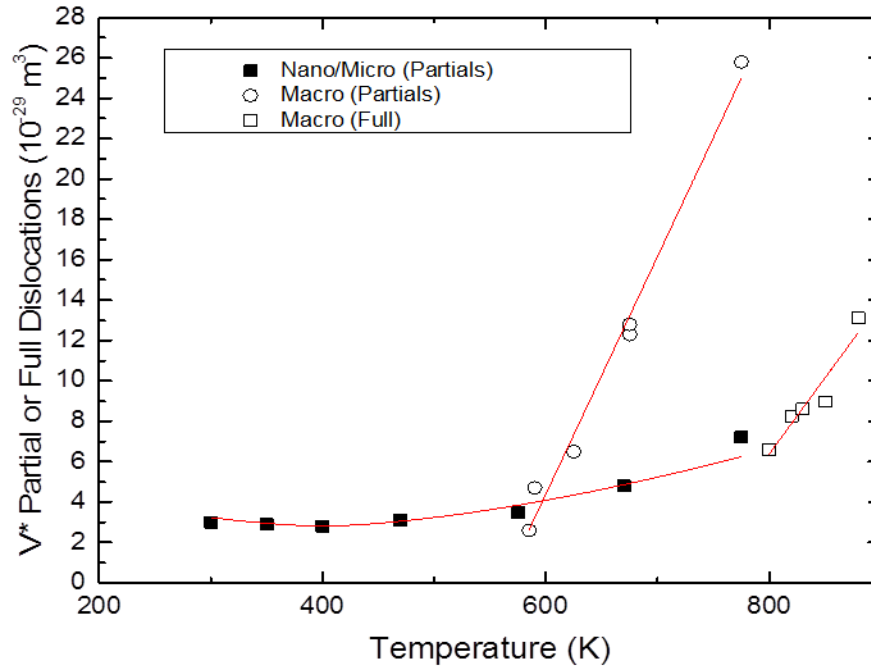
Figure 5.10: Activation volumes for partial dislocations at high stress, low T (■) and for lower stress, higher temperature partial dislocations (O) and full dislocations (□).

5.6.4: Subsidiary Variables

These variables are not going to be explicitly considered in the model but are important to keep in mind. The REDG effect is important since most studies of length scale effects at sub-micron sizes are accomplished using electron microscopes. It has been observed that with increasing electron radiation, e.g. 300keV vs. 100 keV, that dislocation velocities can increase [245], however studies of silicon nanospheres by both atomic force microscopy [64] and transmission electron microscopy [159] resulted in similar flow stress behavior. This effect remains somewhat mysterious but could be incorporated into the activation energy term, as well as in the temperature if the local temperature variations from beam heating could be characterized. Regarding phase transformation effects, this has been clearly observed under the pressure provided by nanoindentation [246] and was the most likely explanation for the Moiré pattern shown in Chapter 3. This phase transformation relieves a substantial amount of stress upon occurrence and would affect the τ^*V^* term. Considering dopant levels, extensive studies [237,238] have demonstrated that p-doping can favor enhanced dislocation velocities compared to intrinsic silicon, impacting dislocation shielding and τ^*V^*.

5.7: Ductile-to-Brittle Transition in Silicon Fitting

Now applying Eq. (34) to single crystal silicon data, Ψ_0 can be set to 1/s since there is little to no native dislocation density. With $\dot{\varepsilon}$ representing the strain rate and Ψ_0 as unity, the only adjustable parameter is β. Utilizing the data from Figures 5.8 and 5.10 to estimate τ^*V^*, setting β = 1.6 gave the values of K_{IC} shown in Figure 5.11 as a function of temperature near 300 K. As used by Ando *et al.* [160], a stress-free activation energy

of 0.88 eV was selected. This compared favorably with their experimental values regardless of using full or partial dislocations using data from [152]. One might expect the partial dislocation calculations to fit better rather than the full dislocation ones at this length scale. However, since there are many variables including orientation, doping and the REDG effect, it is surprising that the fit is this good with only one adjustable constant. One may also consider then that the transition in activation volume seen in Fig. 5.10 may also be due to dislocation nucleation rather than dislocation velocity. In future simulation investigations this would represent an additional avenue to explore. With this data and the activation energy determined from the experimental study [153,236], the fracture toughness was determined from Eq. (34) as shown in Figure (5.11).
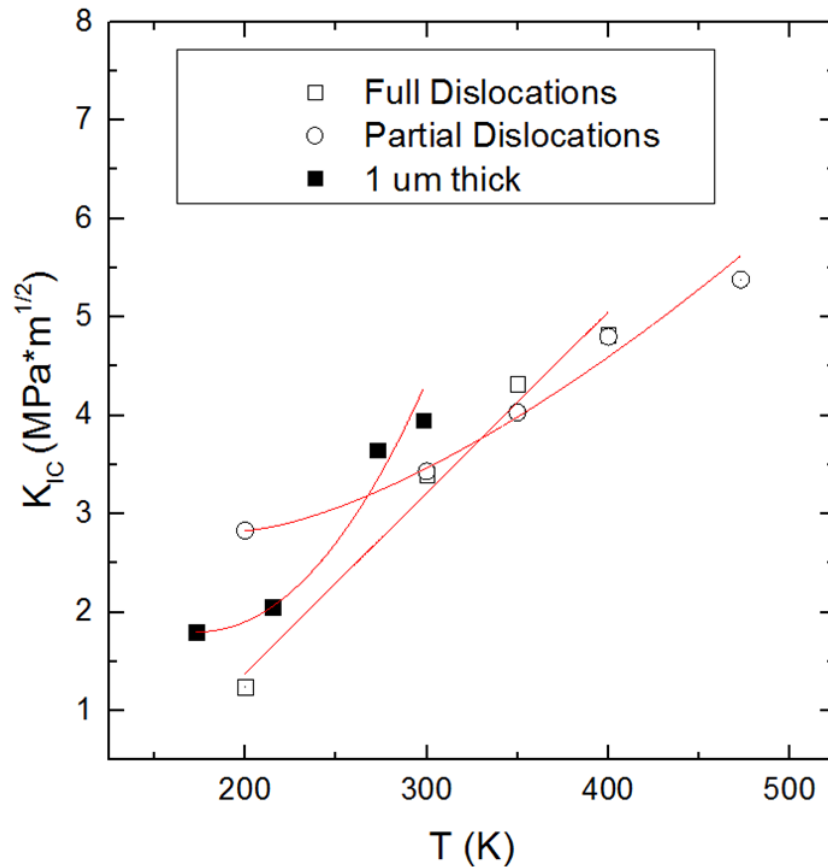
Figure 5.11: Fracture Toughness of 1 μm thick beams [160] compared to Eq. (34).

A final caveat is that even with the proximal agreement in Fig. 5.11, it is emphasized that parameters used to determine $\tau^* V^*$ have been taken from several different studies [123,152-154]. This allows for variation of $\tau^* V^*$ in the exponential giving some flexibility in analysis. Even with that reservation, however, one would prefer an approach which includes comprehensive parameter measures of fundamental quantities that allow atomistic simulation. This should eventually provide realistic comparisons to substantiate verification between experiment and theory.

5.8: Conclusions

To summarize, using previously published data, insight as to how dislocation shielding affects the ductile to brittle transition of Fe3%Si both without and with the involvement of hydrogen is presented. The key, as others have postulated above, is thermal activation of dislocation processes at the crack tip.

Regarding the applications to silicon, the preliminary promise of *in-situ* TEM and SEM evaluations of nano- and micro- scale samples which can supply needed parameters to better understand small scale mechanical properties has been shown. This applies to properties measured at intermediate to near theoretical stresses which govern both plasticity and fracture of semi-brittle intermetallic, semiconductor and ceramic crystals. While this is premature to being used for engineering applications, it is believed all that is proposed is near at hand.

5.9: Future Work

In Table 4, it is seen that all values are the same both with and without hydrogen except for β and the hydrogen affected thermal activation parameters, σ^*V^*. Comparing β for no hydrogen (3.08) to with hydrogen (0.58) might imply that hydrogen should really decrease the activation volume even for the assumed edge dislocations as they move away from the crack tip region. This requires additional experimental and theoretical study. Experimentally, thermally-activated parameters are best measured on the same samples that have produced fracture toughness results, including the variation of σ^* and V^* with temperature and strain rate. With validated comparison between nanoindentation and uniaxial tests, this could be possible. Theoretically, additional studies of dislocation shielding using discretized dislocation dynamics and/or density functional theory and edge dislocations with and without hydrogen would be insightful.

Indentation, sphere and nanopillar evaluations in the size range of 30 to 1000 nm were utilized to evaluate τ^*V^*. As all of these were in compression and fracture instabilities are generally associated with silicon in tension, the role of length scale is not totally addressed by these experiments. With similar evaluations using thicker samples at elevated temperature and techniques developed for an SEM as discussed in Chapter 4, many of the parameters of Table 5 can be evaluated. For example, in progress are both activation energy and activation volume measurements as a function of temperature and strain rate. In principle with an appropriate model this would allow measurement of nearly all of the critical parameters which can also be accessed by atomistic simulations coupled to multiscale discretized dislocation models.

Chapter 6: Summary

In Chapter 3, Si nanocube compression experiments were presented. Mechanical behavior was characterized and was seen to be composed of upper-lower yield behavior followed by linear hardening. The measured yield stresses were near to the theoretical strength as is typical for defect-free nanomaterials, but the elastic limit of 0.07 strain, upper yield strain of 0.11 strain and onset of hardening around 0.5 strain are substantially enhanced compared to other comparable bending and tension experiments for nanowires. Next, plasticity mechanisms were explored for these NCs using high resolution imaging and dark-field experiments. Findings included a dislocation embryo which appeared to consist of a local phase transformation at the contact surface of the NC and substantial plasticity by partial dislocations. Lastly, the hardening behavior was fit using a dislocation pile-up model which achieved reasonable success. Compression of particles at this scale required special modifications of the *in-situ* indentation equipment to reduce lateral vibrations which were unresolved by the axial transducer.

In Chapter 4, exploration of an *in-situ* fracture testing method utilized pre-notched doubly-clamped bending beams was undertaken. Two model materials were utilized, Nitronic 50, and Si. Test specimens were fabricated using FIB machining. Improvements in notch sharpness were achieved by utilizing a converged TEM beam as compared to FIB. *In-situ* SEM experiments were carried out and included EBSD scanning to track deformation. *In-situ* TEM experiments showed indications of dislocation activity and allowed estimation of the plastic zone in some of the cases.

Initial analysis efforts were carried out despite numerous shortcomings in the methodology employed. Many refinements were made towards testing the Si bending beams, including improved geometry to limit complication of the stress field, HF etching to remove residual FIB damage and use of a blunter tip. Initial FEM models were employed to characterize the complex stress state, which resulted in appropriate values for fracture toughness. Initial high temperature testing of Si microbeams was also carried out as a proof of concept.

In Chapter 5, a dislocation-shielded crack tip model for the DBT was developed which utilized a stress-dependent activation energy and temperature dependent dislocation velocity law. There was reasonable success in fitting this model to pre-existing data for compact tension specimens of Fe-3%Si at varied strain rates and in the presence of atmospheric hydrogen. Next, applications of this model to nano/micro scale silicon fracture specimens were explored with the confounding variables and important considerations outlined. In particular, the flow stress variations, enhanced back stresses similar to the fitting employed in Chapter 3 and activation volume changes were discussed for nanoscale specimens. An initial fit utilizing the fracture toughness model was moderately successful.

References

[1] W.W. Gerberich, W.M. Mook, C.R.Perrey, C.B. Carter, M.I. Baskes, R. Mukherjee, A. Gidwani, J. Herberlein, P.H. McMurry, S.L. Girshick, "Superhard silicon nanospheres." J. Mech. Phys. Solids 51 (2003): 979-992

[2] M.D. Uchic, D.M. Dimiduk, J.N.Florando, W.D. Nix, "Sample dimensions influence strength and crystal plasticity." Science 305 (2004): 986-9

[3] C.A. Volkert, E.T. Lilleodden, "Size effects in the deformation of sub-micron Au columns." Philos. Mag. 86 (2006): 5567-79.

[4] S. H. Oh, et al., "In situ observation of dislocation nucleation and escape in a submicrometre aluminium single crystal." Nature materials 8 (2009): 95-100.

[5] M. Legros, D. S. Gianola, and C. Motz, "Quantitative in situ mechanical testing in electron microscopes." MRS bulletin 35 (2010): 354-360.

[6] Z. Shen, R. H. Wagoner, and W. A. T. Clark, "Dislocation and grain boundary interactions in metals." Acta Metallurgica 36 (1988): 3231-3242.

[7] S. Wurster, et al., "Micrometer-Sized Specimen Preparation Based on Ion Slicing Technique." Advanced Engineering Materials 12 (2010): 61-64.

[8] R. J.Arsenault and N. Shi, "Dislocation generation due to differences between the coefficients of thermal expansion." Materials Science and Engineering 81 (1986): 175-187.

[9] S. Amelinckx, The direct observation of dislocations. Vol. 964. New York: Academic Press, 1964.

[10] D. Hull and D.J. Bacon, Introduction to Dislocations. 3rd Edition. International Series on Materials Science and Technology, Volume 37. Pergamon Press. 1984

[11] J.P. Hirth and Jens Lothe, "Theory of dislocations." (1982).

[12] R. Peierls, Proc. Phys. Soc. London 52 (1940): 34.

[13] F.R.N. Nabarro, Proc. Phys. Soc. London 59 (1947): 256.

[14] E. Schmid and W. Boas, "Plasticity of crystals." (1950).

[15] R.W. Hertzberg, Deformation and fracture mechanics of engineering materials. Vol. 89. New York: Wiley, 1996.

[16] A. A. Griffith, "The phenomena of rupture and flow in solids" Philosophical Transactions of the Royal Society of London, A 221 (1921): 163–198.

[17] A.H. Cottrell, Proc. Roy. Soc. A, 1963, vol. 279, pp. 1-10.

[18] T.L. Anderson, Fracture mechanics: fundamentals and applications. CRC press, 2005.

[19] D. S. Dugdale, "Yielding of steel sheets containing slits." Journal of the Mechanics and Physics of Solids 8.2 (1960): 100-104.

[20] B. A. Bilby, A. H. Cottrell, and K. H. Swinden, "The spread of plastic yield from a notch." Proceedings of the Royal Society of London. Series A. Mathematical and Physical Sciences 272.1350 (1963): 304-314.

[21] J.R. Rice, "A path independent integral and the approximate analysis of strain concentration by notches and cracks." Journal of applied mechanics 35.2 (1968): 379-386.

[22] A. Kelly, W.R. Tyson and A.H. Cottrell, "Ductile and brittle crystals." Philos. Mag. 15 (1967): 567-586.

[23] G.I. Barenblatt, "The mathematical theory of equilibrium cracks in brittle fracture." Adv. Appl. Mech 7 (1962): 55-129.

[24] C.St. John, "The brittle-to-ductile transition in pre-cleaved silicon single crystals." Philos. Mag. 32 (1975): 1193-1212.

[25] P. Gumbsch, "Modelling brittle and semi-brittle fracture processes." Materials Sci. and Engng. A 319-321 (2001): 1-7.

[26] I.-H. Lin R. and Thomson, "Cleavage, Dislocation Emission and Shielding for Cracks Under Load." Acta Metall. 34 (1986): 187-206.

[27] M.J. Lii, X.F. Chen, Y. Katz and W.W. Gerberich, "Dislocation modeling and acoustic emission obseration of alternating ductile/brittle events in Fe-3 wt% Si crystals." Acta. Mater. 38 (1990): 2435-2453.

[28] P.G. Marsh and W.W. Gerberich, "A microscopically-shielded Griffith criterion for cleavage in grain-oriented silicon steel." Acta Metall. Mater. 42 (1994): 613-619.

[29] J. Samuels, S.G. Roberts and P.B. Hirsch, "The brittle-to-ductile transition in silicon." Mat'ls. Sci. and Engng A. 105 (1988): 39-46.

[30] J. Samuels and S.G. Roberts, "The brittle-ductile transition in silicon. I. Experiments." Proc. Roy. Soc. London A 421 (1989): 1-23.

[31] S.G. Roberts and P.B. Hirsch, "Modelling the upper yield point and the brittle-ductile transition of silicon wafers in three-point bend tests." Philos. Mag. A 86 (2006): 4099-4116.

[32] B. Devincre and S.G. Roberts, "Three-dimensional simulation of dislocation-crack interactions in BCC metals at the mesoscopic scale." Acta Mater. 44 (1996): 2891-2900.

[33] Y. Qiao and A.S. Argon, "Cleavage cracking resistance of high angle grain boundaries in Fe-3% Si alloy." Mechanics of Materials 35 (2003): 313-331.

[34] H. Huang and W.W. Gerberich, "Crack-tip dislocation arrangements for equilibrium - II. Comparisons to analytical and computer simulation models." Acta. Metall. Mater. 40 (1992): 2873-2881.

[35] J. Song and W.A. Curtin, "Atomic mechanism and prediction of hydrogen embrittlement in iron." Nature Mater. 12 (2012): 145-151.

[36] A. Giannattasio and S.G. Roberts, "Strain-rate dependence of the brittle-to-ductile transition temperature in tungsten." Philos. Mag. 87 (2007): 2589-2598.

[37] R. A. Oriani and P. H. Josephic, "Effects of hydrogen on the plastic properties of medium-Carbon steels." Metallurgical Transactions A, 11 (1980): 1809-1820.

[38] G. D. Samolyuk, Y. N. Osetsky, and R. E. Stoller, "The influence of transition metal solutes on the dislocation core structure and values of the Peierls stress and barrier in tungsten." Journal of Physics: Condensed Matter 25.2 (2013): 025403.

[39] K. Ono and A. W. Sommer, "Peierls-Nabarro hardening in the presence of point obstacles." Metallurgical Transactions 1.4 (1970): 877-884.

[40] Y. Yamashita, F. Jyobe, Y. Kamura and K. Maeda, "Hydrogen enhanced dislocation glide in silicon." Phys. Status Solidi. A, 171 (1999): 27.

[41] M. Brede and P. Haasen, "The brittle-to-ductile transition in doped silicon as a model substance." Acta Metallurgica, 36 (1988): 2003-2018.

[42] H. Idrissi, G. Regula, M. Lancin, J. Douin and B. Pichaud, "Study of Schockley partial dislocation mobility in highly N-doped 4H-SiC by cantilever bending," Phys. Stat. Sol. ©, 2 (2005): 1998-2003.

[43] N.O. Petch and P. Stables, Nature 169 (1952): 842.

[44] A.S. Tetelman and W.D. Robertson, Trans. AIME 224 (1962): 775.

[45] A.S. Tetelman and S. Kunz in "Stress-corrosion cracking and hydrogen embrittlement of iron-based alloys," edited by R.W. Stahle (NACE. Proc., Firminy, France, 1973) p. 359

[46] W.W. Gerberich, P.G. Marsh, J.W. Hoehn, in "Hydrogen Effects on Materials," edited by A.W. Thompson and N.R. Moody (TMS, Warrendale, PA, 1996) p.539

[47] C.D. Beachem, Metall. Trans. 3 (1972): 437.

[48] I.M. Robertson and H.K. Birnbaum, "An HVEM study of hydrogen effects on the deformation and fracture of nickel." Acta. Metall. 34 (1986): 353-386.

[49] J. Eastman, F. Heubaum, T. Masumoto and H.K. Birnbaum, Acta. Metall. 30 (1982): 1579.

[50] H.K. Birnbaum and P. Sofronis, in "Hydrogen Effects in Materials," edited by A.W. Thompson and N.R. Moody (TMS, Warrendale, Pa, 1996).

[51] C. Altstetter and D. Abraham, in 'Hydrogen Effects in Materials," edited by A.W. Thompson and N.R. Moody (TMS, Warrendale, Pa, 1996) p. 599

[52] P.D. Hicks and C.J. Altstetter, in "Hydrogen embrittlement of superalloys," edited by A.W. Thompson and N.R. Moody (TMS, Warrendale, Pa, 1989) p. 613.

[53] E. Arzt, "Size effects in materials due to microstructural and dimensional constraints: A comparative review." Acta Mater. 46, 16: (1998): 5611-5626

[54] E.O. Hall, "The Deformation and Ageing of Mild Steel: III Discussion of Results". Proc. Phys. Soc. London 64 (1951): 747–753.

[55] N.J. Petch, "The Cleavage Strength of Polycrystals." J. Iron Steel Inst. London 173 (1953): 25–28.

[56] R. Dingreville, J. Qu, C. Mohammed, "Surface free energy and its effect on the elastic behavior of nano-sized particles, wires and films." J. Mech. Phys. Solids 53, 8 (2005): 1827-1854.

[57] L.G. Zhou and H. Huang, "Are surfaces elastically softer or stiffer?" Appl. Phys. Lett. 84, 11 (2004): 1940-1942.

[58] M.J. Kobrinsky, G. Dehm, C.V. Thompson, E. Arzt, "Effects of thickness on the characteristic length scale of dislocation plasticity in Ag thin films." Acta Mater. 49 (2001): 3597-3607.

[59] T.T. Zhu, A.J. Bushby, D.J. Dunstan, "Size effect in the initiation of plasticity for ceramics in nanoindentation." J. Mech. Phys. Solids (2007).

[60] S. Baker, "Plastic deformation and strength of materials in small dimensions." Materials Science and Engineering A319-321 (2001): 16-23.

[61] W.W. Gerberich, N.I. Tymiak, J.C. Grunlan, M.F. Horstemeyer, M.I. Baskes, "Interpretations of indentation size effects." Journal of Applied Mechanics, Transactions ASME 69 (2002): 433-422.

[62] J.M. Jungk, W.M. Mook, M.J. Cordill, M.D. Chambers, W.W. Gerberich, D.F. Bahr, N.R. Moody, J.W. Hoehn, "Length-scale-based hardening model for ultra-small volumes." J. Materials Research 19 (2004): 2812-2821.

[63] W.W. Gerberich, J.M. Jungk, L. Min, A.A. Volinsky, J.W. Hoehn, K. Yoder, "Length scales for the fracture of nanostructures." Int. J. of Fracture 119 (2003): 387-405.

[64] W. M. Mook, J. D. Nowak, C. R. Perrey, C. B. Carter, R. Mukherjee, S. L. Girschick, P. McMurray, W. W. Geberich, "Compressive stress effects on Nanoparticle modulus and fracture." Phys. Rev. B. 75 (2007): 214112.

[65] Z. P. Bažant, "Size effect." International Journal of Solids and Structures 37 (2000): 69-80.

[66] J. R. Morris, H. Bei, G. M. Pharr, E. P. George, "Size effects and stochastic behavior of nanoindentation pop in." Physical review letters 106 (2011): 165502.

[67] J. R. Greer and W. D. Nix, "Nanoscale gold pillars strengthened through dislocation starvation." Physical Review B 73.24 (2006): 245410.

[68] C. Chisholm, H. Bei, M. B. Lowry, J. Oh, S. S.Asif, O. L.Warren, Z. W. Shan, E. P. George, A. M. Minor, "Dislocation starvation and exhaustion hardening in Mo alloy nanofibers." Acta Materialia, 60 (2012): 2258-2264.

[69] C. J. Bayley, W. A. M. Brekelmans, M. G. D. Geers, "A comparison of dislocation induced back stress formulations in strain gradient crystal plasticity." International Journal of Solids and Structures 43.24 (2006): 7268-7286.

[70] A.D. Fischer-Cripps, Nanoindentation. Springer: New York, 2004.

[71] W.C. Oliver, G.M. Pharr, "An improved technique for determining hardness and elastic modulus using load and displacement sensing indentation experiments." J. Materials Research 7 (1992): 1564-1583.

[72] W.C. Oliver, G.M. Pharr, "Measurement of hardness and elastic modulus by instrumented indentation: Advances in understanding and refinements to methodology." J. Materials Research 19 (2004): 3-20.

[73] H. Bei, S. Shim, M.K. Miller, G.M. Pharr, E.P. George, "Effects of focused ion beam milling on the nanomechanical behavior of a molybdenum-alloy single crystal." Appl. Phys. Lett. 91 (2007): 111915.

[74] S. Shim, H. Bei, M.K. Miller, G.M. Pharr, E.P. George, "Effects of focused ion beam milling on the compressive behavior of directionally solidified micropillars and the nanoindentation response of an electropolished surface." Acta Materialia 57 (2009): 503-510.

[75] N. I. Kato, "Reducing focused ion beam damage to transmission electron microscopy samples." Journal of electron microscopy 53.5 (2004): 451-458.

[76] L. A. Giannuzzi, R. Geurts, J. Ringnalda, "2 keV Ga+ FIB milling for reducing amorphous damage in silicon." Microscopy and Microanalysis 11.S02 (2005): 828-829.

[77] D. Kiener, et al, "Advanced nanomechanics in the TEM: effects of thermal annealing on FIB prepared Cu samples." Philosophical Magazine 92 (2012): 3269-3289.

[78] D. Williams, C. Carter, Transmission electron microscopy: a textbook for materials science, Springer Verlag, 2009.

[79] R.F. Egerton, S.C. Cheng, "Measurement of local thickness by electron energy-loss spectroscopy." Ultramicroscopy 21 (1987): 231-244.

[80] J. Li, Z. Shan, E. Ma, "Elastic strain engineering for unprecedented materials properties." MRS Bull. 39 (2014): 108-114.

[81] D. G. Schlom, L.-Q. Chen, C. J. Fennie, V. Gopalan, D. A. Muller, X. Pan, R. Ramesh, R. Uecker, "Elastic strain engineering of ferroic oxides." MRS Bull. 39 (2014): 118-130.

164

[82] M. J. Hÿtch, A. M. Minor, "Observing and measuring strain in nanostructures and devices with transmission electron microscopy." MRS Bull. 39 (2014): 138-146.

[83] B. Yildiz, ""Stretching" the energy landscape of oxides—Effects on electrocatalysis and diffusion." MRS Bull. 39 (2014): 147-156.

[84] D. Yu, J. Feng, J. Hone, "Elastically strained nanowires and atomic sheets." MRS Bull.39 (2014): 157-162.

[85] T. Zhu, J. Li, "Ultra-strength materials." Prog. Mater. Sci.55 (2010): 710-757.

[86] S. W. Bedell, A. Khakifirooz, D. K. Sadana, "Strain scaling for CMOS." MRS Bull. 39 (2014): 131-137.

[87] J. R. Greer, W. C. Oliver, W. D. Nix, "Size dependence of mechanical properties of gold at the micron scale in the absence of strain gradients." Acta Mater. 53 (2005): 1821-1830.

[88] M. R. Sørensen, M. Brandbyge, K. W. Jacobsen, "Mechanical deformation of atomic-scale metallic contacts: structure and mechanisms." Phys. Rev. B:Condens. Matter Mater. Phys. 57 (1998): 3283.

[89] F. Östlund, K. Rzepiejewska-Malyska, K. Leifer, L. M. Hale, Y. Tang, R. Ballarini, W. W. Gerberich, J. Michler, "Brittle-to-Ductile Transition in Uniaxial Compression of Silicon Pillars at Room Temperature." Adv. Func. Mater. 19 (2009): 2439-2444.

[90] Y. Zhu, F. Xu, Q. Qin, W. Y. Fung, W. Lu, "Mechanical properties of vapor− liquid− solid synthesized silicon nanowires." Nano Lett. 9 (2009): 3934-3939.

[91] T. Tsuchiya, "Tensile testing of silicon thin films." Fatigue Fract. Eng. Mater. Struct. 28 (2005): 665-674.

[92] X. D. Han, K. Zheng, Y. F. Zhang, X. N. Zhang, Z. Zhang, Z. L. Wang, "Low-temperature in situ large-strain plasticity of silicon nanowires." Adv. Mater. 19 (2007): 2112.

[93] R. A. Minamisawa, M. J. Süess, R. Spolenak, J. Faist, C. David, J. Gobrecht, K. K. Bourdelle, H. Sigg, "Top-down fabricated silicon nanowires under tensile elastic strain up to 4.5%." Nat. Commun. 3 (2012): 1096.

[94] T. Namazu, Y. Isono, T. Tanaka, "Evaluation of size effect on mechanical properties of single crystal silicon by nanoscale bending test using AFM." J. Microelectromech. Syst 9 (2000): 450-459.

[95] Y. Sun, S. E. Thompson, T. Nishida, "Physics of strain effects in semiconductors and metal-oxide-semiconductor field-effect transistors." J. Appl. Phys. 101 (2007): 104503.

[96] P. Hashemi, L. Gomez, J. L. Hoyt, "Gate-all-around n-MOSFETs with uniaxial tensile strain-induced performance enhancement scalable to sub-10-nm nanowire diameter." IEEE Electron Device Lett. 30 (2009): 401-403.

[97] V. Pott, K. E. Moselund, K. E. Moselund, D. Bouvet, L. De Michielis, A. M. Ionescu, "Nanotechnology." IEEE Trans. Nanotechnol. 7 (2008): 733.

[98] M. Chu, Y. Sun, U. Aghoram, S. E. Thompson, "Strain: a solution for higher carrier mobility in nanoscale MOSFETs." Ann. Rev. Mater. Res. 39 (2009): 203-229.

[99] K. Zheng, X. Han, L. Wang, Y. Zhang, Y. Yue, Y. Qin, X. Zhang, Z. Zhang, "Atomic mechanisms governing the elastic limit and the incipient plasticity of bending Si nanowires." Nano Lett. 9 (2009): 2471-2476.

[100] L. Wang, K. Zheng, Z. Zhang, X. Han, "Direct atomic-scale imaging about the mechanisms of ultralarge bent straining in Si nanowires." Nano Lett. 11 (2011): 2382-2385.

[101] S. Hoffmann, I. Utke, B. Moser, J. Michler, S. H. Christiansen, V. Schmidt, S. Senz, P. Werner, U. Gösele, C. Ballif, "Measurement of the bending strength of vapor-liquid-solid grown silicon nanowires." Nano Lett. 6 (2006): 622-625.

[102] D.-M. Tang, C.-L. Ren, M.-S. Wang, X. Wei, N. Kawamoto, C. Liu, Y. Bando, M. Mitome, N. Fukata, D. Golberg, "Mechanical properties of Si nanowires as revealed by in situ transmission electron microscopy and molecular dynamics simulations." Nano Lett. 12 (2012): 1898-1904.

[103] G. Stan, S. Krylyuk, A. V. Davydov, I. Levin, R. F. Cook, "Ultimate bending strength of si nanowires." Nano Lett. 12 (2012): 2599-2604.

[104] D. Chrobak, N. Tymiak, A. Beaber, O. Ugurlu, W. W. Gerberich, R. Nowak, "Deconfinement leads to changes in the nanoscale plasticity of silicon." Nat. Nanotechnol. 6 (2011): 480-484.

[105] N. Zhang, Q. Deng, Y. Hong, L. Xiong, S. Li, M. Strasberg, W. Yin, Y. Zou, C. R. Taylor, G. Sawyer, Y. Chen, "Deformation mechanisms in silicon nanoparticles." J. Appl. Phys. 109 (2011): 063534.

[106] J. Guénolé, S. Brochard, J. Godet, "Unexpected slip mechanism induced by the reduced dimensions in silicon nanostructures: Atomistic study." Acta Mater. 59 (2011): 7464-7472.

[107] J. Godet, L. Pizzagalli, S. Brochard, P. Beauchamp, "Computer study of microtwins forming from surface steps of silicon." Comput. Mater. Sci. 30 (2004): 16-20.

[108] P. Valentini, W. W. Gerberich, T. Dumitrică, "Phase-transition plasticity response in uniaxially compressed silicon nanospheres." Phys. Rev. Lett. 99 (2007): 175701.

[109] L. Pizzagalli, J. Godet, J. Guénolé, S. Brochard, E. Holmstrom, K. Nordlund, T. Albaret, "A new parametrization of the Stillinger–Weber potential for an improved description of defects and plasticity of silicon." J. Phys.: Condens. Matter 25 (2013): 055801.

[110] J. Wang, F. Sansoz, J. Huang, Y. Liu, S. Sun, Z. Zhang, S. X. Mao, "Near-ideal theoretical strength in gold nanowires containing angstrom scale twins." Nature communications 4 (2013): 1742.

[111] P.R. Howie, S. Korte, W. J. Clegg. "Fracture modes in micropillar compression of brittle crystals." Journal of Materials Research 27 (2012): 141-151.

[112] S. Garcia-Manyes and A.G. Guell, "Mechanics of silicon surfaces with atomic force microscopy: insight to the first stages of plastic deformation." J.Chem. Phys. 123 (2005): 114711/1-7.

[113] J. Frenkel, "Zur theorie der elastizitätsgrenze und der festigkeit kristallinischer körper." Z. Physik 37 (1926): 572-609.

[114] F.D. Murnaghan "The Compressibility of Media under Extreme Pressures." Proceedings of the National Academy of Sciences of the United States of America 30 (1944): 244–247.

[115] C. Begau, A. Hartmaier, E.P. George and G.M. Pharr, "Atomistic processes of dislocation generation and plastic deformation during nanoindentation." Acta Materialia 59 (2011): 934-942.

[116] A. Bapat, M. Gatti, Y. P. Ding, S. A. Campbell, U. Kortshagen, "A plasma process for the synthesis of cubic-shaped silicon nanocrystals for nanoelectronic devices." J. Phys. D: Appl. Phys. 40 (2007): 2247.

[117] A. Bapat, C. Anderson, C. R. Perrey, C. B. Carter, S. A. Campbell, U. Kortshagen, "Plasma synthesis of single-crystal silicon nanoparticles for novel electronic device applications." Plasma Phys. Controlled Fusion 46 (2004): B97.

[118] A. J. Wagner, C. M. Anderson, J. N. Trask, L. Cui, A. Chov, K. A. Mkhoyan, U. R. Kortshagen, „Propagating Nanocavity-Enhanced Rapid Crystallization of Silicon." Thin Films Nano Lett. 13 (2013): 5735-5739.

[114] J. Li, K. J. Van Vliet, T. Zhu, S. Yip, S. Suresh, "Atomistic mechanisms governing elastic limit and incipient plasticity in crystals." Nature 418 (2002): 307-310.

[115] K. J. Van Vliet, J. Li, T. Zhu, S. Yip, S. Suresh, "Quantifying the early stages of plasticity through nanoscale experiments and simulations." Phys. Rev. B 67 (2003): 104105.

[116] I. Salehinia, S. K. Lawrence, D. F. Bahr, "The effect of crystal orientation on the stochastic behavior of dislocation nucleation and multiplication during nanoindentation." Acta Mater. 61 (2013): 1421-1431.

[117] D. L. Callahan, J. C. Morris, "The extent of phase transformation in silicon hardness indentations." J. Mater. Res. 7 (1992): 1614.

[118] I. V. Gridneva, Y. V. Milman, V. I. Trefilov, "Phase transition in diamond-structure crystals during hardness measurements." Phys. Status Solidi (a) 14 (1972): 177-182.

[119] G. M. Pharr, W. C. Oliver, D. R. Clarke, "The mechanical behavior of silicon during small-scale indentation." J. Electron. Mater. 19 (1990): 881-887.

[120] V. Domnich, Y. Gogotsi, S. Dub, "Effect of phase transformations on the shape of the unloading curve in the nanoindentation of silicon." Appl. Phys. Lett. 76 (2000): 2214-2216.

[121] G. M. Pharr, W. C. Oliver, D. S. Harding, "New evidence for a pressure-induced phase transformation during the indentation of silicon." J. Mater. Res. 6 (1991): 1129-1130.

[122] R. G. Hennig, A. Wadehra, K. P. Driver, W. D. Parker, C. J. Umrigar, J. W. Wilkins, "Phase transformation in Si from semiconducting diamond to metallic β-Sn phase in QMC and DFT under hydrostatic and anisotropic stress." Phys. Rev. B 82 (2010): 014101.

[123] J. Rabier, L. Pizzagalli, J. Demenet, "Dislocations in silicon at high stress." Dislocat. Solids 16 (2010): 47-108.

[124] S. Korte, J. S. Barnard, R. J. Stearn, W. J. Clegg, "Deformation of silicon–insights from microcompression testing at 25–500 C." Int. J. Plast. 27 (2011): 1853-1866.

[125] E. J. Kirkland, Advanced computing in electron microscopy, Springer, 2010.

[126] Youssef, Khaled M. and Scattergood, Ronald O. and Murty, K. Linga and Horton, Joseph A. and Koch, Carl. C., "Ultrahigh strength and high ductility of bulk nanocrystalline copper." Applied Physics Letters 87 (2005): 091904.

[127] S.M. Han, T. Bozorg-Grayeli, J.R. Groves, W.D. Nix, "Size effects on strength and plasticity of vanadium nanopillars." Scripta Materialia 63 (2010): 1153-1156.

[128] M.J. Cordill, M.D. Chambers, M.S. Lund, D.M. Hallman, C.R. Perrey, C.B. Carter, A. Bupat, U. Kortshagen and W.W. Gerberich, "Plasticity responses in ultra-small confined cubes and films." Acta Materialia 54 (2006): 4515-4523.

[129] J.D. Eshelby, F.C.Frank and F.R.N. Nabarro, "The equilibrium of linear arrays of dislocations." Philos. Mag., 42 (1951): 351.

[130] A. Bourret, J. Desseaux, A. Renault, "Core structure of the Lomer dislocation in germanium and silicon." Philos. Mag. A 45 (1982): 1-20.

[131] J. Y. Shu, N. A. Fleck, E. Van der Giessen, A. Needleman, "Boundary layers in constrained plastic flow: comparison of nonlocal and discrete dislocation plasticity." Journal of the Mechanics and Physics of Solids, 49 (2001): 1361-1395.

[132] M. Hopcroft, W. D. Nix, T. W. Kenny, "What is the Young's Modulus of Silicon?" Microelectromechanical Systems, Journal of, 19 (2010): 229-238.

[133] J.D. Nowak, A.R. Beaber, O. Ugurlu, S.L. Girshick, and W.W. Gerberich. "Small size strength dependence on dislocation nucleation." Scripta Materialia 62 (2010): 819-822.

[134] T.E. Mitchell, P. Peralta and J.P. Hirth, "Deformation by a kink mechanism in high temperature materials." Acta Materialia, 47 (1999): 3687-3694.

[135] L. Pizzagalli and P. Beauchamp, "Dislocation motion in silicon: the shuffle-glide controversy revisited." Philos. Mag. Lett., 88 (2008): 421-427.

[136] J.L. Demenet, J. Rabier, X. Milhet, M.H. Hong, P. Pirouz, I. Stretton and P. Cordier, "Microstructures of 4H-SiC single crystals deformed under very high stresses." J. Phys.: Condens. Matter, 14 (2002): 12961.

[137] Hirsch, P. B., and S. G. Roberts. "The brittle-ductile transition in silicon." Philosophical Magazine A 64.1 (1991): 55-80.

[138] C. J. Healy and G.J. Acland, "MD simulations of compression of nanoscale iron pillars."MRS Proc., 1369 (2012).

[139] L.M. Hale, X.W.Zhou, J.A. Zimmerman, N.R. Moody, R. Ballarini and W.W. Gerberich, "Molecular dynamics simulation of delamination of a stiff, body-centered-cubic crystalline film from a compliant Si substrate." J. Appl. Phys., 106 (2009): 1- 7.

[140] M.I. Menelev, S. Han D.G. Srolovitz, G.J. Ackland, D.Y. Sun and M. Asta, "Development of new interatomic potentials appropriate for crystalline and liquid iron." Phil. Mag., 83 (2003): 3977-3944.

[141] J. R. Kermode, T. Albaret, D. Sherman, N. Bernstein, P. Gumbsch, M. C. Payne, G. Csányi and A. De Vita, "Low-speed fracture instabilities in a brittle crystal." Nature 455 (2008): 1224-1227.

[142] M. Imai and K. Sumino, "In situ X-ray topographic study of the dislocation mobility in high-purity and impurity-doped silicon crystals." Philosophical Magazine Part B 47 (1983): 599-621.

[143] S. B. Kulkarni and W. S. Williams, "Dislocation velocities and electronic doping in silicon." Journal of Applied Physics 47.10 (1976): 4318-4324.

[144] A. Xiao, H. Pape, B. Wunderle, H.M.B. Jansen, J. de Vreugd, L. J. Ernst, "Interfacial fracture properties and failure modeling for microelectronics." In Electronic Components and Technology Conference (2008): 1724-1730.

[145] J. Auersperg, B. Seiler, E. Cadalen, R. Dudek, B. Michel. "Fracture mechanics based crack and delamination risk evaluation and RSM/DOE concepts for advanced microelectronics applications." In Thermal, Mechanical and Multi-Physics Simulation and Experiments in Micro-Electronics and Micro-Systems, 2005. EuroSimE (2005): 197-200

[146] X. Li, B. Bhushan, K. Takashima, C.-W. Baek, Y.-K. Kim, "Mechanical characterization of micro/nanoscale structures for MEMS/NEMS applications using nanoindentation techniques." Ultramicroscopy 97 (2003): 481-494.

[147] H. Kahn, N. Tayebi, R. Ballarini, R.L. Mullen, A.H. Heuer, "Fracture toughness of polysilicon MEMS devices." Sensors and Actuators A: Physical, 82 (2000): 274-280.

[148] A. Akturk, N. Goldsman, G. Metze, "Self-consistent modeling of heating and MOSFET performance in 3-d integrated circuits." Electron Devices, IEEE Transactions on, 52 (2005): 2395-2403.

[149] S. Zimin, L. Litian, L. Zhijian, "Self-heating effect in SOI MOSFETs." In Solid-State and Integrated Circuit Technology, 1998. Proceedings. 1998 5th International Conference on (1998): 572-574.

[150] S. Kolluri, K. Endo, E. Suzuki, K. Banerjee, "Modeling and analysis of self-heating in FinFET devices for improved circuit and EOS/ESD performance." In Electron Devices Meeting, 2007. IEEE International (2007): 177-180.

[151] A. J. Scholten, G. D. J. Smit, R. M. T. Pijper, L. F. Tiemijer, H. P. Tuinhout, J-LPJ Steen, A. Mercha, M. Braccioli, and D. B. M. Klaassen, "Experimental assessment of self-heating in SOI FinFETs." (2009): 305-308.

[152] J. Rabier, A. Montagne, J. M. Wheeler, J. L. Demenet, J. Michler, R. Ghisleni, "Silicon micropillars: high stress plasticity." physica status solidi (c) 10 (2013): 11-15.

[153] P. Veyssiere, J. Rabier, J.L. Demenet and J. Castaing, "Plastic deformation of intrinsic and extrinsic silicon below 500 C." in Deformation of Ceramic Materials II, R.E. Tressler, et al, eds. Plenum Press, N.Y. (1984).

[154] K. Yasutake, S. Shimizu, M. Umano and H. Kawbe, "Velocity of twinning partial dislocations in silicon." J. Appl. Phys. 61 (1987): 940.

[155] P. B. Hirsch and S. G. Roberts, "Modelling plastic zones and the brittle-ductile transition." Philosophical Transactions of the Royal Society of London A: Mathematical, Physical and Engineering Sciences 355 (1997): 1991-2002.

[156] E. Bitzek and P. Gumbsch, "Mechanisms of dislocation multiplication at crack tips." Acta Materialia 61.4 (2013): 1394-1403.

[157] W. Kang and M.T.A. Saif, "In Situ Study of Size and Temperature Dependent Brittle-to-Ductile Transition in Single Crystal Silicon." Advanced Functional Materials 23 (2013): 713-719.

[158] H. Feng, Q. H. Fang, L. C. Zhang, Y. W. Liu, "Special rotational deformation and grain size effect on fracture toughness of nanocrystalline materials." International Journal of Plasticity, 42 (2013): 50-64.

[159] A.R. Beaber, J.D. Nowak, O. Ugurlu, W.M. Mook, S.L. Girshick, R. Ballarini, W.W. Gerberich, "Smaller is tougher." Philosophical Magazine 91 (2011): 1179-1189.

[160] T. Ando, T. Takumi, S. Nozue, K. Sato, "Fracture toughness of Si thin film at very low temperatures by tensile test." In Micro Electro Mechanical Systems (MEMS), 2011 IEEE 24th International Conference on (2011) 436-439.

[161] I. De Wolf and W. M. Van Spengen, "Techniques to study the reliability of metal RF MEMS capacitive switches." Microelectronics reliability 42.9-11 (2002): 1789-1794.

[162] H. Lee, et al., "Characterization of metal and metal alloy films as contact materials in MEMS switches." Journal of Micromechanics and Microengineering 16.3 (2006): 557.

[163] S.P. Lacour, et al., "Design and performance of thin metal film interconnects for skin-like electronic circuits." Electron Device Letters, IEEE 25.4 (2004): 179-181.

[164] F. Faupel, et al., "Adhesion and deformation of metal/polyimide layered structures." Journal of Applied Physics 65.5 (1989): 1911-1917.

[165] P. Wellner, et al., "Channel cracking of β-NiAl thin films on Si substrates." Acta materialia 52.8 (2004): 2325-2336.

[166] M.J. Cordill, et al., "Fracture and delamination of chromium thin films on polymer substrates." Metallurgical and Materials Transactions A 41.4 (2010): 870-875.

[167] D. T. Read and J. W. Dally., "Fatigue of microlithographically-patterned free-standing aluminum thin film under axial stresses." Journal of Electronic Packaging 117.1 (1995): 1-6.

[168] M. Kodera, et al., "Stress corrosion cracking of Cu interconnects during CMP with a Cu/porous low-k structure." Journal of The Electrochemical Society 152 (2005): G506-G510.

[169] A.A. Volinsky, J.B. Vella, W.W. Gerberich, "Fracture toughness, adhesion and mechanical properties of low-K dielectric thin films measured by nanoindentation." Thin Solid Films 429 (2003): 201-210.

[170] K. Kim, V.I. Artyukhov, W. Regan, Y. Liu, M.F. Crommie, B.I. Yakobson, A. Zettl, "Ripping graphene: preferred directions." Nano Letters 12 (2011): 293-297.

[171] S. Sundararajan, B. Bhushan, "Development of AFM-based techniques to measure mechanical properties of nanoscale structures." Sensors and Actuators A: Physical 101 (2002): 338-351.

[172] J. Ast, T. Przybilla, V. Maier, K. Durst, M. Göken, "Microcantilever bending experiments in NiAl–Evaluation, size effects, and crack tip plasticity." J Mater Res 29 (2014): 2129–2140.

[173] B. Völker, S. Venkatesan, W. Heinz, K. Matoy, R. Roth, J.M. Batke, R. Roth, M.J. Cordill G. Dehm, "Following crack path selection in multifilm structures with weak and strong interfaces by in situ 4-point-bending." J Mater Res 30 (2015): 1090–1097.

[174] J.M. Krafft, A.M. Sullivan, R.W. Boyle, "Effect of dimensions on fast fracture instability of notched sheets." Proceedings of the Crack Propagation Symposium 1 (1961): 8-26.

[175] W.F. Brown, J.E. Srawley, "Plane strain crack toughness testing of high strength metallic materials." Philadelphia: American Society for Testing and Materials (1966).

[176] J.F. Knott, Fundamentals of fracture mechanics. Gruppo Italiano Frattura (1973) .

[177] K. Hellan, Introduction to fracture mechanics. Vol. 150. New York: McGraw-Hill (1984).

[178] H. Hosokawa, A.V. Desai, M.A. Haque, "Plane stress fracture toughness of freestanding nanoscale thin films." Thin Solid Films 516 (2008): 6444-6447.

[179] V.M. Paviot, J.J. Vlassak, W.D. Nix, "Measuring the mechanical properties of thin metal films by means of bulge testing of micromachined windows." MRS Proceedings 356 Cambridge University Press (1994): 579.

[180] J. Chen, S.J. Bull, "Assessment of the toughness of thin coatings using nanoindentation under displacement control." Thin Solid Films 494 (2006): 1-7.

[181] M.A. Haque, M.T.A. Saif, "In-situ tensile testing of nano-scale specimens in SEM and TEM." Experimental Mechanics 42 (2002): 123-128.

[182] G. Dehm, M. Legros, B. Heiland , "In-situ TEM straining experiments of Al films on polyimide using a novel FIB design for specimen preparation." Journal of materials science 41 (2006): 4484-4489.

[183] A.M. Minor, S. S. Asif, Z. Shan, E.A. Stach, E. Cyrankowski, T.J. Wyrobek, O.L. Warren, "A new view of the onset of plasticity during the nanoindentation of aluminium." Nature materials 5 (2006): 697-702.

[184] B.N. Jaya, V. Jayaram, S.K. Biswas, "A new method for fracture toughness determination of graded (Pt, Ni) Al bond coats by microbeam bend tests." Philosophical Magazine 92 (2012): 3326-3345.

[185] B.N. Jaya, V. Jayaram, "Crack stability in edge-notched clamped beam specimens: modeling and experiments." Int J Fract 188 (2014): 213–228.

[186] B.N. Jaya, C. Kirchlechner, G. Dehm, "Can microscale fracture tests provide reliable fracture toughness values? A case study in silicon." J Mater Res 30 (2015): 686–698.

[187] G. Moser, H. Felber, B. Rashkova, P.J. Imrich, C. Kirchlechner, W. Grosinger, C. Motz, G. Dehm, D. Kiener, "Sample preparation by metallography and focused ion beam for nanomechanical testing." Practical Metallography 49 (2012): 343-355.

[188] J. E. Srawley "Wide range stress intensity factor expressions for ASTM E 399 standard fracture toughness specimens." International Journal of Fracture 12.3 (1976): 475-476.

[189] Designation, A. S. T. M. "E399-90. Standard test method for plane-strain fracture toughness of metallic materials." 1991 Annual Book of ASTM Standards 3 (1997): 485-51.

[190] S. Kumar, X. Li, M.A. Haque, H. Gao, "Is stress concentration relevant for nanocrystalline metals?" Nano Letters 11 (2011): 2510-2516.

[191] S. Kumar, M.A. Haque, H. Gao, "Transformation induced toughening and flaw tolerance in pure nanocrystalline aluminum." International Journal of Plasticity 44 (2013): 121-128.

[192] M.D. Drory, R.H. Dauskardt, A. Kant, R.O. Ritchie, "Fracture of synthetic diamond." Journal of Applied Physics 78 (1995): 3083-3088.

[193] N. Pugno, "Predictions of strength in MEMS components with defects - a novel experimental-theoretical approach." International Journal of Solids and Structures 42 (2005): 647-61.

[194] D.E.J. Armstrong, A.S.M.A. Haseeb, S.G. Roberts, A.J. Wilkinson, K. Bade, "Nanoindentation and micro-mechanical fracture toughness of electrodeposited nanocrystalline Ni–W alloy films." Thin Solid Films 520 (2012): 4369-4372.

[195] J. May, H.W. Höppel, M. Göken, "Strain rate sensitivity of ultrafine-grained aluminium processed by severe plastic deformation." Scripta Materialia 53 (2005): 189-194.

[196] R.A. Schwarzer, "Advances in crystal orientation mapping with the SEM and TEM." Ultramicroscopy 67 (1997): 19-24.

[197] J. Chen and S.J. Bull, "Finite Element Modelling of Delamination in Multilayer Coatings." Nanoscience and Nanotechnology Letters 5 (2013): 795-800.

[198] S.N. Alturi, T.L. Nishioka M. Nakagaki, "Incremental path-independent integrals in inelastic and dynamic fracture mechanics." Engineering Fracture Mechanics 20 (1984): 209-244.

[199] F.W. Brust, J.J. McGowan, S.N. Atluri, "A combined numerical/experimental study of ductile crack growth after a large unloading using T*, J and CTOA criteria." Engineering Fracture Mechanics 23 (1986): 537-550.

[200] J. Chen and S.J. Bull, "On the relationship between plastic zone radius and maximum depth during nanoindentation." Surface and Coatings Technology 201 (2006): 4289-4293.

[201] C.F. Shih, "Relationships between the J-integral and the crack opening displacement for stationary and extending cracks." Journal of the Mechanics and Physics of Solids 29 (1981): 305-326.

[202] A.D. Bakker, "Evaluation of elastic fracture mechanics parameters for bend specimens." International Journal of Fracture 71 (1995): 323-343.

[203] T. Ye, Z. Suo, A.G. Evans, "Thin film cracking and the roles of substrate and interface." International Journal of Solids and Structures 29 (1992): 2639-2648.

[204] X.-K. Zhu, J.A. Joyce, "Review of fracture toughness (G, K, J, CTOD, CTOA) testing and standardization." Engineering Fracture Mechanics 85 (2012): 1-46.

[205] E.Y. Guo, H.X. Xie, S.S. Singh, A. Kirubanandham, T. Jing, N. Chawla, "Mechanical Characterization of Microconstituents in a Cast Duplex Stainless Steel by Micropillar Compression." Materials Science and Engineering: A 598 (2014): 98-105.

[206] S. Wurster, C. Motz, R. Pippan, "Characterization of the fracture toughness of micro-sized tungsten single crystal notched specimens." Philosophical Magazine 92 (2012): 1803-1825.

[207] R.A. Causey and T.J. Venhaus, "The use of tungsten in fusion reactors: a review of the hydrogen retention and migration properties." Physica scripta 94 (2001): 9.

[208] R. Neu, et al., "Tungsten: an option for divertor and main chamber plasma facing components in future fusion devices." Nuclear fusion 45 (2005): 209.

[208] R. E. Hook and J. P. Hirth, "The deformation behavior of isoaxial bicrystals of Fe-3% Si." Acta Metallurgica 15.3 (1967): 535-551.

[209] E.-I. Furubayashi, "Behavior of Dislocations in Fe-3% Si under Stress." Journal of the Physical Society of Japan 27.1 (1969): 130-146.

[210] Y.Qiao and A.S. Argon, "Brittle to ductile transition of cleavage fracture by thermal crack arrest in Fe-3%Si single crystals." Mech. Mater 35 (2003): 903-912.

[211] W.W. Gerberich, P.G. Marsh and H. Huang, "The effect of local dislocation arrangements on hydrogen-induced cleavage." Fundamental Aspects of stress Corrosion Cracking, TMS/ASM Parkins Symposium, TMS Warrendale, (1992): 191-204.

[212] P. G. Marsh, Prediction of fracture toughness, stress-corrosion cracking thresholds and corrosion fatigue thresholds in iron-base materials. PhD Thesis, University of Minnesota (1994).

[213] S. Demouchy, S.J. Mackwell, and D.L. Kohlstedt, "Influence of hydrogen on Fe-Mg interdiffusion in (Mg,Fe)O and implications for Earth's lower mantle." Contrib. Mineral. Petrol. 154 (2007): 279-289.

[214] D.L. Kohlstedt, Water and rock deformation, "The case for and against a climb controlled creep rate." in Water in Nominally Anhydrous Minerals, eds. H. Keppler and J.R.Smyth, Reviews in Mineralogy and Geochemistry 62 (2006): 377-396.

[215] W.W.Gerberich, D.D. Stauffer, A.R. Beaber and N.I. Tymiak, "A brittleness transition in silicon due to scale." J. Materials Res. 27 (2012): 552-561.

[216] W.W. Gerberich, N.I. Tymiak, J.C. Grunlan, M.F. Horstemeyer and M. I. Baskes, "Interpretations of Indentation Size Effects." J. Appl. Mechanics 69 (2002): 433-442.

[217] W.W. Gerberich, J. Michler, W.M. Mook, R. Ghisleni, F. Östlund, D.D. Stauffer and R. Ballarini, "Scale effects for strength, ductility and toughness in brittle materials." J. Mater. Res 24 (2009): 898-906.

[218] A.H. Cottrell and B.A. Bilby, "Dislocation theory of yielding and strain ageing in iron." Proc. Phys. Soc. A 62 (1949): 49.

[219] P.G. Marsh and W.W. Gerberich, "A microscopically-shielded Griffith criterion for cleavage in grain-oriented silicon steel." Acta Metall. Mater. 42 (1994): 613-619.

[220] F. Garofalo, " The dependence of the lower yield strength in iron and steel on grain size and temperature." Metall. Trans. 3 (1972): 3115-3119

[221] Y.T. Chen, D. G. Atteridge and W.W. Gerberich, "Plastic flow of Fe-binary alloys—I. A description at low temperatures." Acta Metallurgica 29 (1981): 1171-1185.

[222] C.H. Ersland, Atomistic modeling of failure in iron. Ph.D. thesis, Norwegian University of Science and Technology (2012).

[223] A. Barnoush, C. Bies and H. Vehoff, " In situ electrochemical nanoindentation of FeAl (100) single crystal: Hydrogen effect on dislocation nucleation." J. Mat'ls Res. 24 (2009): 1105-1113.

[224] X. Gao, "Displacement burst and hydrogen effect during loading and holding in nanoindentation of an iron single crystal." Scripta Mater. 53 (2005): 1315-1320.

[225] R. Kircheim, "Solid solution softening and hardening by mobile solute atoms with special focus on hydrogen." Scripta Mater. 67 (2012): 767-770.

[226] F.A. McClintock and G.R. Irwin, "Plasticity Aspects of Fracture Mechanics." ASTM STP 381, (1964): 84-113.

[227] A. Barnoush and H. Vehoff, "In situ electrochemical nanoindentation : A nanomechanics approach to rank hydrogen embrittlement in extremeley small volumes." Proceedings of the 2008 International Hydrogen Conference (ASM International) (2009): 187-194.

[228] P. Sofronis and H.K. Birnbaum, "Mechanics of the hydrogen-impurity-interactions: Part I - Increasing shear modulus." J.Mech. Phys. Solids 43(1), 49-90 (1995).

[229] K. Nibur, D. Bahr and B. Somerday, "Hydrogen effects on dislocation activity in austenitic stainless steel." Acta Mater. 5 (2006): 2677-2684.

[230] M. Itakura, H. Kaburaki, M. Yamaguchi, T. Okita, "The effect of hydrogen atom on the screw dislocation mobility in BCC iron: A first principles study." Cond. Mat. Matrl-Sci, (2013).

[231] D. L. Goldsby and T. E. Tullis, "Low frictional strength of quartz rocks at subseismic slip rates." Geophysical Research Letters 29.17 (2002): 25-1.

[232] M. S. Duesbery, B. Joos, D. J. Michel, "Dislocation core studies in empirical silicon models." Physical Review B 43.6 (1991): 5143.

[233] M. J. Buehler, et al., "Threshold crack speed controls dynamical fracture of silicon single crystals." Physical Review Letters 99.16 (2007): 165502.

[234] J.W. Hutchinson, "Plasticity at the micron scale." International Journal of Solids and Structures 37.1 (2000): 225-238.

[235] R. Ramachandramoorthy, R. Bernal, H. D. Espinosa, "Pushing the Envelope of In Situ Transmission Electron Microscopy." ACS nano (2015).

[236] A. George and G. Champier, "Velocities of screw and 60˚ dislocations in n- and p-type silicon" Phys.Stat.Sol. (a) 53 (1979): 529-540.

[237] J. R. Patel, L. R. Testardi, P. E. Freeland, "Electronic effects on dislocation velocities in heavily doped silicon." Physical Review B 13.8 (1976): 3548.

[238] M.S.R.N. Kiran, T.T. Tran, L.A. Smillie, B. Haberl, D. Subianto, J. S. Williams, J. E. Bradby, "Temperature-dependent mechanical deformation of silicon at the nanoscale: Phase transformation versus defect propagation." Journal of Applied Physics 117 (2015): 205901.

[239] K. Kang and W. Cai, "Size and temperature effects on the fracture mechanisms of silicon nanowires: Molecular dynamics simulations." International Journal of Plasticity, 26 (2010): 1387-1401.

[240] R. Gröger, A. G. Bailey, V. Vitek, "Multiscale modeling of plastic deformation of molybdenum and tungsten: I. Atomistic studies of the core structure and glide of 1/2< 111> screw dislocations at 0K." Acta Materialia 56.19 (2008): 5401-5411.

[241] J. Rabier and J. L. Demenet, "On a change in deformation mechanism in silicon at very high stress: new evidences." Scripta materialia 45.11 (2001): 1259-1265.

[242] Q. Wei, S. Cheng, K.T. Ramesh, E. Ma, "Effect of nanocrystalline and ultrafine grain sizes on the strain rate sensitivity and activation volume: fcc versus bcc metals." Materials Science and Engineering: A 381 (2004): 71-79.

[243] R. Hull, "Properties of crystalline silicon." EMIS Data Reviews Series, No. 20, Inspec Publications, IEEE, London, (1999): 1390.

[244] P. Pirouz, J.L. Demenet, M.H. Hong, "On transition temperatures in the plasticity and fracture of semiconductors." Phil. Mag. A. 81 (2001): 1207-1227.

[245] H. R. Kolar, J. C. H. Spence, H. Alexander, "Observation of moving dislocation kinks and unpinning." Physical review letters 77 (1996): 4031.

[246] Minor, A. M., J. W. Morris Jr, and E. A. Stach, "Quantitative in situ nanoindentation in an electron microscope." Applied Physics Letters 79 (2001): 1625-1627.